Journal of Research of the National Institute of Standards and Technology

Volume 99 Number 1 January–February 19

U.S. Department of Commerce—**Ronald H. Brown,** Secretary
Technology Administration—**Mary L. Good,** Under Secretary for Technology
National Institute of Standards and Technology—**Arati Prabhakar,** Director

The Journal of Research of the National Institute of Standards and Technology features advances in measurement methodology and analyses consistent with the NIST responsibility as the nation's measurement science laboratory. It includes reports on instrumentation for making accurate and precise measurements in fields of physical science and engineering, as well as the mathematical models of phenomena which enable the predictive determination of information in regions where measurements may be absent. Papers on critical data, calibration techniques, quality assurance programs, and well-characterized reference materials reflect NIST programs in these areas. Special issues of the Journal are devoted to invited papers in a particular field of measurement science. Occasional survey articles and conference reports appear on topics related to the Institute's technical and scientific programs.

ISSN 1044-677X **Coden: JRITEF** **Library of Congress Catalog Card No.: 89-656121**

United States Government Printing Office, Washington: 1994

Volume 99, Number 1, January–February 1994
Journal of Research of the National Institute of Standards and Technology

Contents

Articles

Conference Reports

News Briefs

Volume 99, Number 1, January–February 1994
Journal of Research of the National Institute of Standards and Technology

Volume 99, Number 1, January–February 1994
Journal of Research of the National Institute of Standards and Technology

Volume 99, Number 1, January–February 1994
Journal of Research of the National Institute of Standards and Technology

[J. Res. Natl. Inst. Stand. Technol. 99, 1 (1994)]

Precision Comparison of the Lattice Parameters of Silicon Monocrystals

Volume 99 Number 1 January–February 1994

E. G. Kessler, A. Henins, R. D. Deslattes, L. Nielsen,[1] and M. Arif

National Institute of Standards and Technology, Gaithersburg, MD 20899-0001

The lattice spacing comparator established at the National Institute of Standards and Technology to measure the lattice spacing differences between nearly perfect crystals is described in detail. Lattice spacing differences are inferred from the measured differences in Bragg angles for different crystals. The comparator is a two crystal spectrometer used in the nearly nondispersive geometry. It has two x-ray sources, two detectors, and a device which permits remote interchange of the second crystal sample. A sensitive heterodyne interferometer which is calibrated with an optical polygon is used to measure the Bragg angles. The crystals are manufactured with nearly equal thicknesses so that the recorded profiles exhibit pendellosung oscillations which permit more precise division of the x-ray profiles. The difference in lattice spacing between silicon samples used at Physikalisch-Technische Bundesanstalt (PTB) and NIST has been measured with a relative uncertainty of 1×10^{-8}. This measurement is consistent with absolute lattice spacing measurements made at PTB and NIST. Components of uncertainty associated with systematic effects due to misalignments are derived and estimated.

Key words: Bragg angle; lattice spacing; silicon; x-ray diffraction; x-ray spectrometer.

Accepted: October 25, 1993

Contents

1. Introduction

Absolute measurements of the crystal lattice spacing of silicon have been reported by two laboratories [1,2,3,4] and are in progress in at least two other laboratories [5,6]. These experiments present a very difficult metrological challenge and require extreme care in order to achieve a relative uncertainty of several parts in 10^8. The output of these experiments is the lattice spacing of a particular silicon specimen in terms of an optical wavelength standard.

[1] Present address: Danish Institute of Fundamental Metrology, DK-2800 Lyngby, Denmark.

Crystals having well defined lattice spacings and whose lattice spacings are known with an uncertainty in the 0.1 to 0.01 ppm range (1ppm = 10^{-6}) are needed in the field of metrology (i.e., x-ray and gamma-ray wavelength measurements). However, the effort required to directly compare a large family of crystal samples to an optical wavelength standard is prohibitive. Thus, several techniques and devices to more rapidly measure lattice spacing differences with a relative uncertainty below 0.1 ppm have been devised. This paper describes in detail the precision lattice spacing comparator (Δd comparator) established at the National Institute of Standards and Technology and reports the results of a careful comparison of Si samples which were measured absolutely by the x-ray interferometer technique at the Physikalisch-Technische Bundesanstalt (PTB) and NIST. The measured lattice spacing difference has a relative uncertainty of 1.4×10^{-8} and is, at present, consistent with the absolute measurements reported by the two laboratories.

2. Principle of the Measurement

The principle of the NIST lattice-comparison measurement is illustrated by the geometrical layout of the spectrometer (Fig. 1). This geometry, which is similar to one suggested by Hart [7], is a conventional double-crystal Laue-case spectrometer. Ando et al. [8], Becker et al. [9], and Häusermann et al. [10] have also used similar geometries

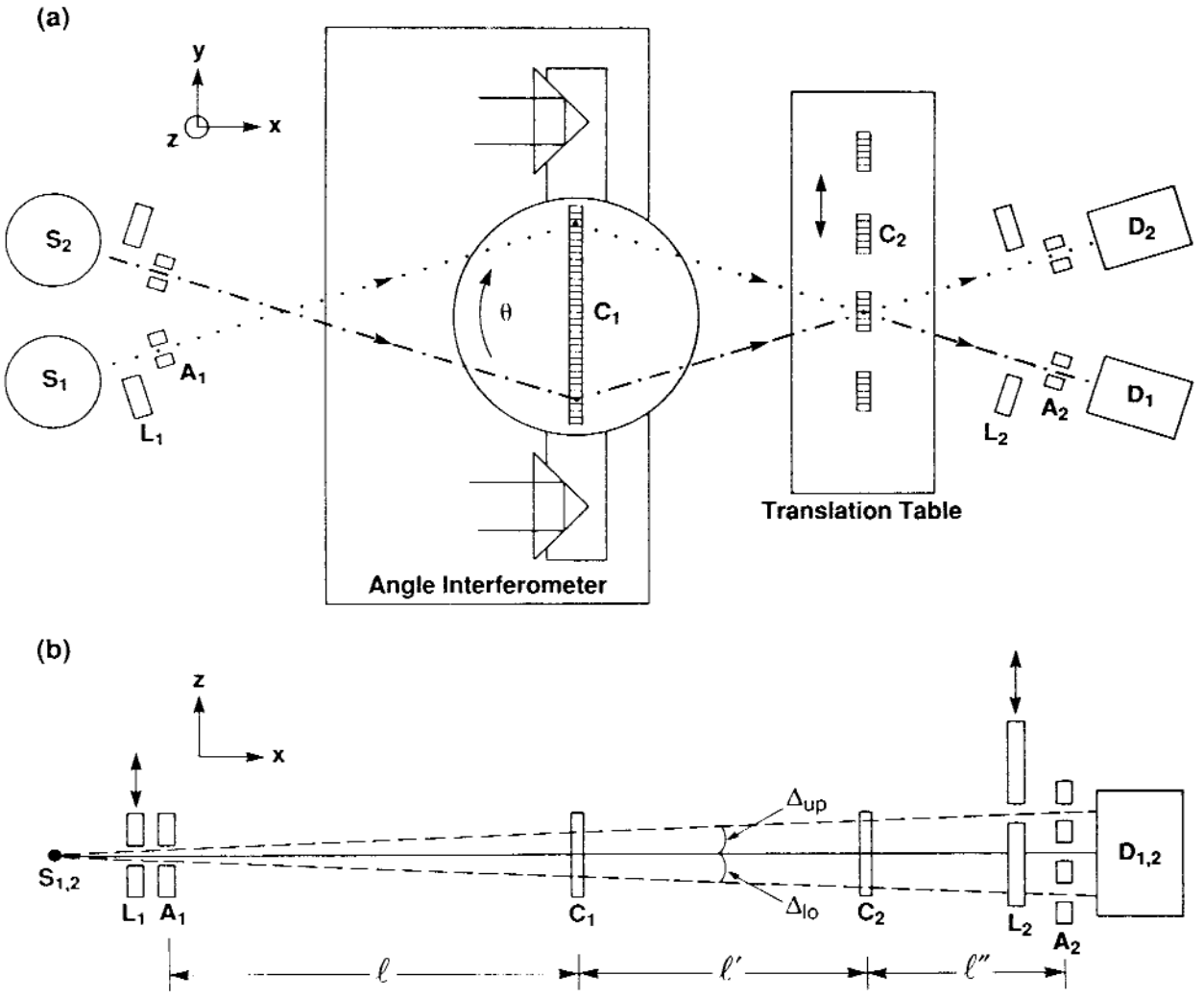

Fig. 1. Schematic diagram of the NIST lattice spacing comparator. S_1, S_2—x-ray sources; L_1, L_2—shutters; A_1, A_2—apertures; C_1, C_2—crystals; D_1, D_2—detectors; l, l' l''—x-axis projections of the x-ray paths from A_1 to C_1, C_1 to C_2, C_2 to A_2, respectively. a) Top view (x, y plane), b) side view (x, z plane)

to precisely compare lattice spacings. As will emerge in the discussion which follows, the NIST instrument has certain new features which enhance its generality and sensitivity. The spectrometer has two sources, S_1 and S_2, two crystals, C_1 and C_2 and two detectors, D_1 and D_2, and is used to record only nearly nondispersive profiles. The x-ray beams are defined by precision source, A_1, and detector, A_2, apertures and there are computer controlled shutters, L_1 and L_2, near the sources and the detectors, respectively.

By using the spectrometer in the nearly nondispersive mode, the large intrinsic linewidths associated with characteristic x-ray emission do not contribute appreciably to the width of the recorded profiles. The source shutters permit isolation of the two x-ray paths so that doubly diffracted profiles from one source can be recorded without interference from singly diffracted profiles from the other source. There are three apertures in front of each detector (Fig. 1b), one above, one on, and one below the plane of dispersion. An indexed shutter selects one of these apertures depending on whether lattice spacing difference scans or crystal alignment scans are being recorded. For lattice spacing difference scans, apertures on the plane of dispersion are used for both sources and the detectors. As crystal 1 is rotated through the reflection, the source shutters alternately pass and block the two x-ray paths, path $(\cdots)$ and path $(-\cdot-)$, so that the two x-ray profiles are essentially recorded simultaneously. Thus errors due to drifts of the crystals or the angle interferometer are eliminated. For crystal alignment scans, only one source is used and the detector shutter alternately permits radiation to pass through the apertures above and below the plane of dispersion as crystal 1 is scanned. The angular shift of these two out-of-plane profiles is related to the tilt misalignment of the planes of the first crystal with respect to the planes of the second crystal. By careful alignment, the contribution to the uncertainty due to crystal tilt misalignment can be made small (see Appendix A).

General features of the comparator operation may be understood as follows: If the crystal planes near the ends of the first crystal are parallel and the lattice spacings of the first (d_1) and the second (d_2) crystals are equal ($d_1 = d_2$), then the profiles in the path $(\cdots)$ and the path $(-\cdot-)$ will peak at the same angular setting of the first crystal. However, if $d_1 \neq d_2$, then there will be an angular offset, $\beta_{2,1}$ between the two profiles which is a measure of the lattice spacing difference, $\Delta d = d_2 - d_1$, between the two crystals. If θ_1 and θ_2 are the Bragg angles of crystals 1 and 2, respectively, then $\beta_{2,1} = 2(\theta_2 - \theta_1) = 2\Delta\theta$. If $\Delta d/d$ is small ($< 10^{-5}$) and the required uncertainty in $\Delta d/d$ is $\sim 10^{-8}$, then it is appropriate to use the differential form of the Bragg equation to express $\Delta d/d$.

$$\Delta d/d = -(\Delta\theta)\cot\theta = -(\beta_{2,1}/2)\cot\theta \qquad (1)$$

In our comparison scheme, the first long crystal serves as a temporary (a few hours) reference. Profiles are recorded using one of the small second crystals. Then another small second crystal is brought into the position where the x-ray beams diffracted by the first crystal intersect. The first crystal is again scanned and profiles are recorded.

By subtracting the angular offsets, β, measured with the different second crystal samples, the properties of the first crystal such as the absolute lattice spacing, the effects of variation in lattice spacing, and parallelism of crystal planes at the two ends of the crystal are eliminated. One needs only assume that the properties of the first crystal are constant during the time of measurement of the two different second crystal samples. The equation for the difference in crystal lattice spacings for the pair of small crystals becomes

$$\Delta d/d_s = -(\Delta\theta)\cot\theta_s = -(\beta/2)\cot\theta_s\,, \qquad (2)$$

where θ_s = the Bragg angle for the standard sample, θ_u = the Bragg angle for the unknown sample, d_s = lattice spacing of standard sample, d_u = lattice spacing of unknown sample, $\Delta d = d_s - d_u$, $\beta_s = 2(\theta_s - \theta_1)$ = angular offset for the standard sample, $\beta_u = 2(\theta_u - \theta_1)$ = angular offset for the unknown sample, and $\beta = \beta_s - \beta_u = 2(\theta_s - \theta_u) = 2\Delta\theta$.

In Appendix A the equations for calculating Δd in ideal and misaligned geometries are derived. For small lattice parameter differences and well aligned x-ray beams and crystals, the more involved equations derived in the appendix reduce to Eq. (2). The forms of the corrections associated with misalignments are explicitly given and their magnitudes are estimated for our particular spectrometer. This appendix is likely to be most interesting to the precision x-ray specialist. Throughout this paper and particularly in the appendix the path $(\cdots)$ is referred to as the path $(-)$ and the path $(-\cdot-)$ is referred to as the path $(+)$.

Since x rays from the two paths interrogate the same area of the second crystal, small variations in lattice spacing along a crystal can be measured with this scheme. The second crystal samples reside on a precision slide which allows easy interchange of

crystal samples. A typical data sequence involves many changes of crystal samples and permits compensation for drifts of the crystals and the angle measuring spectrometer.

3. Experimental Apparatus

The lattice comparison spectrometer rests on a 1 m × 2 m cast iron plate which is isolated from building vibrations by three passive air bags. The x-ray tubes, detectors, and shutters are rigidly attached to this plate. A smaller plate (61 cm × 122 cm) on which the laser, receiver, and precision spectrometer are mounted rests on vibration damping rubber feet on top of the large cast iron plate. The precision spectrometer is constructed on a 35 cm × 74 cm × 2.5 cm thick cast iron U channel. The angle interferometer, rotary table, and translation table reside on top of the inverted U channel and the drive arm coupled to the rotary table is conveniently located underneath the channel. The important dimensions which define the scale of the spectrometer are: 1) x-ray focal spot to source slit = 6 cm; 2) source slit to x-ray tube pivot = 25.4 cm; 3) x-ray tube pivot to first crystal = 8.25 cm; 4) first crystal to second crystal = 8.25 cm; and 5) second crystal to detector slit = 28.5 cm.

The radiation sources are identical silver or molybdenum x-ray tubes operated at $V = 40$ keV and $I = 15$ mA and having a 1 mm × 1 mm focal spot (in projection). The tubes are cooled by temperature regulated water so that the spectrometer temperature remains constant and uniform. The x-ray sources pivot about the point of intersection of the x-ray beams which lies between the sources and the first crystal. Bragg angles from 10° to 22° are accessible. The vertically defining slits in front of the sources have a 1 mm opening. The center of these slits and the middle slits near the detectors are carefully placed on the plane of dispersion (plane perpendicular to the axis of rotation) to within 0.1 mm. The x-ray tubes are positioned so that the focal spots fill the source and detector slits uniformly. The lead shutters near the source slits are computer controlled to block or pass the x-ray beams.

The axis of rotation is a precision commercial rotary table [11] having a radial concentricity and axial movement less than one micrometer. The table is driven by a stepping motor coupled to a threadless screw and a 48 cm long tangent arm with fine adjustment of the rotation obtained by piezoelectric transducers. The long first crystal is mounted in the center of the rotating table so that its diffracting planes are parallel to the axis of rotation to within a few seconds (of plane angle).

Angles are measured by a polarization encoded Michelson interferometer having an angular sensitivity of a few $\times 10^{-4}$ seconds. The interferometer is shown schematically in Fig. 2 where the inset shows the over and under arrangement of the beams. The interferometer is illuminated by a commercial 633 nm HeNe laser [12] which emits two orthogonal linearly polarized frequencies separated by 1.8 MHz. The polarization sensitive beam splitter, b, divides the incoming light beam so that one polarization and frequency traverses one arm of the interferometer and the other polarization and frequency traverses the other arm. The beam splitter, steering elements (e, g, h), and compensating element (f) are chosen and positioned so that the two interferometer arms have equal air and equal glass paths at zero angle. Elements c and d are 90° polarization rotators which rotate the plane of polarization of the outgoing and return beams respectively in order that both corner cubes are transversed with the same polarization orientation and that the output beams are directed away from the laser. The roof prisms, i and j, return the light to the corner cubes, k and l, doubling the angular sensitivity of the interferometer and keeping the output beams fixed in space. The corner cubes are mounted on an arm which is rigidly attached to the rotating crystal table and retroreflect the light in each arm of the interferometer.

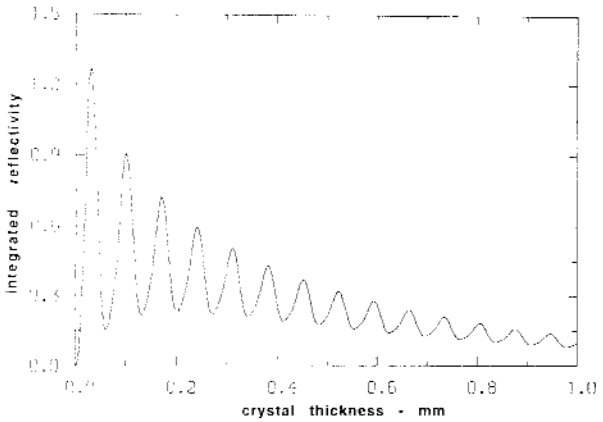

Fig. 2. Schematic diagram of the angle interferometer. a, e, g, h—beam steering elements; b—polarization sensitive beam splitter; c, d—90° polarization rotators; f—glass path compensating plate; i, j—roof prisms; k, l—corner cubes. The insert shows the passage of the beam through the corner cube—roof prism part of the interferometer.

The interferometer output beam which includes the two orthogonally polarized frequencies is analyzed by a 45° polarizer included in a commercial detector which provides a measurement difference frequency signal. The laser and its electronics also provides a reference difference frequency signal for the light emitted by the laser. For a stationary interferometer the two difference frequency signals are identical except for a phase difference ϕ, which is proportional to the difference in the optical path lengths of the two interferometer arms. Rotation of the interferometer arm causes a phase shift of the measurement difference frequency signal relative to the reference difference frequency signal. Conversely, phase comparison of the measurement difference frequency signal with the reference difference frequency signal permits measurement of the angular rotation.

The 1.8 MHz difference frequency signals must be converted into signals which permit up-down counting for clockwise and counter clockwise rotation of the axis, measurement of fringe fractions, and servo control of the axis position. Although electronics to perform these functions is commercially available, no existing system could be conveniently coupled to our spectrometer. An electronics module to perform the above functions has been developed and is briefly described in Appendix B.

The diffraction profiles are recorded as x-ray intensity vs interferometer fringes and, thus, the angular offsets, β are also measured in interferometer fringes. However, the angular offsets, β, needed in Eq. (2) must be in absolute angles. In order to convert interferometer fringes into absolute angles, the angle interferometer is calibrated using an optical polygon and a photoelectric autocollimator [4]. A 24-sided optical polygon (external angles ~15°) is mounted on top of an indexing table on the rotation axis in place of the first crystal. The photoelectric autocollimator senses the directions normal to the faces of the optical polygon. The 24 external angles are measured in terms of interferometer fringes and the sum of the angles is constrained to be 360°. The equation relating angles and fringes is $F = K\sin(\theta)$ where F is the fringe number, θ is the corresponding angle of rotation, and K is the calibration constant. The measured value of K is 5138551.7 at 22.5 °C. Near $\theta = 0°$, the value for the angular rotation/fringe is 0.0401 arcsec/fringe. The calibration constant is directly related to the separation of the corner cubes. Because the arm which defines the separation of the corner cubes is made out of stainless steel, the calibration constant has a large temperature coefficient (~16.7 ppm/°C). As long as the angular offsets are small and the temperature is well controlled, this large temperature coefficient can be tolerated. However, in the near future the spectrometer will be equipped with an invar corner cube arm.

The zero angle of the interferometer is determined by measuring one of the external angles of the polygon in a symmetric and asymmetric fashion. In the symmetric measurement, the polygon is positioned on the axis so that the faces forming the 15° angle are measured at +7.5° and −7.5°. This symmetric measurement of the external angle is quite insensitive to the zero angle of the interferometer. In the asymmetric measurement, the polygon is positioned so that the faces of the same angle are measured at ±14.5° and ∓0.5°. This asymmetric measurement of the external angle is very sensitive to the zero angle of the interferometer. The zero angle is determined by requiring equality of the two measurements of the same angle. The uncertainty of the zero angle determination is approximately 2 arcsec which makes a completely negligible contribution to the measurement of the small angular offsets near zero angle.

The second crystals reside on a precision translator equipped with a stepping motor and a linear encoder [13]. The slide has 15 cm of travel and a positioning accuracy of 0.01 mm. Although the slide has pitch and yaw of a few seconds in a few cm of travel, it is reproducible at the 0.01 second level and shows no short term drift. Each second crystal is mounted on a flexure hinge so its planes can be oriented to be roughly parallel to the planes of the first crystal. Fine adjustment is achieved by applying voltage to a piezoelectric "tipper."

The diffracted x-rays are detected by two identical NaI(Tl) detectors which pivot about the second crystal position. In front of each detector are three slits each 1.6 mm × 1.6 mm. The slits are arranged in the direction normal to the plane of dispersion with center of the middle opening on the plane of dispersion and the top and bottom openings 3.2 mm above and below the plane of dispersion. Each slit has a computer controlled shutter which permits radiation to pass through any one of the three openings.

4. Crystal Preparation

In order to make measurements with an uncertainty of 0.01 ppm, considerable care must be exercised in cutting, polishing, mounting, and aligning the crystal samples. The full width at half

maximum (FWHM) of nondispersive x-ray profiles obtained with Ag Kα radiation and the Si 440 reflection is about 0.6 seconds. Since the angular separation which corresponds to a lattice spacing difference of 1×10^{-8} is ~0.001 seconds, it appears that peak positions must be determined to 1/500 of the FWHM. This is a formidable task requiring very reproducible profiles. However, by carefully matching the thickness of the first and second crystals to within a few micrometers, nondispersive Laue-case rocking curves exhibit oscillatory fine structure which has a modulation period which is typically less than 1/10 of the FWHM of the profile. This fine structure is predicted by the dynamical theory of x-ray diffraction and has been used in high precision determinations of the structure factor of Si [14, 15] and Ge [16] and in x-ray refractive index measurents [17]. We use this fine structure on the x-ray profiles as a sharp convenient reference to measure the angular separation of the profiles.

The integrated reflectivity for the double crystal profiles oscillates as a function of crystal thickness. In Fig. 3, the integrated reflectivity vs crystal thickness is shown for the Si 440 diffraction of Ag Kα radiation. We have chosen a crystal thickness of 0.455 mm as a compromise of intensity and practical problems with thin crystals. Theoretical and experimental profiles for this thickness are shown in Fig. 4.

The theoretical profile [18, 19] is obtained by adding the convolution of two intrinsic reflections for the two polarization states (σ and π)

$$I(\Delta)=I_0\sum_{\sigma,\pi}\int I^{II,\sigma}(\theta)\,I^{\pi,\sigma}(\theta+\Delta)\,\mathrm{d}\theta$$

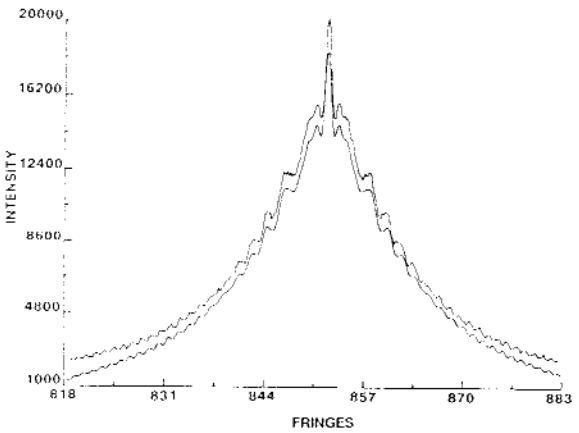

Fig. 3. Integrated reflectivity of double crystal nondispersive profiles as a function of crystal thickness for the Si 440 reflection and Ag $K\alpha_1$ radiation.

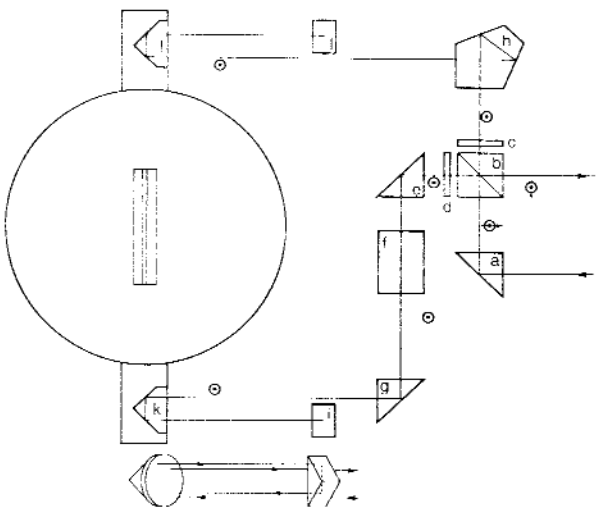

Fig. 4. Theoretical (lower) and experimental (upper) profiles for the 440 reflection of Ag Kα radiation using 0.455 mm thick Si crystals.

where Δ = the angle between the diffracting planes of crystal 1 and crystal 2

$$I^{\pi,\sigma}(\theta)=\exp(-\mu t/\cos\theta_B)\left|\sin[A(y^2+v^2)^{1/2}]/(y^2+v^2)^{1/2}\right|^2$$

$$A=\pi t/t_0$$

$$\chi_h=\chi_{hr}+i\chi_{hi}$$

$$y=\Delta\sin2\theta_B/(C|\chi_{hr}|)$$

$$v^2=\chi_h\chi_{\bar{h}}/|\chi_h\chi_{\bar{h}}|$$

$$t_0=\lambda\cos\theta_B/(C|\chi_{hr}|)$$

$$C=\begin{cases}1 & \sigma\text{ polarization}\\ |\cos2\theta_B| & \pi\text{ polarization}\end{cases}$$

and

θ_B is the Bragg angle
μ is the linear absorption coefficient
t is the crystal thickness
t_0 is the extinction length
y is the angular parameter
C is the polarization factor
λ is the wavelength
χ_h is the complex electronic susceptibility of the crystal: $\chi_{hr}+i\chi_{hi}$

For low absorption where $\chi_{hr}>\chi_{hi}$, it can be shown that

$$v^2=1-i(\epsilon\mu t_0)/(\pi\cos\theta_B)$$

$$t_0=\pi V\cos\theta_B/(\lambda r_e F|C|)$$

$$I^{\pi,\sigma}(\theta)=[\exp(-\mu t/\cos\theta_B)/(y^2+1)]$$

$$\{[\sin^2[A(y^2+1)^{1/2}]+\sinh^2[\mu t\epsilon(y^2+1)^{-1/2}/2\cos\theta_B]\}$$

where $\epsilon = (|\varkappa_{hi}|/|\varkappa_{oi}|)|C|$

$\varkappa_{hi}$, $\varkappa_{oi}$ = imaginary parts of the Fourier coefficients $\varkappa_h$, $\varkappa_o$

V = volume of the unit cell

r_e = classical electron radius

F = temperature modified structure factor

When generating a theoretical profile, numerical values must be assigned to the following quantities μ, t, F, λ, r_e, V, and ϵ. Conversely, when fitting an experimental profile with the theoretical description, a quantity such as t or F can be varied until the difference between the experimental and theoretical profiles is a minimum.

In order to obtain strain free samples, the crystals are made with a 1.5 cm × 1.5 cm base on top of which is the thin 1.5 cm high wafer which is used for diffraction. Drawings of the long first crystal and the second crystal are shown in Figs. 5 and 6. Typical lengths of the long and short crystals are 6.3 cm and 1.2 cm, respectively. The long crystal is balanced on a 1.5 mm wide silicon rod which is centered on an optically polished silicon cylinder. This assembly is waxed together with a low temperature optician's wax. The polished silicon cylinder is attached to a ground cast iron base with epoxy resin. The cast iron base and the rotating table are joined by screw fasteners. After assembly the angular offset between the normal to the polished silicon cylinder and the crystal planes is measured using an x-ray spectrometer and an autocollimator. The long crystal is mounted on a flexure hinge on the rotating table and is tipped an amount equal to the measured offset. In this way the crystal planes are made parallel to the axis of rotation with an estimated uncertainty of 2 seconds.

The short crystal assembly consists of a ground cast iron base, a piezoelectric tipper, a silicon anvil (with a small hole for a thermistor), and the crystal. The base, PZT elements, and silicon anvil are attached by conductive epoxy and the crystal is balanced on the raised portion of the silicon anvil (1.5 mm wide) and attached by low temperature optician's wax. This assembly is mounted on a flexure hinge on the translation table. Using x rays diffracted by the first crystal above and below the plane of dispersion, the planes of the second crystal are made parallel to those of the first crystal by the coarse mechanical adjustment and the fine PZT tipper.

The crystals are cut with a diamond saw and then polished to the desired thickness using a chemically assisted mechanical polishing solution [20]. Typical polishing rates are 10 μm per h and 50 μm to 70 μm are removed from each side t insure that no saw damage remains. Crystal thick ness was measured using a coordinate measurin machine [21]. The reproducibility of the thicknes measuring procedure was 1 μm–2 μm. Polishin the long first crystal so that the two areas used fo diffraction had equal thickness was the most diffi cult task. Because the edges of the crystals tend t be too thin, the areas used for diffraction were a least 2 mm from any crystal edge. After polishing all surfaces of the crystal except for the polishe surfaces were etched in HF/HNO_3 to relieve strair

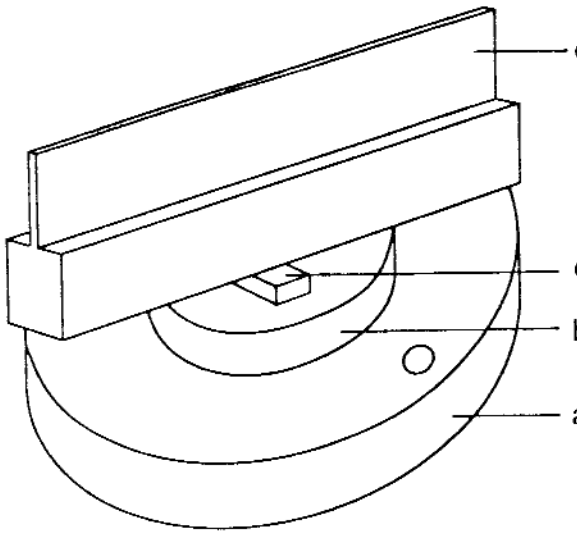

Fig. 5. Detailed drawings of the first crystal. a—cast iron, b—Si disk, and c—Si rod, and d-Si diffraction crystal.

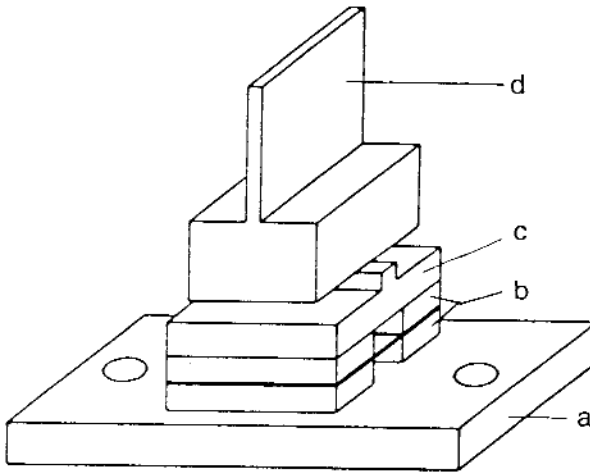

Fig. 6. Detailed drawing of the second crystal. a—cast iron b—PZT, c—Si support, d—Si diffraction crystal.

5. Temperature Measurement and Control

Because the lattice parameter measurements are relative measurements, we required only accurate relative temperature values and not accurate absolute values. Since the expansion coefficient for silicon is 2.56×10^{-6}/K, relative temperature measurements accurate to 4 mK suffice for 1×10^{-8} lattice parameter measurements. Six ultra-stable calibrated thermistor probes are used to measure the temperature of the crystals: two thermistors on the base of the long first crystal (one on each side) and one thermistor on the silicon anvil to which each of the four silicon crystals is attached. Vacuum grease is used to insure good thermal contact between the silicon and the thermistors. The six thermistors and an ultra-stable calibrated standard resistor (2.5 kΩ) [22] are connected in series and powered with a constant current source ($\approx 1\text{x}10^{-5}$ A). A precision digital voltmeter is used to read the voltage drop across each thermistor and the standard resistor. The temperatures are read every 4 s, so the temperature for a measurement time of 20 s is an average of five measurements.

Before and after a critical measurement, the six thermistors are placed in a constant temperature bath in order to measure offsets between the thermistors. The offsets are typically a few mK and are stable to less than 1 mK over times long compared to the few weeks needed for a lattice parameter measurement.

The temperature of the laboratory is constant to within ~0.1 K over several days. For the measurement reported here the spectrometer was isolated from direct air currents within the laboratory by a cloth curtain. The curtain has subsequently been replaced by an insulated chamber. The crystals are covered with an aluminum thermal shield and two 20 mm thick styrofoam thermal shields. The x-ray tubes, motors, and detectors are outside the shields. The temperature difference between the first and second crystals is typically 0.1 K and can be varied by changing the temperature of the water used to cool the x-ray tubes. The temperature differences between the second crystals is only a few mK. Variation of the temperature differences (the critical quantity for relative measurements) over a 24 h period is typically less than 20 mK.

6. Data Analysis

The angular offsets, β_S and β_u, which are needed to calculate $\Delta d/d$ from Eq. (2) are the angular separation of profiles recorded along the path (−) and path (+). The profiles are measured by stepping the axis through N discrete angles (typically $N=110$) which are recorded as angle interferometer fringe numbers. For each angle the number of x-ray photons in each detector is counted for a fixed time (typically 10 s to 20 s). The time per scan is 40 min to 80 min. The fringe numbers for each profile are corrected in a point by point manner for the temperature difference between the first and second crystals. From the Bragg equation the dependence of the diffraction angle, θ, on temperature, T, is easily seen to be

$$d\theta/dT = -\alpha_0 \tan\theta ,$$

where α_0 = linear coefficient of thermal expansion of the crystal. For silicon $\alpha_0 = 2.56\times10^{-6}$/K. Let θ_- and θ_+ be the angular settings of the first crystal for the path (−) and path (+), respectively, the rotation angle reference be the y axis, and clockwise and counter clockwise rotations be positive and negative respectively. When the Bragg condition is simultaneously satisfied at crystals 1 and 2 and both crystals are at a reference temperature, T_0, (see Fig. 1a and Fig. 8),

$$\theta_-(T_0) = \theta_{B2}(T_0) - \theta_{B1}(T_0)$$

and

$$\theta_+(T_0) = -\theta_{B2}(T_0) + \theta_{B1}(T_0).$$

When crystal 1 is at temperature, T_1, and crystal 2 is at temperature, T_2, then these two equations become

$$\theta_-(T_0) = [\theta_{B2}(T_2) - \theta_{B1}(T_1)] - \frac{d\theta}{dT}(T_1 - T_2) =$$

$$\theta_-(T_1, T_2) - \frac{d\theta}{dT}(T_2 - T_1)$$

and

$$\theta_+(T_0) = -\theta_{B2}(T_2) + \theta_{B1}(T_1) + \frac{d\theta}{dT}(T_2 - T_1) =$$

$$\theta_+(T_1, T_2) + \frac{d\theta}{dT}(T_2 - T_1) ,$$

where we have assumed the crystals are of the same material.

The angles θ_- for the path $(-)$ are corrected by $-\mathrm{d}\theta/\mathrm{d}T\ (T_2-T_1)$ while the angles θ_+ for the path $(+)$ are corrected by $+\mathrm{d}\theta/\mathrm{d}T\ (T_2-T_1)$. Since the profiles are recorded in fringe numbers, these angular corrections need to be converted to fringes before adding. The angle measuring interferometer is positioned within a few minutes of the zero degree angle for all the measured offsets. Using the interferometer equation discussed above, the angle to fringe conversion factor of 0.0401 sec/fringe at zero degree angle is determined and used to convert the angle corrections due to temperature differences into fringes.

The angular offsets between the profiles on the temperature corrected fringe scale have been determined by two different methods. In the first method the profiles were fit with a Lorentzian function using a nonlinear least squares procedure in which the position, intensity, width, and background are adjusted. The data with its pronounced wiggles and central spike is not well represented by the smooth Lorentzian function. However, by taking the differences, $R_\pm$, between the recorded profiles, $I_\pm$, and the smooth fitting functions, $L_\pm$, the wiggles of the two profiles are emphasized.

$$R_\pm(\theta_i) = (I_\pm(\theta_i) - L_\pm(\theta_i))$$

The correlation function, $C(\Delta\theta)$, for the two sets of residuals is computed.

$$C(\Delta\theta) = \sum_{i=1}^{N} R_+(\theta_i) + R_-(\theta_i + \Delta\theta),$$

where the sum is over the N data points of the profile.

The value of $\Delta\theta$ for which $C(\Delta\theta)$ is a maximum is the angular separation (offset angle β) of the two profiles. The uncertainty in the measurement of the angular separation of the profiles is typically $\approx 6\times10^{-9}$ rad.

In the second method the dynamical diffraction function was fit to the recorded profiles. The crystal thicknesses were fixed at 0.455 mm and the structure factors were taken from Refs. [14 and 15]. The only adjustable parameters in the fitting procedure were the position, the intensity and the background. The angular separation between the profiles is obtained as the difference between the fitted position of the two profiles. The measured angular separations obtained with the two methods agree within the measurement uncertainty. Because the first method is computationally simpler and more easily adapted to a small computer, it was used to obtain all of the results presented below.

A single lattice comparison run usually consists of 16 to 20 data scans, preceded and followed by alignment scans. The profiles are scanned by repeating the following sequence: unknown crystal—cw rotation, unknown crystal—ccw rotation, standard crystal—cw rotation, and standard crystal—ccw rotation. After determining the angular separation for each scan, the angular separations vs time of day for each crystal are fit with a variable order polynomial (usually 3). The constant (in time) angular offset between these two curves is the angular offset between the unknown and standard crystals for one data set. The scatter in the offsets is typically $<6\times10^{-9}$ rad provided the crystals are well aligned and the same areas of the crystals are used to diffract the x-ray beam.

7. Comparison of Two Silicon Samples

Two Si samples were prepared as described in Sec. 4 from material acquired by PTB and NIST for absolute lattice parameter measurements. The NIST sample was supplied by Dow Chemical[2] and was a slab adjacent to the NIST x-ray/optical interferometer. The PTB material was supplied by Wacker-Chemitronic and labeled WASO 17 by PTB. The relative difference between WASO 17 and WASO 4.2 (the PTB x-ray/optical interferometer crystal) has been measured to be $2.5\pm1\times10^{-8}$ [23](WASO 17 – WASO 4.2). The first long crystal was prepared from material supplied by Monsanto.

These two samples were chosen because the lattice spacing of the NIST sample has been measured absolutely and the lattice spacing of WASO 17 was measured relative to the WASO 4.2 sample which was measured absolutely at the PTB. In the case of the NIST sample, further refinement of the absolute lattice parameter measurement is continuing [24, 25]. Because the absolute lattice measurements have not yet achieved 0.01 ppm uncertainty, they do not provide as definitive a test of the Δd measurements as is desirable. The published results of the absolute lattice spacing measurements are

[2] Certain commercial equipment, instruments, or materials are identified in this paper to specify adequately the experimental procedure. Such identification does not imply recommendation or endorsement by the National Institute of Standards and Technology, nor does it imply that the materials or equipment identified are necessarily the best available for the purpose.

d_{220}(WASO 4.2) at 22.5 °C = 0.192015560 (12) nm ($\pm 6.2\times10^{-8}$)

d_{220}(NIST) at 22.5 °C = 0.19201554 (2) nm ($\pm 10.4\times10^{-8}$)

which lead to

$$\Delta d/d(\text{NIST-WASO 4.2}) = -1\times10^{-7}\pm1.2\times10^{-7}.$$

In order to develop confidence in the Δd measurements, we have measured the long term reproducibility by recording an extensive set of data over more than one half year during which the crystals were realigned on the spectrometer several times. In addition, measurements were taken using two different wavelengths (Ag Kα and Mo Kα x-ray radiation) and with the long first crystal in the two possible orientations (the 0° and the 180° orientation).

In Fig. 7 the measured values of $\Delta d/d$ are plotted vs time with different symbols for the different sources and different first crystal orientations. Note the long time span over which the Ag Kα, 0° orientation measurements were taken. In Table 1 the average numerical values for the different sources and first crystal orientations are presented. From both the table and the figure, the magnitude of systematic effects related to the source and first crystal orientation is estimated to be $\sim 7\times10^{-9}$. Table 2 provides a summary of uncertainty contributions resulting from systematic effects associated with 1) the wavelength and first crystal orientation, 2) crystal temperature measurements, 3) crystal misalignments, and 4) periodic nonlinearity in the Michelson angle interferometer.

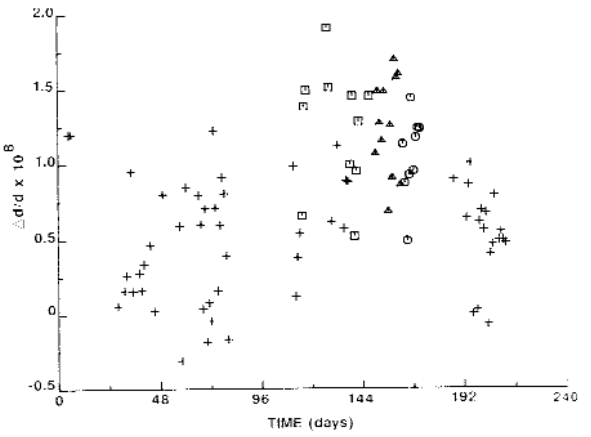

Fig. 7. Comparison of NIST and WASO 17 crystals: + AgKα, first crystal 0°; □ AgKα, first crystal 180°; ⊙ MoKα, first crystal 0°; Δ MoKα, first crystal 180°.

Table 1. Comparison of NIST and WASO 17 samples

Source	First crystal orientation	$\Delta d/d\times10^8$ NIST–WASO 17
Ag Kα	0°	0.508 ± 0.379
Ag Kα	180°	1.236 ± 0.393
Mo Kα	0°	1.050 ± 0.262
Mo Kα	180°	1.251 ± 0.310

Table 2. Estimated uncertainties from systematic effects

Systematic effect	Contribution to $\Delta d/d\times10^8$
λ and 1st crystal orientation	0.7
Temperature	0.3
Crystal misalignment	0.2
Interferometry nonlinearity	0.5

The uncertainty in the measurement of the crystal temperature differences is less than 1 mK. This value was determined by periodically placing all of the thermistors in a constant temperature bath as explained in Sec. 5. A 1 mK uncertainty in the crystal temperature differences leads to an uncertainty of 3×10^{-9} in $\Delta d/d$. The uncertainty introduced by crystal misalignment is discussed in detail in Appendix A and is estimated to be less than 2×10^{-9}.

Heterodyne Michelson interferometers are prone to sub-periodic nonlinearity resulting from imperfect separation of the two frequencies by the primary beam splitter [26, 27]. The periodic nonlinearity can be evaluated by pressure scanning the interferometer and recording the fringe advance vs pressure increase. The maximum amplitude of the nonlinearity is estimated to be 4×10^{-9} rad. This means that the angular separation of two points on a diffraction profile which are separated by 0.5 interferometer fringe (4×10^{-7} rad) might be in error by 8×10^{-9} rad. However, because the profiles are typically 25 interferometer fringes wide, the influence of the interferometer periodic error on the profile peak position is significantly reduced by averaging. In addition, the phase relation of the x-ray profile to the angle interferometer fringes changes so that uncertainty due to periodic nonlinearity becomes part of the statistical uncertainty. We estimate that the uncertainty contribution to $\Delta d/d$ due to the systematic effect associated with the periodic nonlinearity of the angle interferometers is not larger than 5×10^{-9}. The angle interferometer is being modified in order to reduce the periodic nonlinearity by approximately a factor of 5.

A final value for the NIST-WASO 17 comparison was obtained by considering each of the entries in Table 1 to be an independent measurement of equal weight. The statistical uncertainty was combined with the uncertainties from systematic effects in Table 2 to obtain a value for $\Delta d/d$ (NIST-WASO 17) $= (1.037 \pm 1.0) \times 10^{-8}$. By combining this value with the WASO 17-WASO 4.2 difference noted above, one obtains

$$\Delta d/d \text{ (NIST-WASO 4.2)} = (3.5 \pm 1.4) \times 10^{-8}.$$

This value is only slightly outside the 1 σ uncertainty of the absolute measurements. In addition, it should be remembered that the NIST absolute value is a preliminary result.

8. Conclusions

A lattice comparison facility has been established at NIST which is capable of measuring crystal lattice spacing difference with an uncertainty < 0.01 ppm. By using crystals of equal thickness, the recorded profiles exhibit fine structure which permits more precise measurement of the small angular offsets between profiles. The spectrometer is designed to permit easy interchange of crystal samples and the comparison of four samples in one setup. Procedures are provided for precise alignment of the crystals so that alignment errors contribute $< 2 \times 10^{-9}$. A comparison of samples whose lattice spacings have been absolutely measured is consistent with the absolute measurements. In th near future other crystal samples (including Ge destined for x- and gamma-ray diffraction will b compared using the spectrometer and the tech nique described here.

9. Appendix A. Derivation of th Equation for Calculation of Δd

If the lattice planes in crystal 1 and 2 are a perfectly parallel with the axis of rotation and th x-ray beams lie in a plane normal to the axis o rotation, then the difference in lattice spacing be tween crystal 1 and 2 can be derived from Bragg' law (see Sec. 2). In reality, however, the alignmer of the crystals and/or the x-ray beams is never per fect. In this appendix, equations for the calculatio of Δd which include misalignment terms ar derived. The x-ray beams are described b wavevectors, $\boldsymbol{k}$, and the crystals are described b reciprocal vectors, $\boldsymbol{\tau}$. The derivation is based o the fact that the angular positions, θ_+ and θ_-, o the symmetric rocking curve profiles, measure along path (+) and path (−) in the two crysta spectrometer, are equal to the two particular rota tion angles θ, for which the Laue-conditions fo path (+) and path (−), are simultaneously satis fied at crystal 1 and 2 (see Figs. 8 and 9).

Larson [28] has made a similar geometrical anal ysis of a lattice parameter comparison using Brag geometry. We first derive the equation for $\Delta d/d$ fo the ideal case involving perfect crystals and no mis alignment of the crystals or the x-ray beams. Th

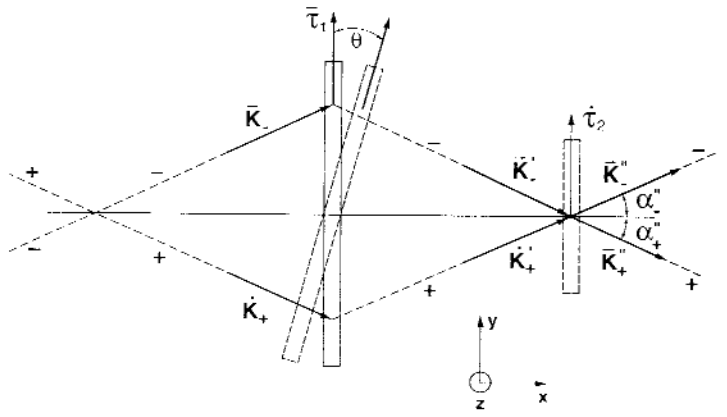

Fig. 8. Geometry of the lattice parameter measurement with no crystal misalignment.

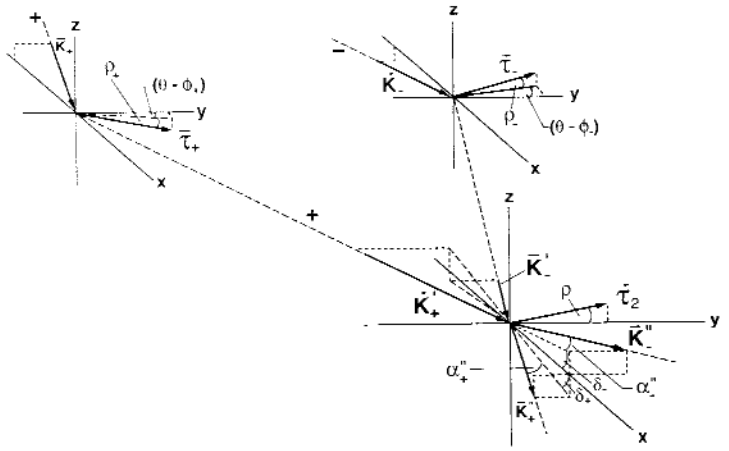

Fig. 9. Geometry of the lattice parameter measurement including crystal misalignment.

more experienced reader may choose to skip over this section. Next, we derive the equations for the nonideal case and apply them to "alignment scans" and "data scans."

9.1 Ideal Case

First consider the ideal case of no misalignment of the x-ray beams or tilting of the crystals. The geometry of the measurement is then entirely confined to the xy plane and is as shown in Fig. 8. The coordinate system is such that the z-axis is parallel to the θ-axis (i.e., the axis of the rotating table), the x-axis is parallel to the lattice planes of interest in crystal 2, the y-axis is normal to the lattice planes in crystal 2, and the normal to the lattice planes in crystal 1 lies in the xy plane. The rotation angle reference is taken to be the y-axis and the θ's, the angles of rotation of the first crystal, are positive for clockwise rotation and negative for counterclockwise rotation.

The x-ray beams are described by their wave vectors: $\boldsymbol{k}_-$, $\boldsymbol{k}_+$ for the incident rays; $\boldsymbol{k}'_-$, $\boldsymbol{k}'_+$ for the singly diffracted rays; and $\boldsymbol{k}''_-$, $\boldsymbol{k}''_+$ for the double diffracted rays. Using the angles shown in Fig. 8, the doubly diffracted rays can be written as

$$\boldsymbol{k}''_- = 2\pi/\lambda(\cos\alpha''_-,\ \sin\alpha''_-,\ 0),$$

$$\boldsymbol{k}''_- = 2\pi/\lambda(\cos\alpha''_+,\ \sin\alpha''_+,\ 0).$$

The crystals are described by their reciprocal lattice vectors $\tau_1(\theta)$ for crystal 1 and τ_2 for crystal 2 which can be written as

$$\tau_1(\theta) = \frac{2\pi}{d_1}\ (\sin\theta,\ \cos\theta,\ 0),$$

$$\tau_2 = \frac{2\pi}{d_2}\ (0,1,0).$$

The planes at the two ends of crystal 1 are assumed to be parallel and to have the same lattice spacing. When the Laue condition is satisfied at crystal 1

$$\boldsymbol{k}'_- - \boldsymbol{k}_- = -\tau_1(\theta_-) \text{ and } \boldsymbol{k}'_+ - \boldsymbol{k}_+ = \tau_1(\theta_+). \quad (3)$$

Similarly when the Laue condition is satisfied at crystal 2

$$\boldsymbol{k}''_- - \boldsymbol{k}'_- = \tau_2 \text{ and } \boldsymbol{k}''_+ - \boldsymbol{k}'_+ = -\tau_2. \quad (4)$$

Since the wave vectors have equal magnitude, $2\pi/\lambda$, Eqs. (3 and 4) imply

$$\tau_1(\theta_-)\cdot(\tau_2 - \boldsymbol{k}''_-) \frac{1}{2}|\tau_1(\theta_-)|^2 \text{ and } \tau_1(\theta_+)\cdot(\tau_2 + \boldsymbol{k}''_+) = \frac{1}{2}|\tau_1(\theta_+)|^2. \quad (5)$$

By substituting the reciprocal lattice vectors and the wave vector with $\alpha''_- = \alpha''_+ = \theta_{B2}$ = Bragg angle at the crystal 2 into Eq. (5) and using the Bragg equation, $\lambda = 2d_2 \sin\theta_2$, to eliminate the wavelength, two equations for the lattice spacing difference are obtained.

$$\frac{d_2-d_1}{d_1} = -\sin\theta_-\cot\theta_{B2} - (1-\cos\theta_-) \approx$$

$$-\theta_-\cot\theta_{B2} - \frac{1}{2}\theta_-^2$$

$$\frac{d_2-d_1}{d_1} = -\sin\theta_+\cot\theta_{B2} - (1-\cos\theta_+) \approx$$

$$\theta_+\cot\theta_{B2} - \frac{1}{2}\theta_+^2$$

where terms up to second order in $\theta_\pm$ have been retained. These two equations can be added to obtain

$$\frac{d_2-d_1}{d_1} = -\frac{(\theta_- - \theta_+)}{2}\cot\theta_{B2} - \frac{1}{8}(\theta_- - \theta_+)^2, \quad (6)$$

where we have used the fact that $\theta_+ = -\theta_-$.

For comparisons in which the first and second crystal are made out of the same material $[(d_2-d_1)/d_1 < 10^{-5}]$, the last term is negligible as the following inequality shows

$$10^{-10} > \left|\frac{d_2-d_1}{d_1}\right|^2 > \frac{1}{2}\left|\frac{d_2-d_1}{d_1}\right|^2 \tan^2\theta_{B2} \approx$$

$$\frac{1}{8}(\theta_- - \theta_+)^2, \text{ if } \theta_{B2} < 54°.$$

If crystal 2 is alternately the standard and unknown crystal, the Eq. (6) becomes

$$\frac{d_s-d_1}{d_1} \approx -\frac{\beta_s}{2}\cot\theta_{Bs} \text{ where } \beta_s = \theta_{-s} - \theta_{+s}$$

$$\frac{d_u-d_1}{d_1} \approx -\frac{\beta_u}{2}\cot\theta_{Bu} \text{ where } \beta_u = \theta_{-u} - \theta_{+u}$$

These two equations immediately lead to Eq. (2).

$$\frac{d_s-d_u}{d_1} \approx -\frac{\beta_s-\beta_u}{2}\cot\theta_{Bs} \quad (7)$$

9.2 Non-Ideal Case

Misalignment of the planes of crystals 1 and 2 with respect to the rotation axis, imperfections in the first crystal (i.e., lattice spacing gradient and nonparallelism of the planes at the two ends of the crystal), and the misalignment of the x-ray beams with respect to the plane normal to the rotation axis introduce correction terms to the measured lattice spacing difference. In the analysis which takes into account misalignments and crystal imperfections, the geometry of Fig. 9 is used.

The coordinate system is identical to that used for the ideal case, i.e., the z axis is parallel to the axis of rotation and the x axis parallel to the lattice planes in crystal 2. However, the wave and reciprocal lattice vectors no longer lie in the xy plane. The wave vector of the double diffracted x-rays can be put in the following form:

$$\boldsymbol{k}''_\pm = \frac{2\pi}{\lambda}(\cos\alpha_\pm \cos\delta_\pm, \mp\sin\alpha_\pm, \cos\alpha_\pm \sin\delta_\pm), \quad (8)$$

where $\delta_\pm$ is the angle between the xy plane and the projection of the wavevector $\boldsymbol{k}''_\pm$ on the xz plane.

The reciprocal lattice vectors associated with path $(+)$ and path $(-)$ in crystal 1, τ_+ and τ_-, are no longer parallel and of equal magnitude. The two vectors $\tau_\pm$ can be described by the six parameters $d_\pm$, $\rho_\pm$ and $\theta_\pm$ as follows:

$$\boldsymbol{\tau}_\pm = \frac{2\pi}{d_\pm}(\sin(\theta - \phi_\pm)\cos\rho_\pm,$$

$$\cos(\theta - \phi_\pm)\cos\rho_\pm, \sin\rho_\pm), \quad (9)$$

where $d_\pm$ is the lattice spacing in the diffracting region of crystal 1 corresponding to path $(\pm)$, $\rho_\pm$ is the angle between $\tau_\pm$ and the xy-plane, and $\phi_\pm$ is the particular angle of rotation θ for which $\tau_\pm$ is parallel to the yz plane. For a perfect first crystal, $d_+ = d_-$, $\rho_+ = \rho_-$, and $\phi_+ = \phi_-$. In crystal 2 the reciprocal lattice vector, τ_2, is the same for both paths and is given by

$$\boldsymbol{\tau}_2 = \frac{2\pi}{d_2}(0, \cos\rho, \sin\rho), \quad (10)$$

where d_2 is the lattice spacing in the diffracting region of crystal 2, and ρ is the angle between τ_2 and xy-plane. Note that τ_2 is in the yz plane.

For path $(\pm)$, the relations between the wave vectors $\boldsymbol{k}_\pm$ of the incident rays, $\boldsymbol{k}'_\pm$ of the single diffracted rays, and $\boldsymbol{k}''_\pm$ of the double diffracted rays are given by the Laue conditions:

$$\boldsymbol{k}'_\pm - \boldsymbol{k}_\pm = \pm\boldsymbol{\tau}_\pm \quad \text{(crystal 1)} \quad (11)$$

$$\boldsymbol{k}''_\pm - \boldsymbol{k}'_\pm = \mp\boldsymbol{\tau}_2 \quad \text{(crystal 2)} \quad (12)$$

Since the wave vectors have equal magnitude, $2\pi/\lambda$, Eqs. (11) and (12) imply that

$$\boldsymbol{\tau}_2 \cdot \boldsymbol{k}''_{\pm} = \mp\frac{1}{2}|\boldsymbol{\tau}_2|^2 \tag{13}$$

$$\boldsymbol{\tau}_{\pm} \cdot (\boldsymbol{\tau}_2 \pm \boldsymbol{k}''_{\pm}) = \frac{1}{2}|\boldsymbol{\tau}_{\pm}|^2. \tag{14}$$

When the Laue condition is satisfied at crystal 2, the angles, $\alpha_{\pm}$, can be expressed as $\alpha_{\pm} = \theta_{B2} + \epsilon_{\pm}$ where $\epsilon_{\pm}$ are the small angular corrections to the second crystal Bragg angle because of crystal imperfections and misalignments. Thus Eq. (8) becomes

$$\boldsymbol{k}''_{\pm} = \frac{2\pi}{\lambda}\,(\cos(\theta_{B2}+\epsilon_{\pm})\cos\delta_{\pm},$$

$$\mp\sin(\theta_{B2}+\epsilon_{\pm}),\ \cos(\theta_{B2}+\epsilon_{\pm})\sin\delta_{\pm}). \tag{15}$$

In order to establish a relation between the lattice spacing d of crystal 2 and the rotation angles $\theta = \theta_{\pm}$, for which the Laue-conditions corresponding to path $(\pm)$ are simultaneously satisfied at crystal 1 and crystal 2, Eqs. (9), (10), and (15) are expanded to second order in the angles $\theta_{\pm} - \phi_{\pm}$, $\rho_{\pm}$, ρ and $\delta_{\pm}$ and to first order in the correction angle $\epsilon_{\pm}$:

$$\boldsymbol{\tau}_{\pm} = \frac{2\pi}{d_{\pm}}\,(\theta_{\pm}-\phi_{\pm},\ 1-\frac{1}{2}(\theta_{\pm}-\phi_{\pm})^2-\frac{1}{2}\rho_{\pm}^2,\ \rho_{\pm}) \tag{16}$$

$$\boldsymbol{\tau}_2 = \frac{2\pi}{d_2}\,(0,\ 1-\frac{1}{2}\rho^2,\ \rho) \tag{17}$$

$$\boldsymbol{k}''_{\pm} = \frac{\pi}{d_2}\left((1-\frac{1}{2}\delta_{\pm}^2)\cot\theta_{B2}-\epsilon_{\pm},\ \mp 1 \mp \epsilon_{\pm}\cot\theta_{B2},\right.$$

$$\left.\delta_{\pm}\cot\theta_{B2}\right). \tag{18}$$

In the last equation, the wavelength λ has been eliminated using $\lambda = 2d_2\sin\theta_{B2}$. By insertion of Eqs. (17) and (18) into Eq. (13), an expression for the correction angles $\epsilon_{\pm}$ is easily obtained:

$$\epsilon_{\pm} = \frac{1}{2}\rho^2\tan\theta_B \pm \rho\delta_{\pm}\ . \tag{19}$$

Now by inserting Eqs. (16), (17), (18), and (19) into Eq. (14) the following equation can be derived:

$$\frac{d_2 - d_{\pm}}{d_{\pm}} = \pm(\theta_{\pm}-\phi_{\pm})\cot\theta_B + e_{\pm}\ , \tag{20}$$

where $e_{\pm}$ is the second order correction term

$$e_{\pm} = -\frac{1}{2}(\theta_{\pm}-\phi_{\pm})^2 - \frac{1}{2}(\rho_{\pm}-\rho)(\rho_{\pm}-3\rho)$$

$$\pm\delta_{\pm}(\rho_{\pm}-\rho)\cot\theta_{B2}\ . \tag{21}$$

The angle $\delta_{\pm}$ in Eq. (21) describes the inclination of the double diffracted beam relative to the xy-plane, (see Fig. 9). If crystal 1 and crystal 2 are perfectly parallel, the wavevectors $\boldsymbol{k}_{\pm}$, $\boldsymbol{k}'_{\pm}$, and $\boldsymbol{k}''_{\pm}$ are coplanar and the inclinations $\delta_{\pm}$ are determined simply by the positions of the source and detector slits. When the two crystals are not perfectly parallel, $\delta_{\pm}$ are also dependent on the misalignment angles $\rho_{\pm}$ and ρ.

Let ℓ, ℓ', and ℓ'' be projections along the x-axis of the x-ray paths from the source slit to crystal 1, from crystal 1 to crystal 2, and from crystal 2 to the detector slit, respectively. The distances are shown in Fig. 1 and for our spectrometer are:

$$\ell = (25.4\cos\theta_B + 8.25)\ \text{cm}$$
$$\ell' = 8.25\ \text{cm}$$
$$\ell'' = (28.5\cos\theta_B)\ \text{cm}$$

If $\Delta Z_{\pm}$ denotes the difference in Z-coordinate between the detector slit and source slit of path $(\pm)$, then the inclination $\Delta_{\pm}$ relative to the xy-plane of the straight line joining the two slits is given by:

$$\Delta_{\pm} = \frac{\Delta Z_{\pm}}{\ell + \ell' + \ell''}\ . \tag{22}$$

The change in Z-coordinate as one moves from the source slit to the detector slit along path $(\pm)$ can be expressed by combining the Z-components of the wave vectors $\boldsymbol{k}_{\pm}$, $\boldsymbol{k}'_{\pm}$, and $\boldsymbol{k}''_{\pm}$, normalized to unity and the distances traveled:

$$\Delta Z_{\pm} = \frac{\lambda}{2\pi}\left[(\boldsymbol{k}_{\pm})_z\ell + (\boldsymbol{k}'_{\pm})_z\ell' + (\boldsymbol{k}''_{\pm})_z\ell''\right]$$

$$\frac{1}{\cos\theta_B}\ . \tag{23}$$

From Eqs. (11), (12), and (15) and using Eqs. (9) and (10), the Z-components of the wave vectors are found to second order in $\rho_\pm$, ρ, and $\delta_\pm$:

$$\frac{\lambda}{2\pi}(\boldsymbol{k}_\pm)_z = \delta_\pm \cos\theta_B \pm 2(\rho-\rho_\pm)\sin\theta_B \qquad (24)$$

$$\frac{\lambda}{2\pi}(\boldsymbol{k}'_\pm)_z = \delta_\pm \cos\theta_B \pm 2\rho \sin\theta_B \qquad (25)$$

$$\frac{\lambda}{2\pi}(\boldsymbol{k}''_\pm)_z = \delta_\pm \cos\theta_B . \qquad (26)$$

By insertion of Eqs. (22), (24), (25), and (26) into Eq. (23) a relation between $\delta_\pm$ and $\Delta_\pm$ is obtained:

$$\delta_\pm = \Delta_\pm \pm 2\left(\frac{\ell}{\ell+\ell'+\ell''}\rho_\pm - \frac{\ell+\ell'}{\ell+\ell'+\ell''}\rho\right)\tan\theta_B .$$

Using this expression, the unknown angles $\delta_\pm$ can be eliminated from Eq. (21):

$$e_\pm = -\frac{1}{2}(\theta_\pm-\phi_\pm)^2 + 2(\rho_\pm-\rho)(a_1\rho_\pm + b_1\rho) \pm \Delta_\pm(\rho_\pm-\rho)\cot\theta_B \qquad (27)$$

where

$$a_1 = \frac{\ell}{\ell+\ell'+\ell''} - \frac{1}{4} = 0.23$$

$$b_1 = \frac{\ell''}{\ell+\ell'+\ell''} - \frac{1}{4} = 0.15 .$$

Even though the distances ℓ and ℓ'' depend on the Bragg angle θ_B, the numerical values for a_1 and b_1 are essentially identical for the two x-ray sources ($\theta_B = 16.9°$ for Ag Kα_1 and $\theta_B = 21.6°$ for Mo Kα_1).

When crystal 1 and 2 are both of the same material, an upper limit of the first term in Eq. (27) is easily estimated:

$$\frac{1}{2}(\theta_\pm-\phi_\pm)^2 < \left|\frac{d-d_\pm}{d_\pm}\right|^2 < 10^{-10}$$

$$10^{-10} > \left|\frac{d-d_\pm}{d_\pm}\right|^2 > \frac{1}{2}\left|\frac{d-d_\pm}{d_\pm}\right|^2 \tan^2\theta_B \approx \frac{1}{2}(\theta_\pm-\phi_\pm)^2,$$

if $\theta_B < 54°$.

This term is two orders of magnitude smaller than the intended uncertainty (a few parts in 10^8) in the lattice spacing comparison and is therefore neglected in the following. The remaining two terms in Eq. (27) are both zero, if the lattice planes in crystal 1 and 2 are parallel, i.e., $\rho_+ - \rho = 0$ and $\rho_- - \rho = 0$. The aim of the alignment scan is to measure $\rho_+ - \rho$ and $\rho_- - \rho$ and then to adjust the tip of crystal 2 so as to make $\rho_+ - \rho$ and $\rho_- - \rho$ as close to zero as possible.

9.2.1 The Alignment Scan In the alignment scan, only one path, path (+) or path (−), is used. Two rocking curves are measured simultaneously: one curve using the upper (up) position and one using the lower (lo) position of the detector slit. For the path (−), the observed difference $\Delta\theta_-$ in the centers of the two rocking curves ($\Delta\theta_- = \theta_{-\mathrm{up}} - \theta_{-\mathrm{lo}}$), the change in the inclination ($\Delta_{-\mathrm{up}} - \Delta_{-\mathrm{lo}}$) when the detector slit is moved from the upper to the lower position, and the difference in misalignment of the two crystals, $\rho_- - \rho$, are related. The following equation is derived directly from Eqs. (20) and (27):

$$\rho_- - \rho = \frac{-\Delta\theta_-}{\Delta_{-\mathrm{up}} - \Delta_{-\mathrm{lo}}} . \qquad (28)$$

Similarly, for path (+) it follows that

$$\rho_+ - \rho = \frac{-\Delta\theta_+}{\Delta_{+\mathrm{up}} - \Delta_{+\mathrm{lo}}} \qquad (29)$$

($\Delta_{-\mathrm{up}} - \Delta_{-\mathrm{lo}}$) and ($\Delta_{+\mathrm{up}} - \Delta_{+\mathrm{lo}}$) can be estimated from mechanical measurements of the spectrometer and are $\sim 9\times10^{-3}$ rad. Due to bending of crystal 1, ρ_+ and ρ_- are not equal. Consequently, the sample crystal can only be aligned for one of the two paths. If the tilt of crystal 2 is adjusted so that $|\Delta\theta_-| \approx 2\times10^{-8}$ rad, then typical values for $|\Delta\theta_+|$ are 1×10^{-7} rad. These values imply that

$$|\rho_- - \rho| \approx 2\times10^{-6}$$

$$|\rho_+ - \rho| \approx 1\times10^{-5} .$$

The magnitude of the individual ρ's can also be controlled and estimated. By rotating the 1st crystal by 180°, the tilt of the first crystal can be adjusted so that ρ_+ and ρ_- are $< 1\times10^{-5}$ rad.

9.2.2 The Data-Taking Scan In the data-taking scan, two rocking curves are simultaneously measured with the detector slits fixed in the middle position: one curve using path (+), and one using

path (−). We define the average lattice spacing, d_1, in crystal 1 as

$$d_1 = \frac{2d_+d_-}{d_+ + d_-},$$

and average Eqs. (20) and (27) over path (+) and path (−) to obtain

$$\frac{d_2 - d_1}{d_1} = \frac{1}{2}(\theta_+ - \theta_- + \eta_0)\cot\theta_B + e, \tag{30}$$

where

$$e = \{(\rho_+ - \rho)(a_1\rho_+ + b_1\rho) + (\rho_- - \rho)(a_1\rho_- + b_1\rho)\} +$$

$$\frac{1}{2}\{\Delta_+(\rho_+ - \rho) - \Delta_-(\rho_- - \rho)\}\cot\theta_B \tag{31}$$

and

$$\eta_0 = \phi_- - \phi_+. \tag{32}$$

The angle η_0 describes a bending of crystal 1 around the θ-axis and is independent of the particular sample used as crystal 2. Obviously, the appearance of the unknown angle η_0 in Eq. (30) excludes the possibility of using crystal 1 as an absolute reference crystal.

The two crystals being compared are placed on the translation table and are used alternately as crystal 2. One of the crystals serves as the standard (s) and one as the unknown (u). The difference in lattice spacing, $\Delta d = d_s - d_u$ for the two sample crystals can be derived from Eqs. (30) and (31).

$$\frac{\Delta d}{d_1} = -\left(\frac{\beta_s - \beta_u}{2}\right)\cot\theta_B + \Delta e \tag{33}$$

where:

$$\beta_s = \theta_{-s} - \theta_{+s}$$

$$\beta_u = \theta_{-u} - \theta_{+u}$$

$$\Delta e = [a_2(\rho_+ + \rho_-) + b_2(\rho_s + \rho_u) - \frac{1}{2}$$

$$(\Delta_+ - \Delta_-)\cot\theta_B]\,(\rho_s - \rho_u) =$$

$$[a_2(\rho_+ + \rho_-) + 2b_2\rho_u - \frac{1}{2}(\Delta_+ - \Delta_-)\cot\theta_B]$$

$$(\rho_s - \rho_u) + b_2\,(\rho_s - \rho_u)^2, \tag{34}$$

where $a_2 = b_1 - a_1 = -0.08$ and $b_2 = -2b_1 = -0.30$.

In order to make Δe small, the tilts of the crystals are adjusted so that ρ's are $< 1 \times 10^{-5}$ (see Sec. 9.2.1). Care is taken to center the source and detector slits on the plane of dispersion in order to make $\Delta_+ - \Delta_-$ small, but mechanical measurements suggest that the magnitude of the Δ's is $\lesssim 3 \times 10^{-4}$. The correction term can be estimated by measuring $(\beta_s - \beta_u)$ as a function of $(\rho_s - \rho_u)$ where ρ_u is kept fixed and ρ_s is varied. For $\rho_s - \rho_u \lesssim 5 \times 10^{-5}$, Eqs. (33) and (34) can be approximated by

$$\frac{\Delta d}{d_1} = -\left(\frac{\beta_s - \beta_u}{2}\right)\cot\theta_B + C(\rho_s - \rho_u)$$

where

$$C = a_2(\rho_+ + \rho_-) + 2b_2\rho_u - \frac{1}{2}(\Delta_+ - \Delta_-)\cot\theta_B.$$

A plot of $(\beta_s - \beta_u)$ vs $(\rho_s - \rho_u)$ is shown in Fig. 10 and has an approximate slope of -3.6×10^{-4} in reasonable agreement with the estimates of the Δ's from the mechanical measurements and the estimates of the individual ρ's.

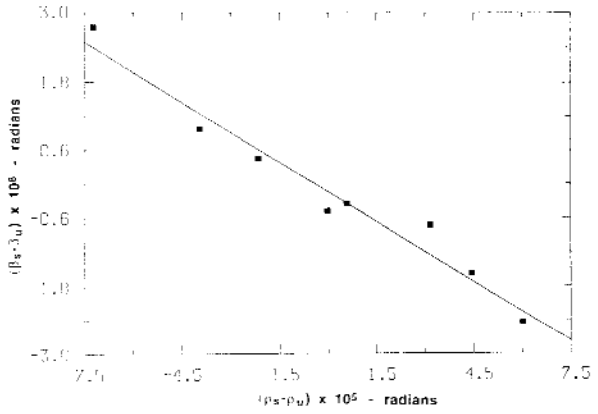

Fig. 10. Measured data profile offsets, $\beta_s - \beta_u$, as a function of the measured crystal tilts $(\rho_s - \rho_u)$. See text for more explanation.

Before and after data scans are recorded using a standard and unknown crystal, alignment scans are recorded for the standard and unknown crystal also. The quantity $\rho_s - \rho_u$ is determined from the alignment scans and is maintained at a value $< 4 \times 10^{-6}$ rad. Thus the correction term $\Delta e < 2 \times 10^{-9}$. Correction of the data for measured values of Δe does not reduce the statistical spread of repeated measurements. We have thus chosen to increase the relative uncertainty of the final results by 2×10^{-9}, but not to correct individual measurements. Although the correction term is small, it could be reduced by an order of magnitude by making the source and

detector slits adjustable about the plane of dispersion. Modifications to the spectrometer to permit this adjustment are in progress.

10. Appendix B. Electronics Associated with the Interferometer

The layout of the Michelson angle interferometers is shown in Fig. 2 and is briefly described in Sec. 3. In this appendix the electronics used to measure the whole and fractional fringes and to servo-control the rotation axes are described. A block diagram of the electronics is provided in Fig. 11.

The 1.8 MHz TTL level signals from the laser and the detector are first converted to low impedance signals by buffer amplifiers. The laser beat signal is then passed through a 2-way 90° splitter with 0° and 90° split yielding sin (ωt) and cos (ωt), respectively. The detector beat signal is passed through a 2-way 0° splitter yielding two sin ($\omega t + \phi$) signals. The laser's cos (ωt) and one of the detector's sin ($\omega t + \phi$) are combined in a mixer which gives signals at the sum and difference frequencies. The difference frequency signal is sin ϕ and the sum frequency signal is sin ($2\omega t + \phi$) which is attenuated by a low pass filter. Meanwhile the sin (ωt) from the laser is combined with the other sin ($\omega t + \phi$) of the detector in another mixer which after filtering gives cos ϕ. The sin ϕ and cos ϕ signals are next amplified to restore their signal strengths which have deteriorated due to losses in the splitters, mixers, and filters.

Ninety degree changes in ϕ which correspond to ~ 0.04 second rotation of the rotary table are detected by sending the sin ϕ and cos ϕ signals to an up/down counter. Smaller changes in ϕ are measured by comparing ϕ to a standard angular signal (sin θ and cos θ) obtained as the output of a digital vector generator. A vector generator with a few 0.1° sensitivity provides a total angular sensitivity of a few $\times 10^{-4}$ seconds with the vector generator address being directly related to the fringe fraction. By taking the difference of the product of sin ϕ and cos θ and the product of cos ϕ and sin θ the signal $\sin(\phi - \theta)$ is obtained. This is an appropriate error signal for locking the angle of the rotary table via a piezoelectric transducer to the position where $\phi = \theta$.

11. References

[1] P. Becker, K. Dorenwendt, G. Ebeling, R. Lauer, W. Lucas, R. Probst, H.-J. Radenmacher, G. Reim, P. Seyfried, and H. Siegert, Absolute Measurement of the (220) Lattice Plane Spacing in a Silicon Crystal, Phys. Rev. Lett. **46**, 1540–1543 (1981).

[2] R. D. Deslattes and A. Henins, X-Ray to Visible Wavelength Ratios, Phys. Rev. Lett. **31**, 972–975 (1973).

[3] R. D. Deslattes, A. Henins, H. A. Bowman, R. M. Schoonover, C. L. Carroll, I. L. Barnes, L. A. Machlan, L. J. Moore, and W. R. Shields, Determination of the Avogadro Constant, Phys. Rev. Lett. **33**, 463 (1974); R. D. Deslattes, A. Henins, R. M. Schoonover, C. L. Carroll, and H. A. Bowman, Avogadro Constant-Corrections to an Earlier Report, Phys. Rev. Lett. Comm. **36**, 898–900 (1976).

[4] R. D. Deslattes, E. G. Kessler, W. C. Sauder, and A. Henins, Remeasurement of γ-Ray Reference Lines, Ann. Phys. **129**, 378 (1980).

[5] G. Basile, A. Bergamin, G. Cavagnero, G. Mana, E. Vittone, and G. Zosi, Silicon Lattice Constant: Limits in IMGC X-Ray/Optical Interferometry, IEEE Trans. Instrum. Meas. **40**, 98–102 (1991).

[6] M. Tanaka, K. Nakayama, and K. Kuroda, Experiment on the Absolute Measurement of a Silicon Lattice Spacing at the NRLM, IEEE Trans. Instrum. Meas. **38**, 206–209 (1989).

[7] M. Hart, High Precision Lattice Parameter Measurements by Multiple Bragg Reflexion Diffractometry, Proc. Roy. Soc. London Ser. A **309**, 281–296 (1969).

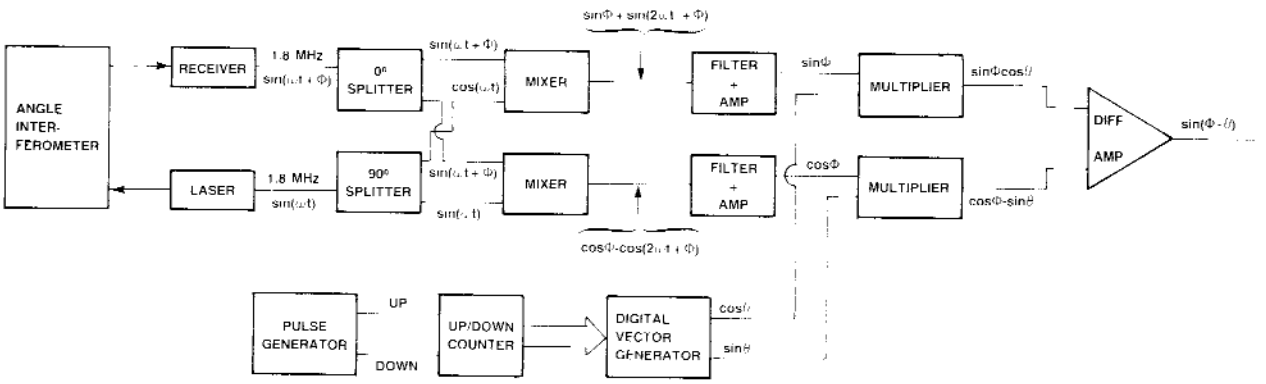

Fig. 11. Block diagram of electronics used to measure whole and fractional fringes.

[8] M. Ando, D. Bailey, and M. Hart, A Simple Bragg-Spacing Comparator, Acta Cryst. A **34**, 484–489 (1978).
[9] P. Becker, P. Seyfried, and H. Siegert, The Lattice Parameter of Highly Pure Silicon Single Crystals, Z. Phys. B **48**, 17–21 (1982).
[10] D. Haüsermann and M. Hart, A Fast High-Accuracy Lattice-Parameter Comparator. J. Appl. Cryst. **23**, 63–69 (1990).
[11] The rotary table is an "Ultraron Rotary Table," Model No. UR-6 supplied by A. A. Gage Inc., Detroit, Michigan.
[12] The laser is a Model 5501A laser transducer, supplied by Hewlett Packard, Santa Clara, California.
[13] The slide is a Model 7-6 Anoride Table supplied by Anorad Corporation, Hauppauge, New York.
[14] M. Deutsch and M. Hart, Electronic Charge Distribution in Silicon, Phys. Rev. B **31**, 3846–3858 (1985).
[15] R. Teworte and U. Bonse, High-Precision Determination of Structure Factors F_h of Silicon, Phys. Rev. B **29**, 2102–2108 (1984).
[16] M. Deutsch, M. Hart, and S. Cummings, High-Accuracy Structure-Factor Measurements in Germanium, Phy. Rev. B **42**, 1248–1253 (1990).
[17] M. Deutsch and M. Hart, X-Ray Refractive-Index Measurement in Silicon and Lithium Fluoride, Phy. Rev. B **30**, 640–642 (1984).
[18] U. Bonse, W. Graeff, R. Teworte, and H. Rauch, Oscillatory Structure of Laue Case Rocking Curves, Phy. Stat. Sol. **43**, 487–492 (1977).
[19] U. Bonse, and W. Graeff, X-Ray and Neutron Interferometry, in X-Ray Optics, H. J. Queisser, ed., Springer, Berlin (1977), pp. 93–143.
[20] The grinding solution is CAB-O-SPERSE SC-3010 supplied by Cabot Corporation, Tuscola, Illinois.
[21] We are indebted to B. Borchert, R. Veale, and W. Gallagher of the NIST Automated Manufacturing and Research Division for making coordinate measuring machines available for these measurements.
[22] We are indebted to N. Belecki and R. Green of the NIST Electricity Division for calibrating the standard resistor.
[23] D. Windisch and P. Becker, Silicon Lattice Parameters as an Absolute Scale of Length for High Precision Measurements of Fundamental Constants, Phys. Stat. Sol. (a) **118**, 379–388 (1990).
[24] R. D. Deslattes, X-Ray Interferometry and γ-Ray Wavelengths, in The Art of Measurement, B. Kramer, ed., Weinheim, Germany: VCH Verlogsgesellschaft (1988), pp. 193–208.
[25] R. D. Deslattes and E. G. Kessler, Jr., Status of a Silicon Lattice Measurement and Dissemination Exercise, IEEE Trans. Instrum. Meas. **40**, 92–97 (1991).
[26] C. M. Sutton, Nonlinearity in Length Measurement Using Heterodyne Laser Michelson Interferometry, J. Phys. E: Sci. Instrum. **20**, 1290–1292 (1987).
[27] N. Bobroff, Residual Errors in Laser Interferometry from Air Turbulence and Nonlinearity, Appl. Opt. **26**, 2676–2682 (1987).
[28] B. C. Larson, High-Precision Measurements of Lattice Parameter Changes in Neutron-Irradiated Copper, J. Appl. Phys. **45**, 514–518 (1974).

About the authors: *Ernest G. Kessler and Albert Henins are physicists in the Quantum Metrology Division of the NIST Physics Laboratory. Richard D. Deslattes is a Senior NIST Research Fellow and Chief of the Quantum Metrology Division of the NIST Physics Laboratory. Lars Nielsen is employed by the Danish Institute of Fundamental Metrology and participated in this work when he was a guest scientist in the Quantum Metrology Division. Mohammad Arif, a physicist, was in the Quantum Metrology Division when this work wad done and is now in the Ionizing Radiation Division of the NIST Physics Laboratory. The National Institute of Standards and Technology is an agency of the Technology Administration, U.S. Department of Commerce.*

Volume 99, Number 1, January–February 1994
Journal of Research of the National Institute of Standards and Technology

[J. Res. Natl. Inst. Stand. Technol. 99, 19 (1994)]

The NIST 30 MHz Linear Measurement System

Volume 99 Number 1 January–February 1994

Jeffrey A. Jargon, Ronald A. Ginley, and Douglas D. Sutton

National Institute of Standards and Technology,
Boulder, CO 80303-3328

An automated linear measurement system (LMS) has been developed to determine the nonlinearity of a tuned 30 MHz power detector over a 6.021 dB range. This detector uses a single thermistor bead design with thermal isolation to obtain nearly linear tracking over a 4:1 change in input power. The nonlinear correction for this change, determined by the LMS, is on the order of 1.00030 (+130 μB) for the detector presently in use. Initial experiments indicate an expanded uncertainty of ±0.138% (±598 μB), which is based upon Type A and Type B components.

Key words: attenuation; automated; calibration; linear; measurement; power; thermistor; uncertainty.

Accepted: November 16, 1993

1. Introduction

There has been a recent interest in and demand for a calibration service at NIST to support rf attenuators and voltage doublers that operate specifically at 30 MHz. The first step required to offer such a service is to develop a reference standard. For the best possible accuracy, a tuned single-element thermistor mount was chosen. A linear measurement system was designed and constructed at NIST to calibrate the nonlinearity of this mount. This paper contains a description of the LMS, an explanation of the measurement scheme, calibration results, and an uncertainty analysis.

2. System Description

A diagram of the system is shown in Fig. 1. The signal generator provides a stable 30 MHz rf signal that is amplified and filtered before the signal is split into two channels. One channel consists of a variable phase shifter and a fixed attenuator. A coaxial switch either terminates the signal with a 50 Ω termination or feeds the signal into a power divider, which splits the signal again. Half of the signal is detected by a single-element thermistor mount, P_1, and the other half is fed into the hybrid. The second channel consists of a variable attenuator. Like the first channel, a coaxial switch either terminates the signal with a 50 Ω load or feeds the signal into a power divider, which splits the signal. Half of the signal is detected by a single-element thermistor mount, P_2, and the other half is fed into the hybrid.

The hybrid takes the sum and difference of the two input signals. The difference is fed into a diode detector to rectify the signal, and then into a null meter. The sum is fed into a coaxial switch, and when the switch is in position 1, the signal is detected by a third thermistor mount, P_3, which is the thermistor to be calibrated.

Each thermistor mount is connected to a NIST Type IV bridge and a digital voltmeter to measure rf power.

The computer controls the signal generator, the digital voltmeters, and the switch controller, and handles the data acquisition and processing through an IEEE-488 bus.

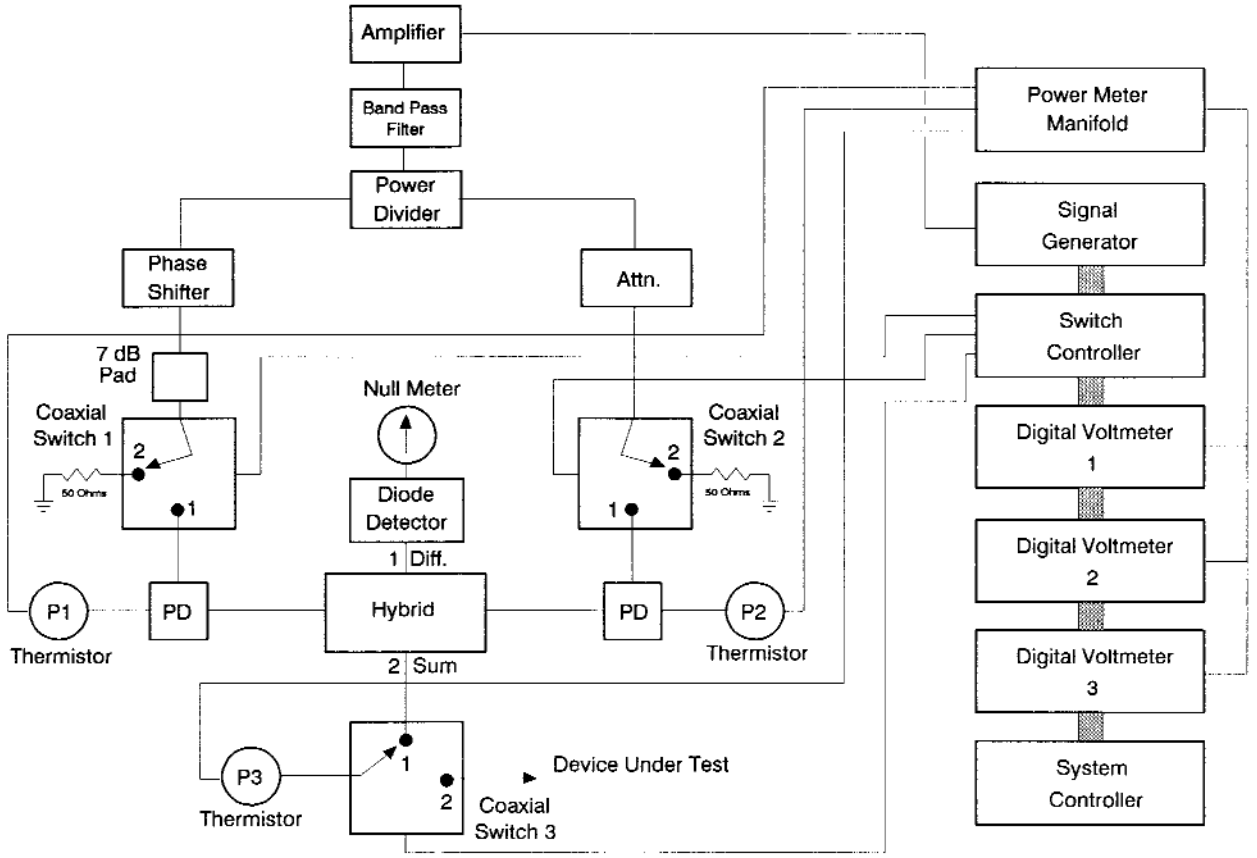

Fig. 1. Block diagram of 30 MHz linear measurement system.

3. Design of 30 MHz Single-Element Thermistor Mount

The dc response of detector P_3 must be nearly linear with changes in input rf power. A single 50 Ω thermistor bead design was selected as a linear detection scheme [1]. This detector is used in conjunction with a NIST Type IV self-balancing dc-substitution rf power meter modified to bias a 50 Ω detector [2]. The Type IV power meter is designed to change the thermistor bead bias current so that the thermistor always maintains the same resistance. The detectors are placed in the LMS housing where the temperature is held to ±0.2 °C.

It is difficult to filter the rf signal from the power meter leads due to the nature of the single bead. The total rf signal should appear across the bead in the ideal case. Other considerations in the detector design include thermal stability and any forms of rf leakage into or out of the detector.

Several ideas are incorporated in the detector to eliminate these problems. Figure 2 shows the circuit diagram of a single-element thermistor mount. LC filter sections are inserted to filter the rf signal in the power meter leads. No ferrite material (such as a ferrite core inductor) is used near the thermistor, since ferrite components experience changes in impedance with changes in the rf power. These impedance changes lead to nonlinearities in the detector response. Therefore, air-cored inductors are inserted near the thermistor. Ferrite-cored conductors are allowable in sections following the first filter section because the rf power is sufficiently reduced and renders any impedance variation negligible. The parallel LC filter is tuned to resonate at 30 MHz. A special thermistor-mounting structure has been developed, and consists of an electrically insulated doughnut and two copper blocks, one on either side of the doughnut. The thermistor is placed inside the doughnut hole and is encapsulated in an air pocket by the addition of the copper blocks. The copper blocks also provide a large thermal mass so that the entire structure cannot experience rapid changes in temperature. The thermal time constant is much longer than the time required to perform a single measurement cycle. Double-sided copper-clad fiberglass boards are used in the exterior detector housing and in the

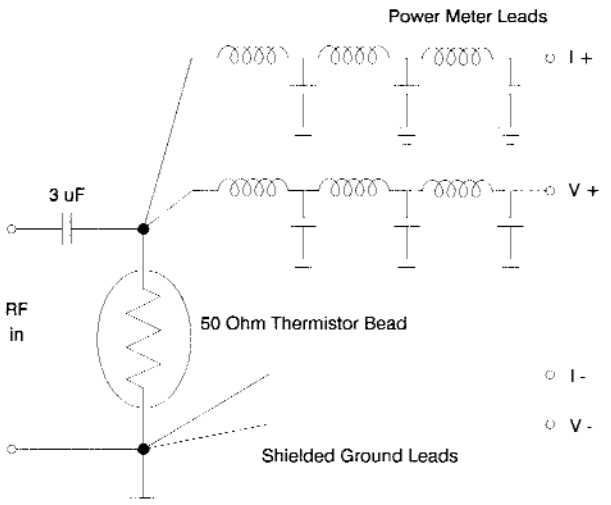

Fig. 2. Circuit diagram of single-element thermistor mount. All inductors are hand-wound and all capacitors are 1 μF unless otherwise labeled.

internal compartment walls which separate various filter sections. This type of construction and the use of capacitive feedthroughs in the compartment walls reduce the amount of rf leakage though the detector. These physical and electrical construction considerations provide a stable linear detector with low rf leakage.

4. Measurement Methods

4.1. Calibration of P_3

Three power meters are used in the LMS—P_1, P_2, and P_3. When a given power meter is read, the notation used is P_{XYZr}, where X denotes the power meter (1, 2, or 3), Y is 1 if channel 1 is switched on and 0 if channel 1 is switched off, Z is 1 if channel 2 is switched on and 0 if channel 2 is switched off, and "r" denotes that this power is a reading and not a true value. Powers without a subscript "r" are true values.

The calibration of P_3 is achieved using a three-stage method. First, with switches 1, 2, and 3 each in position 1, enough power is applied so that a nominal 12 mW is incident on the three thermistor mounts. The phase shifter and variable attenuator are adjusted to balance the two channels, thus obtaining a null on the null meter. Readings are taken on P_1, P_2, and P_3 and are designated P_{111r}, P_{211r}, and P_{311r}, respectively. Next, switch 2 is moved to position 2, so that power is only applied to the first channel. Readings are taken on P_1 and P_3 and are designated P_{110r} and P_{310r}, respectively. A nominal 12 mW will be incident on P_1 and approximately 3 mW will be incident on P_3. Finally, switch 2 is moved back to position 1 and switch 1 is moved to position 2, so that power is only applied to the second channel. Readings are taken on P_2 and P_3 and are designated P_{201r} and P_{301r}, respectively. A nominal 12 mW will be incident on P_2 and approximately 3 mW will be incident on P_3.

The calibration constant of P_3, denoted C^2_{HL}, is calculated using

$$C^2_{HL} = \left[\left(\frac{\frac{P_{310r}}{P_{110r}}}{\frac{P_{311r}}{P_{111r}}} \right)^{1/2} + \left(\frac{\frac{P_{301r}}{P_{201r}}}{\frac{P_{311r}}{P_{211r}}} \right)^{1/2} \right]^2 . \quad (1)$$

The derivation of this formula can be found in Appendix A. The calibration constant is a measure of the detector's nonlinearity over the 6.021 dB power change, and is used as a multiplication factor to correct the ratio measured by P_3, where

$$\frac{P_{311}}{P_{310}} = C^2_{HL} \frac{P_{311r}}{P_{310r}} . \quad (2)$$

4.2. Power Measurements

The NIST Type IV power meter must be connected to an external dc voltmeter. The substituted dc power, P_{dc}, is calculated from measured voltages using

$$P_{dc} = \frac{V^2_{off} - V^2_{on}}{R_0} , \quad (3)$$

where V_{off} is the output voltage with no rf power applied, V_{on} is the output voltage with rf applied, and R_0 (50 Ω) is the resistance of the thermistor mount. Figure 3 shows the measurement sequence for a power calculation [3]. An initial V_{off} is taken; rf power is applied and V_{on} is measured; rf power is removed and a final V_{off} is taken. The initial and final dc measurements are used with the V_{on} measurement to calculate the power and correct for any mount drift, which is assumed to be linear. The calculated value of V_{off} in Eq. (3) is given by

$$V_{off} = V_{off,i} + \frac{t_2 - t_1}{t_3 - t_1} (V_{off,f} - V_{off,i}) , \quad (4)$$

where $V_{off,i}$ is the voltage reading taken before rf is applied at time t_1, $V_{off,f}$ is the voltage taken after rf is removed at time t_3, and t_2 is the time at which V_{on} is taken.

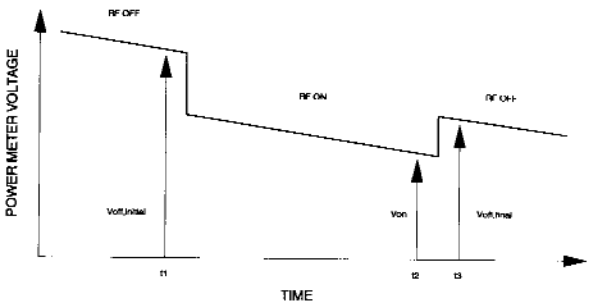

Fig. 3. Sequence for measuring power meter dc voltages.

5. Results

The calibration constant, C^2_{HL}, which is a measure of the nonlinearity of mount P_3, was obtained by repeated measurements. The average value of the three hundred trials taken so far is $C^2_{HL} = 1.00030$ or $+130$ μB. Long-term data are being accumulated to validate the calibration of P_3.

Table 1 shows a sample calibration. Powers read by the three thermistor mounts are displayed for each of the three stages. The calculated calibration constant is shown, along with the actual step in power for each leg of the system.

Table 1. Sample calibration results of the 30 MHz Linear Measurement System's standard mount

	Switches 1&2	Switch 1	Switch 2
P(1)	11.5194	11.5089	0.0000
P(2)	11.4170	0.0001	11.3991
P(3)	11.0907	2.7644	2.7756

Leg 1: 6.0335 dB
Leg 2: 6.0160 dB

C^2_{HL} : 1.00029

6. Uncertainty Analysis

6.1. Evaluation of Type A Standard Uncertainty

Evaluation of a Type A standard uncertainty may be based on any valid statistical method for treating data. Examples are calculating the standard deviation of the mean of a series of independent observations, using the method of least squares to fit a curve to data in order to estimate the parameters of the curve and their standard deviations, and carrying out an analysis of variance in order to identify and quantify random effects in certain kinds of measurements [4].

The calibration of the standard mount, P_3, has been repeated three hundred times to determine the repeatability of the system. Tests were performed at various times of the day over several days to cover as many random factors as possible, including variations of environmental conditions and the operator's ability to renull the system. The sample standard deviation of the mean is $\pm 0.000335\%$ or ± 2 μB. Long-term data are being accumulated to validate this calibration, and a control chart is being developed to track any possible outliers or drift.

6.2. Evaluation of Type B Standard Uncertainty

Evaluation of a Type B standard uncertainty is based upon scientific judgment using all of the available relevant information. This includes previous measurement data, manufacturers' specifications, data provided in calibration reports, knowledge of the behavior of relevant instruments and materials, and uncertainties assigned to reference data taken from handbooks [4].

The Type B evaluation of standard uncertainty accounts for the following factors:

a. Uncertainty in the dc voltmeter measurements.
b. Uncertainty in the Type IV power meters.
c. Imperfect isolation between the two legs.
d. Uncertainty because $P_{301} \neq P_{310}$.
e. Effects of impedance changes in P_3.
f. RF leakage.
g. Spurious signals and harmonics.

6.2.1 Voltmeter Uncertainty The uncertainty in the individual voltmeter readings may be determined by taking the total differential of the power expression, Eq. (3), which gives

$$dP = \frac{2}{R_0}\left(V_{off}\, dV_{off} - V_{on}\, dV_{on}\right) . \qquad (5)$$

The total differential of power, Eq. (5), may be determined by taking the differential of V_{off}, Eq. (4), which gives

$$dV_{off} = (1-T)dV_{off,i} + T\,dV_{off,f} , \qquad (6)$$

where

$$T = \frac{t_2 - t_1}{t_3 - t_1} . \qquad (7)$$

The uncertainties, $dV_{off,i}$, $dV_{off,f}$, and dV_{on}, in the measured values of $V_{off,i}$, $V_{off,f}$, and V_{on}, are based on the voltmeter manufacturer's specifications.

Figure 4 shows the uncertainty in the power measurement as a function of power level, assuming the powers are ratioed as they are in the C^2_{HL}

calculation, Eq. (1). The power measurements, P_{301} and P_{310}, which are approximately 3 mW, result in uncertainties of 0.036%. The other power measurements, which are approximately 12 mW, result in uncertainties of 0.008%. The uncertainty of C^2_{HL} due to the voltmeter readings may be found by inserting the individual power uncertainties into Eq. (1), which gives

$$C^2_{HL} + \Delta_v = \left[\left(\frac{\frac{P_{310}+\Delta_{310}}{P_{110}-\Delta_{110}}}{\frac{P_{311}+\Delta_{311}}{P_{111}-\Delta_{111}}} \right)^{1/2} + \left(\frac{\frac{P_{301}+\Delta_{301}}{P_{201}-\Delta_{201}}}{\frac{P_{311}+\Delta_{311}}{P_{211}-\Delta_{211}}} \right)^{1/2} \right]^2 . \quad (8)$$

This results in an uncertainty of $\Delta_V = \pm 0.028\%$ or ± 122 μB.

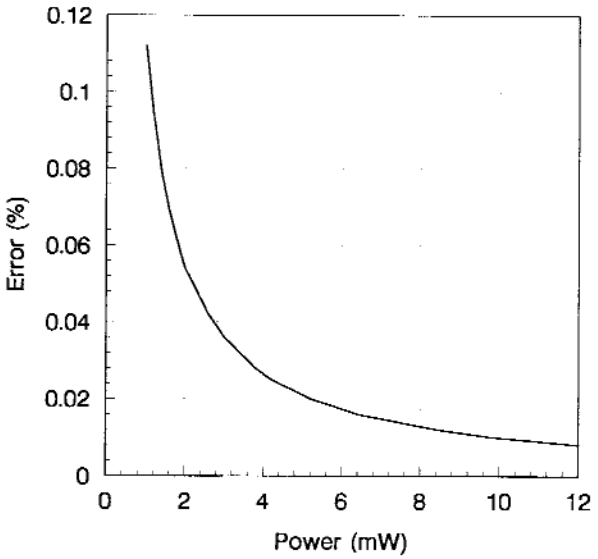

Fig. 4. Power measurement uncertainty due to DVM when ratios are taken.

6.2.2 Type IV Power-Meter Uncertainty The four possible sources of uncertainties internal to the Type IV power meter are the reference resistors, the operational amplifier open-loop gain, input offset voltage, and input bias current. Larsen has shown that the uncertainties due to the Type IV power meters are negligible compared to those of the voltmeters [2].

6.2.3 Imperfect Isolation An uncertainty in the calculation of C^2_{HL} may result if P_1 and P_2 are not zero when they are assumed to be. The thermistor mounts are square-law detectors and are not sufficiently sensitive to determine whether P_1 and P_2 are low enough in the "off" condition to avoid significant errors. This uncertainty is derived in Appendix B.

The corrected formula for C^2_{HL}, taking imperfect isolation into account, is

$$C^2_{HL} = \left[\left(\frac{\frac{P_{310r}}{P_{110r}}}{\frac{P_{311r}}{P_{111r}}} \right)^{1/2} \frac{1}{|1+\beta_1|} + \left(\frac{\frac{P_{301r}}{P_{201r}}}{\frac{P_{311r}}{P_{211r}}} \right)^{1/2} \frac{1}{|1+\gamma|} \right]^2 , \quad (9)$$

where

$$\beta_1 = -\frac{Q_{12}\Delta b_2}{b_{110}} \quad (10)$$

and

$$\gamma_1 = -\frac{\Delta b_1}{b_{201}Q_{12}} . \quad (11)$$

Here, γ_1 is the measure of P_1's contribution to C^2_{HL} if it is not zero when it is assumed to be, and β_1 is the measure of P_2's contribution to C^2_{HL} if it is not zero when it is assumed to be. The terms, b_{110} and b_{201} are the corresponding voltages to the powers P_{110} and P_{201}, respectively. Assuming P_{110} and P_{201} are 12 mW, b_{110} and b_{201} are equal to 0.7746 V. The term, Q_{12}, is defined in Appendix B and its value is approximately -1. The Δb's represent the b's which were assumed to be zero in Appendix A. If the isolation between the channels is 65 dB, as is stated in the power divider manufacturer's specifications, then $\Delta b_1 = \Delta b_2 = 0.000436$. Using nominal values for the P's and substituting the values into Eq. (9), an uncertainty of $\pm 0.112\%$ or ± 488 μB is obtained.

6.2.4 Uncertainty Because $P_{301} \neq P_{310}$ An uncertainty in the calculation of C^2_{HL} may result if $P_{301} \neq P_{310}$. The derivation of this uncertainty can be found in Appendix C.

The measure of nonlinearity, α, of thermistor mount three is

$$\alpha = \frac{1 - C^2_{HL}}{C^2_{HL}\, P_{Lr} - P_{Hr}} , \quad (12)$$

where P_{Lr} is the reading of mount three at the low level and P_{Hr} is the power reading of mount three at the high level. Assuming $C^2_{HL}=1.0004$ worst case, $P_{Lr}=3$ mW, and $P_{Hr}=12$ mW, α is calculated to be 3.334×10^{-5}. The ratio K_{301}/K_{310} is given by

$$\frac{K_{301}}{K_{310}}=\frac{1+\alpha P_{301r}}{1+\alpha P_{310r}}. \tag{13}$$

If P_{301r} is 10% greater than P_{310r}, then

$$\frac{K_{301}}{K_{310}}=\frac{1+\alpha(3\times1.10)}{1+\alpha(3)}=1.000010. \tag{14}$$

The effect of this being nonunity results in a corrected formula for C^2_{HL}, where

$$C^2_{HL}=\left[\left(\frac{\frac{P_{310r}}{P_{110r}}}{\frac{P_{311r}}{P_{111r}}}\right)^{1/2}+\left(\frac{\frac{K_{301}}{K_{310}}\frac{P_{310r}}{P_{201r}}}{\frac{P_{311r}}{P_{211r}}}\right)^{1/2}\right]^2$$

$$=1.000005 \tag{15}$$

using nominal values for the P's. The result is an uncertainty of $\pm0.0005\%$ or ±3 μB.

6.2.5 Uncertainty Due to Impedance Changes in P_3 An uncertainty in the calculation of C^2_{HL} may result if the impedance changes in P_3 with power level. The derivation of this uncertainty can be found in Appendix D.

The corrected formula for C^2_{HL}, taking impedance changes in P_3 into account, is

$$C^2_{HL}=\frac{\left[\left(\frac{\frac{P_{310r}}{P_{110r}}}{\frac{P_{311r}}{P_{111r}}}\right)^{1/2}+\left(\frac{\frac{P_{301r}}{P_{201r}}}{\frac{P_{311r}}{P_{211r}}}\right)^{1/2}\right]^2}{\left|\frac{1-\Gamma_{LMS}\,\Gamma_{311}}{1-\Gamma_{LMS}\,\Gamma_{310}}\right|^2\frac{(1-|\Gamma_{310}|^2)}{(1-|\Gamma_{311}|^2)}}, \tag{16}$$

where Γ_{311} is the reflection coefficient of mount three at the high level, Γ_{310} is the reflection coefficient of mount three at the low level, and Γ_{LMS} is the reflection coefficient of the system looking into port three.

The measured value of Γ_{310} was actually taken 10 dB below Γ_{310} instead of the 6 dB step, so the uncertainty should be conservative. Using nominal values for the P's and the measured reflection coefficients, the calculated uncertainty is $\pm0.014\%$ or ±62 μB.

Impedance changes in the diode detector with respect to power level are assumed to have a negligible effect on the overall uncertainty.

6.2.6 Uncertainty Due to RF Leakage It is difficult to assign a quantitative uncertainty due to rf leakage. In order to reduce leakage, all coaxial cables in the system were replaced with semirigid lines and, wherever possible, SMA connectors were used. For now, the uncertainty due to rf leakage is assumed to be ±10 μB or $\pm0.0023\%$.

6.2.7 Uncertainty Due to Spurious Signals and Harmonics After the signal is amplified and filtered, any harmonics are at least -92 dBc, while spurious signals are no greater than -84 dBc. This will result in a measurement error that will affect the uncertainty of C^2_{HL}.

From Eq. (3), the calculated dc power is

$$P_{dc}=20\,(V^2_{off}-V^2_{on}), \tag{17}$$

where P_{dc} is in mW. Assuming $V_{off}=1$ V, then $V_{on}=0.63246$ V for a calculated power of 12 mW and $V_{on}=0.92195$ V for a calculated power of 3 mW.

A harmonic at -92 dBc results in an uncertainty of $\pm0.0025\%$ for a voltage measurement. This uncertainty translates to power uncertainties of (12 ± 0.0004) mW and (3 ± 0.0008) mW. Using the nominal powers to calculate C^2_{HL}, an uncertainty of $\pm0.023\%$ or ±100 μB is obtained.

A spurious signal at -112 dBc results in an uncertainty of $\pm0.00025\%$ for a voltage measurement. This uncertainty translates to power uncertainties of (12 ± 0.00004) mW and (3 ± 0.000085) mW. Using the nominal powers to calculate C^2_{HL}, an uncertainty of $\pm0.0025\%$ or ±11 μB is obtained.

6.2.8. Overall Type B Uncertainty For each Type B component, an estimated range, $\pm a_j$, is given, assuming that the quantity in question has a 100% probability of lying within that interval. The quantity is treated as if it is equally probable for its value to lie anywhere within the interval. Therefore, it is modeled by a rectangular probability distribution. The best estimate of the standard deviation, u_j, is

$$u_j=\frac{a_j}{\sqrt{3}}. \tag{18}$$

Table 2 shows all of the Type B components along with their corresponding uncertainties and standard deviations. The overall standard deviation of the Type B components, calculated using the root-sum-of-squares method (RSS), is $\pm0.069\%$ or ±299 μB.

Table 2. Type B components of the 30 MHz Linear Measurement System with corresponding uncertainty ranges and standard deviations

Component	Range (%)	Standard deviation (%)
dc voltage measurements	±0.028	0.016
Imperfect isolation	±0.112	0.065
$P_{301} \neq P_{310}$	±0.0005	0.0003
Impedance changes in P_3	±0.014	0.008
rf leakage	±0.0023	0.0013
Spurious signals	±0.0025	0.0014
Harmonics	±0.023	0.013
Combined Type B Standard Uncertainty (RSS)		± 0.069 (±299 μB)

6.3 Combined Standard Uncertainty

The combined standard uncertainty, u_c, is taken to represent the estimated standard deviation of the result. It is obtained by combining the individual standard deviations, u_i, whether arising from a Type A or a Type B evaluation [4]. The technique used to combine the standard deviations is the RSS method.

The total uncertainty reported is the expanded uncertainty, U, which is obtained by multiplying u_c by a coverage factor, k. To be consistent with current international practice, the value of k used at NIST for calculating U is $k = 2$. The total expanded uncertainty, U, of the mount's nonlinearity is calculated to be ±0.138% or ±598 μB.

7. Conclusion

The first step toward offering a calibration service at NIST to support rf attenuators and voltage doublers that operate at 30 MHz has been completed. The reference standard, a tuned single-element thermistor mount, has been calibrated using an LMS, designed and constructed at NIST. The next step is to modify the LMS so that a device under test may be inserted into the system and calibrated against the reference standard.

8. Appendix A. Scattering Coefficient Analysis of the LMS

The 30 MHz Linear Measurement System can be considered a five port network, as shown in Fig. 5. The analysis assumes that the LMS is an ideal system—that is, the system is linear, and when b_1 and b_2 are assumed to be 0, they truly are.

The pertinent scattering coefficients are

$$\begin{aligned} b_1 &= S_{11}a_1 + S_{12}a_2 + S_{13}a_3 + S_{14}a_4 + S_{15}a_5 \\ b_2 &= S_{21}a_1 + S_{22}a_2 + S_{23}a_3 + S_{24}a_4 + S_{25}a_5 \\ b_3 &= S_{31}a_1 + S_{32}a_2 + S_{33}a_3 + S_{34}a_4 + S_{35}a_5 \\ b_4 &= S_{41}a_1 + S_{42}a_2 + S_{43}a_3 + S_{44}a_4 + S_{45}a_5 \\ b_5 &= S_{51}a_1 + S_{52}a_2 + S_{53}a_3 + S_{54}a_4 + S_{55}a_5 . \end{aligned} \quad (19)$$

If $a_1 = \Gamma_1 b_1$ and $a_2 = \Gamma_2 b_2$, then Eq. (19) may be written as

$$\begin{aligned} b_1(1-\Gamma_1 S_{11}) &= S_{12}\Gamma_2 b_2 + S_{13}a_3 + S_{14}a_4 + S_{15}a_5 \\ b_2(1-\Gamma_2 S_{22}) &= S_{21}\Gamma_1 b_1 + S_{23}a_3 + S_{24}a_4 + S_{25}a_5 \\ b_3 &= S_{31}\Gamma_1 b_1 + S_{32}\Gamma_2 b_2 + S_{33}a_3 + S_{34}a_4 + S_{35}a_5 \\ b_4 &= S_{41}\Gamma_1 b_1 + S_{42}\Gamma_2 b_2 + S_{43}a_3 + S_{44}a_4 + S_{45}a_5 \\ b_5 &= S_{51}\Gamma_1 b_1 + S_{52}\Gamma_2 b_2 + S_{53}a_3 + S_{54}a_4 + S_{55}a_5 \end{aligned} \quad (20)$$

This gives five equations and eight unknown variables—a_3, a_4, a_5, b_1, b_2, b_3, b_4, and b_5. Four variables can be eliminated from Eq. (20), say a_4, b_4, a_5, and b_5. Eq. (20) becomes

$$b_1 = P'_{13}a_3 + Q'_{12}b_2 + Q'_{13}b_3 , \quad (21)$$

where the primed quantities are functions of the scattering coefficients and Γ_1 and Γ_2.

It is assumed that Γ_3 is constant with respect to varying power levels. If now $a_3 = \Gamma_3 b_3$,

$$\begin{aligned} b_1 &= (P'_{13}\,\Gamma_3 + Q'_{13})b_3 + Q'_{12}b_2 \equiv \\ &\quad Q_{13}b_3 + Q_{12}b_2 \end{aligned} \quad (22)$$

or

$$b_3 = \frac{b_1 - Q_{12}b_2}{Q_{13}} , \quad (23)$$

where two complex constants, Q_{12} and Q_{13}, describe the relationship among b_1, b_2, and b_3.

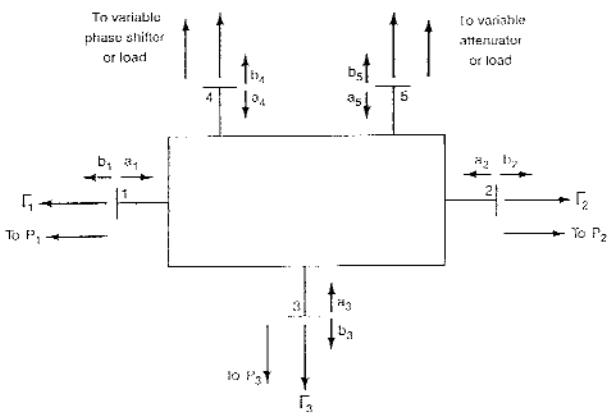

Fig. 5. LMS port nomenclature.

Equation (23) may be applied under three conditions: subscript "10" when $b_2=0$; "01" when $b_1=0$; and "11" when neither b_1 nor b_2 equal 0. Thus

$$b_{311}=\frac{b_{111}-Q_{12}b_{211}}{Q_{13}}, \tag{24}$$

where b_{311} is the value of b_3 when b_1 and b_2 are both energized from ports four and five. When $b_2=0$, which occurs by energizing port four and terminating port five, Eq. (23) becomes

$$b_{310}=\frac{b_{110}}{Q_{13}} \tag{25}$$

or

$$Q_{13}=\frac{b_{110}}{b_{310}}. \tag{26}$$

Similarly, when $b_1=0$, which occurs by energizing port five and terminating port four, Eq. (23) becomes

$$b_{301}=\frac{-Q_{12}}{Q_{13}}\,b_{201}. \tag{27}$$

Substituting Eq. (26) into Eq. (27) gives

$$b_{301}=-Q_{12}b_{201}\frac{b_{310}}{b_{110}} \tag{28}$$

or

$$-Q_{12}=\frac{b_{301}}{b_{201}}\frac{b_{110}}{b_{310}}. \tag{29}$$

Substituting Eqs. (26) and (29) into Eq. (24) gives

$$1=\frac{b_{111}}{b_{311}}\frac{b_{310}}{b_{110}}+\frac{b_{211}}{b_{311}}\frac{b_{301}}{b_{201}}. \tag{30}$$

The b's are complex numbers. If the phase is measured relative to b_{111}/b_{311}, then

$$1=\frac{b_{111}}{b_{311}}\left|\frac{b_{310}}{b_{110}}\right|e^{j\theta_{3110}}+\left|\frac{b_{211}}{b_{311}}\right|e^{j\theta_{2311}}\left|\frac{b_{301}}{b_{201}}\right|e^{j\theta_{3201}}. \tag{31}$$

If $\theta=\theta_{2311}+\theta_{3201}-\theta_{3110}$, Eq. (31) becomes

$$1=e^{j\theta_{3110}}\left[\frac{b_{111}}{b_{311}}\left|\frac{b_{310}}{b_{110}}\right|+\left|\frac{b_{211}}{b_{311}}\right|\left|\frac{b_{301}}{b_{201}}\right|e^{j\theta}\right]. \tag{32}$$

Since the detectors measure only magnitudes, the magnitude squared of Eq. (32) is

$$1=\left(\left|\frac{\frac{b_{310}}{b_{110}}}{\frac{b_{311}}{b_{111}}}\right|+\left|\frac{\frac{b_{301}}{b_{201}}}{\frac{b_{311}}{b_{211}}}\right|\cos\theta\right)^2+\left|\frac{\frac{b_{301}}{b_{201}}}{\frac{b_{311}}{b_{211}}}\right|^2\sin^2\theta, \tag{33}$$

which can also be written as

$$1=\left|\frac{\frac{b_{310}}{b_{110}}}{\frac{b_{311}}{b_{111}}}\right|^2+\left|\frac{\frac{b_{301}}{b_{201}}}{\frac{b_{311}}{b_{211}}}\right|^2+2\left|\frac{\frac{b_{310}}{b_{110}}}{\frac{b_{311}}{b_{111}}}\right|\left|\frac{\frac{b_{301}}{b_{201}}}{\frac{b_{311}}{b_{211}}}\right|\cos\theta. \tag{34}$$

Since the powers are proportional to the squares of the voltages, Eq. (34) becomes

$$1=\frac{\frac{P_{310}}{P_{110}}}{\frac{P_{311}}{P_{111}}}+\frac{\frac{P_{301}}{P_{201}}}{\frac{P_{311}}{P_{211}}}+2\sqrt{\frac{\frac{P_{310}}{P_{110}}}{\frac{P_{311}}{P_{111}}}\frac{\frac{P_{301}}{P_{201}}}{\frac{P_{311}}{P_{211}}}}\cos\theta. \tag{35}$$

Completing the square and transposing terms gives

$$\left[\left(\frac{\frac{P_{310}}{P_{110}}}{\frac{P_{311}}{P_{111}}}\right)^{1/2}+\left(\frac{\frac{P_{301}}{P_{201}}}{\frac{P_{311}}{P_{211}}}\right)^{1/2}\right]^2=1+2\sqrt{\frac{\frac{P_{310}}{P_{110}}}{\frac{P_{311}}{P_{111}}}\frac{\frac{P_{301}}{P_{201}}}{\frac{P_{301}}{P_{211}}}}(1-\cos\theta). \tag{36}$$

Since the powers are all positive and $(1-\cos\theta)$ is greater than or equal to 0, the quantity on the left side of Eq. (36) is a minimum when a null is obtained ($\theta=0$). Since $\cos\theta$ approaches 1 as θ approaches 0, Eq. (36) becomes

$$1=\left[\left(\frac{\frac{P_{310}}{P_{110}}}{\frac{P_{311}}{P_{111}}}\right)^{1/2}+\left(\frac{\frac{P_{301}}{P_{201}}}{\frac{P_{311}}{P_{211}}}\right)^{1/2}\right]^2. \quad (37)$$

The above P's are the true powers. The detectors, however, give readings proportional to the true values. Furthermore, P_3 could have a different proportionality constant for the two levels if the detector is nonlinear. The ratio of these two proportionality constants is the desired result.

If the subscript "r" represents proportional readings, and the nonsubscripted P's represent the true values, then

$$\begin{aligned} P_1&=K_1 P_{1r}\\ P_2&=K_2 P_{2r}\\ P_{311}&=K_{311} P_{311r}\\ P_{310}&=K_{310} P_{310r}\\ P_{301}&=K_{301} P_{301r} \end{aligned} \quad (38)$$

The powers, P_{310} and P_{301}, will ordinarily be very close, and essentially

$$K_{310}=K_{301} \quad (39)$$

since the detectors are assumed to be very nearly linear. P_1 and P_2 remain essentially constant. Substituting Eqs. (38) and (39) into Eq. (37) gives

$$1=\left(\left(\frac{K_{310}}{K_{311}}\right)^{1/2}\left[\left(\frac{\frac{P_{310r}}{P_{110r}}}{\frac{P_{311r}}{P_{111r}}}\right)^{1/2}+\left(\frac{\frac{P_{301r}}{P_{201r}}}{\frac{P_{311r}}{P_{211r}}}\right)^{1/2}\right]\right)^2 \quad (40)$$

or

$$C_{HL}^2=\frac{K_{311}}{K_{310}}=\left[\left(\frac{\frac{P_{310r}}{P_{110r}}}{\frac{P_{311r}}{P_{111r}}}\right)^{1/2}+\left(\frac{\frac{P_{301r}}{P_{201r}}}{\frac{P_{311r}}{P_{211r}}}\right)^{1/2}\right]^2, \quad (41)$$

where C_{HL}^2 is the calibration constant that one must multiply the P_{311r}/P_{310r} reading by to get the true ratio

$$\frac{P_{311}}{P_{311}}=C_{HL}^2\frac{P_{311r}}{P_{310r}}. \quad (42)$$

The calibration constant should be used only when P_3 is operating at the two levels for which it was calibrated.

9. Appendix B. Imperfect Isolation

It is desirable to have an estimate of the error when P_1 and P_2 are not 0 when they are assumed to be. The detectors are square-law detectors and are not sufficiently sensitive to determine whether P_1 and P_2 are low enough in the "off" condition to avoid significant errors.

Let Δb's represent the b's which were assumed to be 0 in Appendix A. Equation (24) is still valid, but Eq. (25) should now be

$$b_{310}=\frac{b_{110}-Q_{12}\Delta b_2}{Q_{13}}=\frac{b_{110}}{Q_{13}}\left(1-\frac{Q_{12}\,\Delta b_2}{b_{110}}\right) \quad (43)$$

and Eq. (27) should now be

$$b_{301}=\frac{\Delta b_1-Q_{12}\,b_{201}}{Q_{13}}=-\frac{Q_{12}b_{201}}{Q_{13}}\left(1-\frac{\Delta b_1}{b_{201}\,Q_{12}}\right). \quad (44)$$

Let

$$\beta_1=-\frac{Q_{12}\,\Delta b_2}{b_{110}} \quad (45)$$

and

$$\gamma_1=-\frac{\Delta b_1}{b_{201}Q_{12}}. \quad (46)$$

Combining Eqs. (43)–(46) gives

$$Q_{13}=\frac{b_{110}}{b_{310}}(1+\beta_1) \quad (47)$$

and

$$-Q_{12}=\frac{b_{301}}{b_{201}}\frac{b_{110}}{b_{310}}\frac{1+\beta_1}{1+\gamma_1}. \quad (48)$$

Eq. (24) now becomes

$$1=\frac{\frac{b_{111}}{b_{311}}+\frac{b_{211}}{b_{311}}\frac{b_{301}}{b_{201}}\frac{b_{110}}{b_{310}}\frac{1+\beta_1}{1+\gamma_1}}{\frac{b_{110}}{b_{310}}(1+\beta_1)} \quad (49)$$

or

$$1=\frac{b_{111}}{b_{311}}\frac{b_{310}}{b_{110}}\frac{1}{1+\beta_1}+\frac{b_{211}}{b_{311}}\frac{b_{301}}{b_{201}}\frac{1}{1+\gamma_1}. \quad (50)$$

The b's and β_1 and γ_1 are complex numbers. If the phase is measured relative to b_{111}/b_{311}, then

$$1=\frac{b_{111}}{b_{311}}\left|\frac{b_{310}}{b_{110}}\right|\frac{e^{j(\theta_{3110}-\theta_{\beta 1})}}{|1+\beta_1|}+\left|\frac{b_{211}}{b_{311}}\right|e^{j\theta_{2311}}$$

$$\left|\frac{b_{301}}{b_{201}}\right|\frac{e^{j(\theta_{3201}-\theta_{\gamma 1})}}{|1+\gamma_1|}, \quad (51)$$

where

$$\theta_{\beta 1}=Arg\ (1+\beta_1) \quad (52)$$

and

$$\theta_{\gamma 1}=Arg\ (1+\gamma_1). \quad (53)$$

Equation (51) may also be written as

$$1=e^{j(\theta_{3110}-\theta_{\beta 1})}\left[\frac{\left|\frac{b_{310}}{b_{110}}\right|}{\frac{b_{311}}{b_{111}}|1+\beta_1|}+\frac{\left|\frac{b_{301}}{b_{201}}\right|e^{j(\theta+\theta_{\beta 1}-\theta_{\gamma 1})}}{\left|\frac{b_{311}}{b_{211}}\right||1+\gamma_1|}\right], \quad (54)$$

where

$$\theta=\theta_{2311}+\theta_{3201}-\theta_{3110}. \quad (55)$$

As in Appendix A, taking the square of the magnitude and changing to power gives

$$1=\frac{\frac{P_{310}}{P_{110}}}{\frac{P_{311}}{P_{111}}|1+\beta_1|^2}+\frac{\frac{P_{301}}{P_{201}}}{\frac{P_{311}}{P_{211}}|1+\gamma_1|^2}+P_{sq}\cos(\theta+\theta_{\beta_1}-\theta_{\gamma_1}), \quad (56)$$

where

$$P_{sq}=2\sqrt{\frac{\frac{P_{310}}{P_{110}}\frac{P_{301}}{P_{201}}}{\frac{P_{311}}{P_{111}}\frac{P_{311}}{P_{211}}|1+\beta_1|^2\,|1+\gamma_1|^2}}. \quad (57)$$

Completing the square of Eq. (56) and transposing terms gives

$$\left[\left(\frac{\frac{P_{310}}{P_{110}}}{\frac{P_{311}}{P_{111}}}\right)^{1/2}\frac{1}{|1+\beta_1|}+\left(\frac{\frac{P_{301}}{P_{201}}}{\frac{P_{311}}{P_{211}}}\right)^{1/2}\frac{1}{|1+\gamma_1|}\right]^2=$$

$$1+P_{sq}\,[1-\cos(\theta+\theta_{\beta_1}-\theta_{\gamma_1})]. \quad (58)$$

As in Appendix A, using the argument on the function being minimum when the angle is 0, and substituting in the proportional readings

$$C_{HL}^2=\left[\left(\frac{\frac{P_{310r}}{P_{110r}}}{\frac{P_{311r}}{P_{111r}}}\right)^{1/2}\frac{1}{|1+\beta_1|}+\left(\frac{\frac{P_{301r}}{P_{201r}}}{\frac{P_{311r}}{P_{211r}}}\right)^{1/2}\frac{1}{|1+\gamma_1|}\right]^2. \quad (59)$$

10. Appendix C. Error Due to $P_{301}\neq P_{310}$

Since the detectors are very close to being precisely linear, it is reasonable to model the nonlinearity by

$$P=KP_r\,(1+\alpha P_r),$$

where α is a measure of the nonlinearity. The non-subscripted P is the true value and P_r is the proportional reading. Substituting Eq. (60) into Eq. (42)

$$\frac{P_H}{P_L}=C_{HL}^2\frac{P_{Hr}}{P_{Lr}}=\frac{KP_{Hr}\,(1+\alpha P_{Hr})}{KP_{Lr}\,(1+\alpha P_{Lr})} \quad (61)$$

or

$$C_{HL}^2=\frac{1+\alpha P_{Hr}}{1+\alpha P_{Lr}}. \quad (62)$$

Solving for α

$$\alpha=\frac{1-C_{HL}^2}{C_{HL}^2\,P_{Lr}-P_{Hr}} \quad (63)$$

The ratio K_{301}/K_{310} may be found using Eq. (60)

$$\frac{P_{301}}{P_{310}}=\frac{K_{301}P_{301r}}{K_{310}P_{301r}}=\frac{KP_{301r}\,(1+\alpha P_{301r})}{KP_{310r}\,(1+\alpha P_{310r})} \quad (64)$$

or

$$\frac{K_{301}}{K_{310}} = \frac{1+\alpha P_{301r}}{1+\alpha P_{310r}} \quad . \tag{65}$$

The effect of this non-unity is obtained by substituting Eq. (38) and (65) into Eq. (37), which gives

$$1 = \left(\left(\frac{K_{310}}{K_{311}}\right)^{1/2} \left[\left(\frac{\frac{P_{310r}}{P_{110r}}}{\frac{P_{311r}}{P_{111r}}} \right)^{1/2} + \left(\frac{\frac{K_{301}}{K_{310}} \frac{P_{301r}}{P_{201r}}}{\frac{P_{311r}}{P_{211r}}} \right)^{1/2} \right] \right)^2 \tag{66}$$

or

$$C_{\mathrm{HL}}^2 = \frac{K_{311}}{K_{310}} = \left[\left(\frac{\frac{P_{310r}}{P_{110r}}}{\frac{P_{311r}}{P_{111r}}} \right)^{1/2} + \left(\frac{\frac{K_{301}}{K_{310}} \frac{P_{301r}}{P_{201r}}}{\frac{P_{311r}}{P_{211r}}} \right)^{1/2} \right]^2 . \tag{67}$$

11. Appendix D. Effects of Impedance Changes in P_3

Starting with Eq. (21),

$$b_1 = P'_{13} a_3 + Q'_{12}\, b_2 + Q'_{13} b_3. \tag{68}$$

If ports four and five are terminated in impedances that null the hybrid, b_1 and b_2 are almost 0 even when a_3 is energized since the two legs of each power divider are isolated. Thus

$$\Gamma_{\mathrm{LMS}} = \frac{b_3}{a_3} \approx - \frac{P'_{13}}{Q'_{13}} , \tag{69}$$

where Γ_{LMS} is the reflection coefficient looking into port three when ports four and five are terminated with matching impedances. The second part of Eq. (69) is obtained from setting b_1 and b_2 to 0 in Eq. (68).

Substituting Eq. (69) into Eq. (68), and using $a_3 = \Gamma_3\, b_3$ yields

$$b_1 = Q'_{12}\, b_2 + (-\Gamma_{\mathrm{LMS}}\, Q'_{13}\, \Gamma_3 + Q'_{13})\, b_3 \tag{70}$$

or

$$b_3(1 - \Gamma_{\mathrm{LMS}}\, \Gamma_3) = \frac{b_1}{Q'_{13}} - \frac{b_2 Q'_{12}}{Q'_{13}} \quad . \tag{71}$$

As before, making b_1 and b_2 successively 0, gives

$$Q'_{13} = \frac{b_{110}}{b_{310}} \frac{1}{1 - \Gamma_{\mathrm{LMS}} \Gamma_{310}} . \tag{72}$$

and

$$-\frac{Q'_{12}}{Q'_{13}} = \frac{b_{301}}{b_{201}} (1 - \Gamma_{\mathrm{LMS}}\, \Gamma_{301}). \tag{73}$$

Assuming $\Gamma_{310} = \Gamma_{301}$, since $b_{310} \approx b_{301}$, gives

$$-\frac{Q'_{12}}{Q'_{13}} = \frac{b_{301}}{b_{201}} (1 - \Gamma_{\mathrm{LMS}}\, \Gamma_{310}). \tag{74}$$

Substituting Eqs. (72) and (74) into Eq. (71), and rearranging terms, gives

$$\frac{1 - \Gamma_{\mathrm{LMS}}\, \Gamma_{311}}{1 - \Gamma_{\mathrm{LMS}}\, \Gamma_{310}} = \frac{b_{111}}{b_{311}} \frac{b_{310}}{b_{110}} + \frac{b_{211}}{b_{311}} \frac{b_{301}}{b_{201}} . \tag{75}$$

Since the right side of Eq. (75) is identical to the right side of Eq. (30), the same manipulations may be performed to yield

$$\left| \frac{1 - \Gamma_{\mathrm{LMS}}\, \Gamma_{311}}{1 - \Gamma_{\mathrm{LMS}}\, \Gamma_{310}} \right|^2 = \left(\left| \frac{\frac{b_{310}}{b_{110}}}{\frac{b_{311}}{b_{111}}} \right| + \left| \frac{\frac{b_{301}}{b_{201}}}{\frac{b_{311}}{b_{211}}} \right| \right)^2 + 2 \left| \frac{\frac{b_{310}}{b_{110}}}{\frac{b_{311}}{b_{111}}} \right| \left| \frac{\frac{b_{301}}{b_{201}}}{\frac{b_{311}}{b_{211}}} \right| (\cos\theta - 1) . \tag{76}$$

As before, the powers are proportional to the b^2's except for P_3, because of the change in Γ_3. Thus

$$P_{311} = \frac{|b_{311}|^2}{Z_0} (1 - |\Gamma_{311}|^2) , \tag{77}$$

$$P_{310} = \frac{|b_{310}|^2}{Z_0} (1 - |\Gamma_{310}|^2) , \tag{78}$$

and

$$P_{301}=\frac{|b_{301}|^2}{Z_0}(1-|\Gamma_{301}|^2)$$

$$=\frac{|b_{301}|^2}{Z_0}(1-|\Gamma_{310}|^2), \qquad (79)$$

because $\Gamma_{301}=\Gamma_{310}$ has been assumed. The characteristic impedance is denoted by Z_0. Replacing the voltages with powers, gives

$$\left|\frac{1-\Gamma_{LMS}\,\Gamma_{311}}{1-\Gamma_{LMS}\,\Gamma_{310}}\right|^2\frac{(1-|\Gamma_{310}|^2)}{(1-|\Gamma_{311}|^2)}=$$

$$\left[\left(\frac{\frac{P_{310}}{P_{110}}}{\frac{P_{311}}{P_{111}}}\right)^{1/2}+\left(\frac{\frac{P_{301}}{P_{201}}}{\frac{P_{311}}{P_{211}}}\right)^{1/2}\right]^2+$$

$$P_{sq}(1-\cos\theta), \qquad (80)$$

where

$$P_{sq}=2\sqrt{\frac{\frac{P_{310}}{P_{110}}\,\frac{P_{301}}{P_{201}}}{\frac{P_{311}}{P_{111}}\,\frac{P_{311}}{P_{211}}}}\,. \qquad (81)$$

As in Appendix A, using the argument that the function is minimum when the angle is 0, and substituting in the proportional readings

$$C_{HL}^2\left|\frac{1-\Gamma_{LMS}\,\Gamma_{311}}{1-\Gamma_{LMS}\,\Gamma_{310}}\right|^2\frac{(1-|\Gamma_{310}|^2)}{(1-|\Gamma_{311}|^2)}=$$

$$\left[\left(\frac{\frac{P_{310}}{P_{110}}}{\frac{P_{311}}{P_{111}}}\right)^{1/2}+\left(\frac{\frac{P_{301}}{P_{201}}}{\frac{P_{311}}{P_{211}}}\right)^{1/2}\right]^2. \qquad (82)$$

Acknowledgments

The authors acknowledge the contributions of C. Allred, who originally developed the theoretical analysis of the linear measurement system; F. Marler, who designed the 30 MHz LMS prototype; J. Juroshek and P. Leyva for reviewing this paper; P. Voris and K. Talley who helped assemble the LMS; G. Rebuldela for his advice throughout the project; and N. Larsen for supplying the data found in Fig. 4.

12. References

[1] R. A. Ginley and C. M. Allred, 1.25 MHz Attenuation Measurement System, IEEE Trans. Instrum. Meas. **IM-35**, 463-466 (1986).

[2] N. T. Larsen, A New Self-Balancing DC-Substitution RF Power Meter, IEEE Trans. Instrum. Meas. **IM-25**, 343-347 (1976).

[3] F. R. Clague, Power Measurement System for 1 mW at 1 GHz, Natl. Inst. Stand. Technol., Technical Note 1345 (1990).

[4] Taylor, B. N. and Kuyatt C. E., Guidelines for Evaluating and Expressing the Uncertainty of NIST Measurement Results, Natl. Inst. Stand. Technol., Technical Note 1297 (1993).

About the authors: *Jeffrey A. Jargon is an electrical engineer and a member of the NIST Microwave Metrology Group, where his main responsibilities are in cw, coaxial high power and 30 MHz attenuation measurements. Ronald A. Ginley is an electrical engineer in the Microwave Metrology Group. His responsibilities include the design of dual six-port systems, and software, hardware, and technical support for the 1.25 MHz Attenuation Measurement System and the lower frequency six-port systems. Douglas D. Sutton was a physical science technician in the Microwave Technology Group when this work was done. The National Institute of Standards and Technology is an agency of the Technology Administration, U.S. Department of Commerce.*

Volume 99, Number 1, January–February 1994
Journal of Research of the National Institute of Standards and Technology

[J. Res. Natl. Inst. Stand. Technol. 99, 31 (1994)]

Uncertainties in Dimensional Measurements Made at Nonstandard Temperatures

Volume 99 Number 1 January–February 1994

Dennis A. Swyt

National Institute of Standards and Technology,
Gaithersburg, MD 20899-0001

This report examines the effects of uncertainties in temperature and coefficient of thermal expansion on the expanded uncertainty of length dimensional measurements made away from the international standard reference temperature of 20 °C for artifact standards and workpieces of various materials. Specific cases examined deal with: 1) uncertainties of thermal-expansion coefficients associated with values given in engineering references, standard reference data, standard reference materials and direct measurements; and 2) uncertainties of part temperature measurements associated with realizing the International Temperature Scale of 1990 (ITS-90) and determining part temperatures relative to ITS-90 with the principal types of thermometry and achievable levels of temperature control.

Key words: dimensional measurement; dimensional tolerances; length metrology; measurement uncertainty; reference temperature; thermal expansion.

Accepted: November 1, 1993

1. Introduction

Material objects—whether complex-geometry parts designed to fit into assemblies or simple-geometry artifacts designed to be calibrated as standards of length—have dimensions which vary with temperature. The size of the variation depends upon the specific material. For example, for aluminum, steel, and silicon, typical coefficients of thermal expansion are respectively, in units of parts per million per degree Celsius, 23.1 ppm/°C, 11.5 ppm/°C, and 2.6 ppm/°C.

Because of the effects of thermal expansion, by national and international agreements length-based dimensions—including those specified, for example, on engineering drawings—are defined to be those which exist at a standard reference temperature of 20 °C [1,2].

Figure 1 illustrates one of two recent developments which have made the issue of thermal-expansion effects in part metrology a matter of increased concern. The figure shows the on-going trend in the manufacture of discrete-part products to increasingly tighter dimensional tolerances in state-of-the-art manufactured goods from aircraft and automobiles to computers and electronics [3]. According to this trend, such tolerances have been decreasing in size by a factor of approximately three every ten years, so that there are today, for example, automobile pistons with tolerances of 6 μm–7 μm and quantum-well electronic devices with tolerances of 0.5 nm [4].

The second development is a proposal to the International Organization for Standardization, subsequently unadopted but of technical import, to change the international standard reference temperature for dimensional measurements from 20 °C to 23 °C [5]. Since referring measurements to a

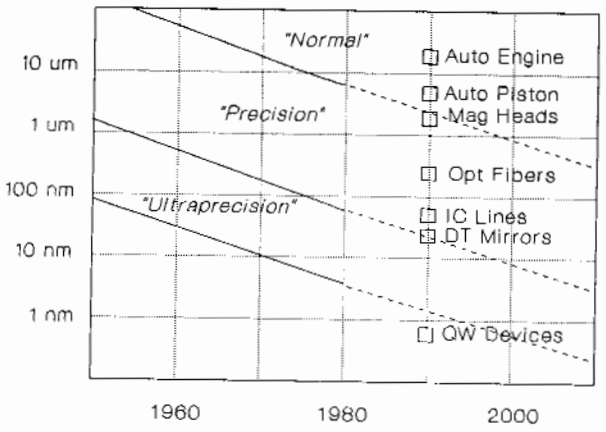

Fig. 1. Trends and examples of state-of-art in dimension tolernces of manufactured parts in normal, precision, and ultrprecision regimes.

standard temperature serves to reduce actual variations in dimensions of parts due to thermal-expansion effects as well as uncertainty in measurements, a shift in reference temperature can increase each, that is, both variations and uncertainties.

This paper looks at possible errors and likely uncertainties in dimensional measurements due to thermal-expansion effects where those measurements are made away from the reference temperature, either the specific interval of 3 °C due to a change to the proposed 23 °C or an arbitrary interval due, for example, to the settling of a temperature control system at other than the standard reference temperature.

2. Uncertainties Due to Thermal Expansion

Contributions to uncertainty in measurements of length-based dimensions due to measurements made at nonstandard temperatures are a function of the length of the object being measured, its temperature, its coefficient of thermal expansion, and the uncertainties in each of these quantities.

The coefficient of linear thermal expansion (CTE) of a material, α, is defined to be

$$\alpha(T)=\frac{\mathrm{d}L/L}{\mathrm{d}T}, \tag{1}$$

where $\mathrm{d}L/L$ is the fractional change in a characteristic linear dimension and $\mathrm{d}T$ is the change in temperature. For a sample with length L_0 at temperature T_0, the length L at temperature T is found by integration to be

$$L=L_0 \exp\left[\int_{T_0}^{T}\alpha(T)\mathrm{d}T\right]. \tag{2}$$

If $\alpha(T)$ is assumed to vary only slightly over the temperature range $T-T_0$, it may be replaced by an average value α and Eq. (2) becomes

$$L=L_0 \exp\left[\alpha(T-T_0)\right]. \tag{3}$$

For typical materials and for changes of temperatures from room temperature to their melting points, Eq. (3) is approximated to within less than 1% by

$$L=L_0\left[1+\alpha(T-T_0)\right]. \tag{4}$$

Equation (4) is the standard expression used to correct dimensional measurements made at a uniform temperature other than the one desired.

3. Uncertainties and Error Relative to Tolerances

This report will use two different methods for examining the effects of thermal expansion relative to tolerances of measurements made at nonstandard temperatures. The first method follows the recommended practice of an international standards body and deals with propagated uncertainties. The second method follows the recommended practice of a national standards body and deals with estimated maximum error. Each method compares resulting uncertainties to a tolerance, that is, to a specified limit of permissible error.

3.1 Thermal Uncertainty Index (TUI)

The first method—which is based upon the approach recommended by the International Committee for Weights and Measures (CIPM), which is the basis of a guideline published by the International Organization for Standardization, and which has been adopted as NIST policy—uses root-sum-of-squares (RSS) propagation of uncertainty [6]. In this approach, the combined standard uncertainty associated with the correction for thermal expansion given by Eq. (4) is the positive square root of the estimated variance u_c^2 given by

$$u_c=\sqrt{\left(\frac{\partial L}{\partial T}\right)^2 u_T^2+\left(\frac{\partial L}{\partial \alpha}\right)^2 u_\alpha^2}, \tag{5}$$

where there is assumed to be no correlation between the variations in temperature and the varia-

tions in the coefficients of thermal expansion. Following the CIPM approach, in this first method results are expressed as an expanded uncertainty:

$$U = k \cdot u_c, \tag{6}$$

with U determined from a coverage factor k *and* the combined standard uncertainty u_c, the estimated standard deviation given by Eq. (6). To be consistent with current international practice, the value of k used by NIST for calculating U is, by convention, $k = 2$ [7]. Hence, with partial derivatives from Eq. (4), substitution of Eq. (5), and $u_{T_0} = 0$, Eq. (6) becomes

$$U = 2 \cdot u_c = 2\sqrt{(\alpha L_0 u_T)^2 + (u_\alpha L_0 (T - T_0))^2}. \tag{7}$$

In parallel with the method to be described in the next section, this paper defines a ratio of expanded uncertainty to tolerance, that is, the limit of permissible error, called the Thermal Uncertainty Index (*TUI*):

$$TUI = (U/\mathcal{T}) \times 100\%, \tag{8}$$

where U is the expanded uncertainty defined by Eq. (7) and $\mathcal{T}$ is an engineering tolerance specific to a given situation.

3.2 Thermal Error Index (TEI)

The second method, based on the approach recommended by the American National Standard Institute (ANSI) in its standards dealing with environmental conditions for dimensional measurements, involves linear addition of absolute values to estimated limits of error [2]. In this approach, the estimated worst-case limit of error e_c associated with the correction for thermal expansion given by Eq. (4) is

$$e_c = \left|\frac{\partial L}{\partial T}\right| e_T + \left|\frac{\partial L}{\partial \alpha}\right| e_\alpha, \tag{9}$$

which, with partial derivatives from Eq. (4), becomes

$$e_c = |\alpha L_0| e_T + |L_0 (T - T_0)| e_\alpha, \tag{10}$$

where e_T and e_α are worst-case errors in temperature and thermal-expansion coefficients and the terms proportional to each are the errors in the correction for thermal expansion due respectively to nominal differential expansion and the temperature variation.

In the ANSI standard which specifies the temperature conditions for dimensional measurements, Thermal Error Index (*TEI*) is defined and represented formally by:

$$TEI = [(TVE + UNDE)/WT] \times 100\% \leq 50\%, \tag{11}$$

where *TEI* is the thermal error index, *UNDE* is the stated uncertainty (no further specification) of nominal differential expansion times the temperature difference, *TVE* is a temperature variation error (defined by a maximum range of temperature drift), and *WT* is the working tolerance for a specific test. According to ANSI-standard procedures for evaluating the performance of dimensional measuring machines, the *TEI* should be less than 50% [8].

The parallelism of the two terms of the Thermal Error Index given by Eq. (11) with those of the variational form of thermal-expansion errors on length given by Eq. (9) suggests that a useful basis for estimating the significance of thermal-expansion effects in dimensional measurements in a specific situation is to determine whether the ANSI-specified condition on *TEI* is met, that is, whether the worst-case limit of error defined by Eq. (10) meets the following condition:

$$e_c/\mathcal{T} \leq 1/2, \tag{12}$$

where *WT*, the symbol for the working tolerance used in the standard, has been replaced by $\mathcal{T}$, the symbol for the specified tolerance introduced in the definition of Thermal Uncertainty Index defined in Eq. (8).

3.3 Interpretation of Statements of Accuracy, Uncertainty, and Error

This report follows the NIST policy on statements of uncertainty associated with measurement results which gives procedures for combining various statements of accuracy, uncertainty and limits of error from other sources, including published measurement data, manufacturer's specifications, data in calibration and other reports, and reference-data handbooks [9].

Throughout this report, unless otherwise noted, unqualified statements of accuracy, uncertainty and limits of error that are taken from other sources are indicated as "stated uncertainty" (des-

ignated in Tables by the symbol Δ) and discussed as such, but, when combined, are converted to the standard-uncertainty representation by assuming a uniform or rectangular probability distribution with

$$U = 2\,u = \frac{2}{\sqrt{3}}\,a = 1.155\,a, \qquad (13)$$

where a is the stated accuracy, uncertainty or estimated limit of error in the reported source and the half width of the assumed distribution. Thus a value given in some source as "$Y \pm X\%$" is quoted here as a stated uncertainty of X but when combined to give an expanded uncertainty is represented as "$Y \pm 1.155 \times X\%$." Note for comparison that this method of conversion to an expanded uncertainty yields a result which is within 15% of both the unqualified original statement and a value reported at the 95% level of confidence, which is converted to the 2σ expanded uncertainty by multiplication by 2/1.96, but is that much outside the assumed uniform distribution and is, therefore, non-physical. Note, however, that since both are so converted, the ratio of the uncertainty to a tolerance is the same whether in the stated or expanded forms.

4. Uncertainties Due to Variations in Coefficient α

An uncertainty in measurement results from uncertainty in the particular value of the CTE, α, used to calculate a part's dimension at the reference temperature when measurements are made at another temperature. The uncertainty in the nominal CTE, while seldom considered in conventional dimensional metrology, has long been recognized as important for large parts (large αL_0) and for large temperature extrapolations (large $T - T_0$) [2,10]. Due to the trends which have made micrometer and nanometer tolerances more commonplace, errors and uncertainties due to thermal-expansion effects are now an important consideration for part sizes and temperature extrapolations not previously considered large.

4.1 Range of Reference Values of α

Table 1 shows the variety of values of CTEs of some metrologically important materials that can be found in references including handbooks for engineers, machinists, and material scientists. Among the materials are: the elements aluminum, iron, and silicon; specific alloys such as Al 6061 and stainless steel 304; general alloys such as cast iron and carbon steel; common Pyrex[1] (a borosilicate

Table 1. Variety of values of coefficients of thermal expansion (in ppm/°C) of some metrologically-important materials provided in various engineering references

Material	CRC [11]	MHB [12]	MSG [13]	ASM [14]	TPM [16]
Al	25	22.4		23.6	23.1
Al 6061			22.0	23.4	22.5
SS 304	17.3		10.6–17.8[a]	17.2	14.7
BeCu	16.7				16.2
Fe	12			11.7	11.8
Cast iron	13.5	11.8	10.6–18.7	8.1–19.3	11.9
C-Steel	12.1	11.4	13.5–15.2	11.6–12.6	10.7
Pyrex	3.2			3.2	2.8
Silicon	3		4.67	5	2.6
Fused quartz	0.42		0.56	0.55	0.49
Invar				0.64–2.0	0.13
Zerodur [12]					0.05

[a] Source identifies stainless steels only by type, e.g. austenitic, ferritic, and age-hardenable.

[1] Certain commercial equipment, instruments, or materials are identified in this paper to specify adequately the experimental procedure. Such identification does not imply recommendation or endorsement by the National Institute of Standards and Technology, nor does it imply that the materials or equipment identified are necessarily the best available for the purpose.

glass) and low-expansion materials, including vitreous silica (fused polycrystalline quartz) and Zerodur (a mixture of crystalline and polycrystalline quartz) [11–17]. Inspection of Table 1 shows the problem of determining a value of CTE for a specific object by looking up a value for a material, namely the variety of values likely to be encountered.

Variations among the values for the various materials from the references shown in Table 1 include, for example, 4.5 ppm/°C or 35% of the mid-range value for carbon steel, 7.0 ppm/°C or 50% of the mid-range value for the stainless steel (which includes CTEs for SS-301 and others from a reference which gives CTEs only for generic types of SS), and 11.2 ppm/°C or 75% of the mid-range for cast-iron.

Table 2 illustrates some likely causes for such variations in tabulated values of CTEs, with the 35% range of the extremes from the mid-value CTE encountered for carbon steel taken as an example. As with other materials, these causes of variations are differences in chemical composition, the physical processing to which the specific sample has been subjected, and the value or range of temperatures for which the coefficient is specified.

The first likely cause of differences in reported values of CTEs for nominally the same material is differences in chemical composition. In general, the name carbon steel encompasses a range of carbon concentration from a few tenths of one percent to nearly 1.5% and includes various small amounts of other elements such as Mn, P, S, Si, Cr, Ni, or Mo, with the values of CTE of annealed samples of carbon steels reported by one source ranging from 11.1 ppm/°C to 12.6 ppm/°C depending on composition [14].

The second likely cause of differences in reported values of CTEs for nominally the same material is differences in microstructure associated with the physical processing to which the sample of material has been subjected. These processes include combinations of mechanical working and heat treatment, such as hot rolling, cold rolling, drawing, casting and annealing. For example, the range of variation of the CTE of steel has been reported to be ±2% (0.2 ppm/°C) among samples cut from different locations in a large piece of steel that has been fully annealed, ±3% (0.3 ppm/°C) among many heats of nominally the same chemical content, ±5% (0.5 ppm/°C) between hot and cold rolling, and ±10% (1.1 ppm/°C) among several heat treatments [18]. For the carbon steel (AISI 52100) of gage blocks, the annealed and hardened states of the material have reported CTEs (20 °C to 100 °C) of 11.9 ppm/°C and 12.6 ppm/°C, respectively [15].

In the case of Invar, Table 1 shows a range of values of CTE from 0.13 to 2.0 ppm/°C for various types of mechanical working and heat treating. Such processing can increase or decrease CTEs and can yield positive, negative or zero values, each of which can vary with time. As indicated by Table 3, annealing of Invar can increase the CTE and quenching can decrease it. Cold working after quenching can reportedly produce a negative coefficient, with very low CTEs usually reverting with time to the normal value for the material [15].

The third likely cause of differences in reported values of CTEs for nominally the same material are differences in the values or range of temperatures for which the CTEs are given. Among the sources cited here the most typical situation is an average value for a range of temperature from 20 °C up to 100 °C or as much as 1000 °C. That such average values can be significantly different than the 20 °C standard-temperature value is shown by Table 4, which compares with its 20 °C value the mean CTE for the range 20 °C to 107 °C and also shows the temperature derivative of the CTE at 20 °C in both

Table 2. Variety of values of the coefficient of thermal expansion (CTE, in ppm/°C) of carbon steel reported in various sources

MHB [12]	CRC [11]	MSG [13]	ASM-1 [15]	ASM-2 [14]	TPM [10]
Steel, carbon	Plain carbon steel AISI-1020	Carbon steel hardening grades wrought $T = 21$ °C–649 °C	AISI grade 1020 (0.22%C) $T = 20$ °C–100 °C	Fe-C alloy 1.08% C $T = 20$ °C–100 °C	Carbon steel Fe + (0.7–1.4)%C well-annealed $T = 20$ °C
11.4	Typical 12.1	13.5–14.9	11.7	10.8	10.7 ± 0.7
		Carbon steel carburizing grades wrought $T = 21$ °C–649 °C	AISI grades 1070–1085 $T = 20$ °C–100 °C	Fe-C alloys 1.45% C $T = 20$ °C–100 °C	
		15.2	11.0–11.8	10.1	

Table 3. Effects of heat treatment and mechanical processing on the mean thermal expansion of Invar ($T = 16$ °C–100 °C)

Processing	Mean α (ppm/°C)
Quenched cold-drawn	0.14
Annealed quenched	0.5
Hot mill	1.4
Forged	1.7
19 h-cool from 830 °C	2.0

a ppm/(°C)^2 and %/°C form [16,17]. Note that for some materials the difference between the CTE at 20 °C and an average value, such as that for the range 20 °C–107 °C shown, can be substantial, including 1 ppm/°C (5%) for aluminum and its alloys, 0.5 ppm/°C (20%) for silicon, and 0.43 ppm/°C (300%) for Invar.

A further consideration in assigning a value of CTE to a particular object is whether the material of the object is homogenous. An obvious situation is that of a compound object, that is, an assembly consisting of materials with different coefficients. One example of such is a commercial ball-plate for performance evaluation of coordinate measuring machines, which consists of ceramic balls mounted in a steel plate [19]. Less obvious is the situation of case-hardened parts, where the surface to some depth has a different CTE than that of the interior. Due to such inhomogeneities, measured values of CTE for steel gage blocks have been observed to be length-dependent, ranging from an asymptotic 12.0 ppm/°C for lengths less than 50 mm to an asymptotic 10.6 ppm/°C for lengths greater than 500 mm, with a value of 11.5 ppm/°C for lengths near 100 mm [20].

4.2 Uncertainty in Specific Values of α

Given that the CTE of an object depends upon its homogeneity, chemical composition, history of thermal-mechanical processing (such as heat treatment, cold working, and hardening), and temperature, a basis for estimating the degree to which even well-characterized values of CTE are known is given by Table 5, which shows the stated uncertainties in CTEs for some calibration artifacts, standard reference data and standard reference materials.

As indicated in the first row of Table 5, the American National Standard ANSI/ASME B89.1.2 for gage blocks specifies that the CTEs of gage blocks conforming to the standard are stated to be "accurate to within ±10% of value stated for the blocks between 15 °C and 30 °C" [21]. The parallel international standard specifies that the CTE of steel gage blocks in the temperature range 10 °C and 30 °C be within the limits (11.5 ± 1.0) ppm/°C, an 8.7% tolerance [22].

Shown in the second row of Table 5 are the stated values of uncertainty specified with standard-reference-data values of CTE for materials covering a wide range of values [16]. As indicated by Table 5, typical reported uncertainties for what are averages over a number of well-annealed samples of specific-composition alloys are 5% and 7%.

In the third row of Table 5 are the stated uncertainties assigned to the values of CTEs of standard reference materials produced and sold as standards of thermal expansion for use in calibrating dilatometers [23]. As indicated, the stated uncertainty associated with each of these specific well-annealed samples of specific-composition reference materials is ±0.03 ppm/°C, which for materials such

Table 4. Calculated temperature-average (20 °C–107 °C) and temperature derivatives (20 °C) of thermal expansion coefficients (CTEs) for some metrologically important materials [11,12]

Material	α_{av} (20 °C–107 °C) (ppm/°C)	α (20 °C) (ppm/°C)	$(d\alpha/dT)_{20\,°C}$ [ppm/(°C)]^2	$(d\alpha/\alpha dT)$ (%/°C)
Aluminum	24.2	23.1	0.009	0.04
Al 6061	23.7	22.5	0.023	0.10
BeCu		16.2	av $0.009_{280-299}$	0.06
Cast iron	12.0	11.9	0.0088	0.07
C-steel	11.9	10.7	0.018	0.17
Quartz	11.7	10.3	0.023	0.22
Pyrex	3.0	2.8	0.00083	0.03
Silicon	3.1	2.6	0.0031	0.12
Fused quartz	0.60	0.49	0.00032	0.07
Invar	0.56	0.13	0.012	9.2
Zerodur	0.05	< 0.05	$< 0.0015_{293-318}$	

Table 5. Comparison of the stated uncertainties in coefficients of thermal expansions associated with various standard gages, data, and materials

Specifier	Material	α (ppm/°C)	Δ_α/α (%)	Δ_α (ppm/°C)
ANSI standard for gage blocks [22]	Stainless steel	To be stated by manufacturer of G-blocks	±10% of stated value	1–1.5
	Cr-plated steel			1.1
	Chrome carbide			0.8
	Tungsten carbide			0.4
TPM standard reference data [17]	Aluminum	23.1	3%	0.7
	Al 6061	22.5	7%	1.6
	Carbon steel	10.7	7%	0.75
	Silicon	2.6	5%	0.13
	Fused quartz	0.49	5%	0.025
NIST standard reference matls [24]	Copper	16.64	0.18%	0.03
	SS-446	9.76	0.31%	0.03
	BS-glass	4.78	0.63%	0.03
	Fused SiO_2	0.48	6.3%	0.03
NRLM dilatometer results [25]	Duraluminum	23.129	0.37%	0.086
	Copper	16.556	0.33%	0.055
	C-steel (0.55%)	11.314	0.36%	0.038
	Invar	0.351	2.0%	0.007
	Glass ceramic	0.000		0.006

as steels with coefficients of the order of 10 ppm/°C corresponds to approximately 0.3%.

Finally, in the fourth row of Table 5 are the stated uncertainties of recent dilatometer measurements by a national standards laboratory on a range of materials, including, for example, one of the standard reference materials shown in the third row [24]. As indicated, the reported uncertainties for each of these materials vary from a high of 0.086 down to a low of 0.006 ppm/°C. Representative of the stated uncertainties in the CTEs of these standard reference materials is the 0.36% value for the materials other than the zero-expansion glass-ceramic.

Taken together, Tables 1, 2, and 5 provide a basis for some generalizations about the expanded uncertainties of values of CTEs: First, with no further information about composition or history, the expanded uncertainty of the CTE for materials simply described as carbon steel, stainless steel or cast iron can be from 5 ppm/°C to greater than 10 ppm/°C (as indicated by Table 1 which includes ranges of reported values of 4.5 ppm/°C or 35% of the mid-range value for carbon steel, 7.0 ppm/°C or 50% of the mid-range value for stainless steel 304, and 11.2 ppm/°C or 75% of the mid-range for cast-iron).

Second, knowing only that a material is gage-quality carbon steel, tungsten carbide or chromium carbide, the expanded uncertainty of the material's CTE is likely to be of the order of 10% or 1 ppm/°C.

Third, with information about chemical composition, the expanded uncertainty in the tabulated values of CTEs of a variety of standard-composition substances including metals, alloys and non-metallic materials are usually of the order of 6% to 9%. (With this generalization, one should keep in mind that the standard reference data are usually for well-annealed specimens of a class of materials and sometimes includes an average over a range of compositions.)

Lastly, with direct measurements of CTEs obtained by dilatometry on particular specimens of materials with coefficients in the range of, say, 3 ppm/°C (such as silicon) to 23 ppm/°C (such as aluminum and its alloys), the expanded uncertainties in CTE are of the order of 0.3%.

5. Uncertainty in Temperature

Uncertainty in the measurement of the length of a part also results from the uncertainty in the value of the temperature of the part, because the temperature must be measured and used to calculate the part dimension at the reference temperature.

5.1 Sensor-Limited Uncertainty in Temperature Measurement

Table 6 shows representative limiting uncertainties, stated (Δ_T) and expanded (U_T), associated with the use of the major types of NIST-calibrated temperature sensor systems for the determination of an object's temperature and, for reference, the absolute limit of temperature measurement at 20 °C. This limit is the 0.0002 °C expanded uncertainty of a primary calibration of a SPRT, which is also the uncertainty with which the melting point of gallium, a defining point on the International Temperature Scale, can be realized [25].

In order of decreasing values, the stated (and expanded) uncertainties are: 1) 0.1 °C (0.12 °C) for a Type-T thermocouple with a reference junction in an ice bath and read-out with a digital voltmeter [26]; 2) 0.03 °C (0.035 °C) for a visually-read mercury-in-glass thermometer [26]; 3) 0.01 °C (0.012 °C) for well-selected glass bead thermistors [27]; 4) 0.002 °C (0.0023 °C) for Type-T thermocouples referenced directly against a standard platinum resistance thermometer (SPRT) in a temperature-controlled 20 °C cell [28]; and 5) 0.001 °C (0.002 °C) for one SPRT as sensor referenced against a second in a 20 °C cell [25].

5.2 Object Temperature Measurement

Figure 2 shows schematically the types of locations at which temperature measurements are made: (A) in the air (or liquid) medium surrounding the object or part the temperature of which is to be determined; (B) on the walls of the temperature-control enclosure surrounding the measuring machine; (C) on the measuring machine; or (D) on the object itself.

Because combinations of radiation, convection, and conduction within this overall system can produce differential heating or cooling, the temperature of the part as a whole is not necessarily the same as that of any these points of measurement, including a single point on the object. Uncertainty also results from nonuniformity of the temperature distribution over the part, or nonequilibrium of the part with the environment at which temperature is measured.

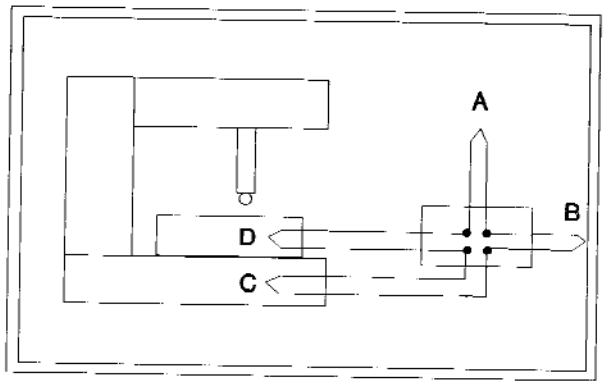

Fig. 2. Schematic representation of alternative locations of temperature monitors: (A) air surrounding object; (B) enclosure walls; (C) machine; (D) object of measurement itself.

5.3 State-of-the-Art Temperature Facilities

Table 7 shows, for state-of-the-art measuring and manufacturing systems, the stated temperature "stability" of each (taken to be the temporal variation about a mean temperature) and reported temperature "accuracy" (taken to be the stated uncertainty in that mean temperature). In each case, stated stabilities and accuracies are each treated as otherwise-unspecified single-component uncertainties obtained from quantities with uniform distribution and converted to expanded uncertainties by multiplication by 1.155.

In the order of decreasing expanded uncertainty, these systems include: (1) conventional metrology facilities with temperatures controlled to 0.12 °C; (2) two commercial laser-interferometer microelectronics mask measurement systems with stabilities

Table 6. Stated (Δ_T) and expanded (U_T) uncertainties in temperature measurement near 20 °C attainable by standard platinum resistance, bead-in-glass thermistor, type-T thermocouple, and mercury-in-glass thermometers

Sensor	Reference	Instrument	Bath	Δ_T (stated)	U_T (expanded)
SPRT	Ga-Pt			0.0001 °C (σ)	0.0002 °C
SPRT	SPRT	Bridge	20 °C Cell	0.001 °C (σ)	0.002 °C
TC	SPRT	Bridge	20 °C Cell	0.002 °C	0.0023 °C
Thermistor		Bridge		0.01 °C	0.012 °C
Hg-glass				0.03 °C	0.035 °C
TC		DVM	0 °C Junc	0.1 °C	0.12 °C

Table 7. Temperature stabilities and uncertainties reported for various state-of-the-art dimensional-measurement instruments and facilities

Instrument/facility with high-performance temperature system	Reported "stability"	Reported "accuracy"	Expanded uncertainty
Primary-std linescale calibration		0.002 °C	0.0023 °C
Large-optics-diamond-turning machine	0.006 °C	0.01 °C	0.010 °C
Primary-std-lab CMM calibration		0.01 °C	0.012 °C
Commercial IC mask metrology system	0.01 °C		0.012 °C
Commercial IC mask metrology system	0.05 °C		0.058 °C
Conventional CMM laboratory		0.1 °C	0.12 °C

of 0.058 °C and 0.012 °C, respectively [29,30]; (3) Physicalish-Technische-Bundesanhalt's special metrology facility controlled to 0.012 °C [31]; (4) Lawrence-Livermore's Large Optics Diamond Turning system with a measured stability of its surrounding air environment of 0.001 °C and an expanded uncertainty of 0.012 °C [32]; and (5) NIST's Linescale Interferometer System with a temperature measurement expanded uncertainty of 0.0023 °C [28].

6. Thermal-Expansion Analyses of State-of-the-Art Engineering Measurement Systems

Table 8 shows reported results of analyses of thermal expansion effects in three state-of-the-art engineering measurement systems. The systems are: 1) a specialized measuring machine for inspecting the mating features of the solid rocket motor of the U.S. Space Shuttle; 2) a commercial

Table 8. Stated incremental, fractional length and fractional tolerance uncertainties compared to the Thermal Error Indices (*TEI*) for three state-of-the-art engineering measurement systems

	Rocket motor seal	CMM step gage	X-ray mask
Dimension	3650 mm	1000 mm	50 mm
Materials	Aluminum/steel	Steel/Zerodur	Silicon
α (ppm/°C)	23.4/12.2	11.5/0.00	2.8
Δ_α (ppm/°C)	1.2/0.6 (5%)	0.1/0.05	(3%)
$(T - T_0)$	Worst: 11.1 °C Ideal: 0 °C	1 °C	0 °C
Δ_T	Worst: 0.9 °C Ideal: 0.36 °C	0.1 °C	0.01 °C
T	127 μm	1.33 μm	1.5 nm
Δ_L	Worst: 95.3 μm Ideal: 17.6 μm	Steel: 1.80/1.27 μm Z-dur: 0.61/0.55 μm	1 nm
Δ_L/L	Worst: 27 ppm Ideal: 4.8 ppm	Steel: 1.8/1.3 ppm Z-dur: 0.6/0.6 ppm	0.02 ppm
Δ_L/T	Worst: 75% Ideal: 14%	Steel: 135%/96% Z-dur: 46%/41%	67%
TEI	Worst: 47% Ideal: 12%	Steel: 94% Z-dur: 4%	67%

high-accuracy coordinate measuring machine used, for example, in automobile manufacturing; and 3) a specialized metrology system required for measurement of new-generation x-ray lithography masks. Based on stated uncertainties in thermal expansion (Δ_α) and temperature (Δ_T), the stated uncertainties are represented in incremental length (Δ_L), fractional length (Δ_L/L), and fractional tolerance (Δ_L/T) forms and compared with the ANSI-Standard Thermal Error Index (TEI).

6.1 Solid Rocket Motor Seal

In the second column of Table 8 are shown data and results of an analysis of the stated measurement uncertainties of a special-purpose profile measuring device developed for the U.S. space program to measure the absolute diameters of mating features of the redesigned joints of the Space Shuttle solid rocket motor subsequent to the failure which destroyed the Challenger [10]. The analysis deals with the case of an aluminum-arm measuring device calibrated at one temperature and used to measure the 3.65 m (144 in) diameter of a steel part at another temperature as much as 11.1 °C (20 °F) different. Machine and part temperatures are stated to be controlled to ±0.27 °C (0.5 °F). With use of reference-table values of CTE of aluminum and steel, assumption of stated uncertainties in CTEs of ±5%, and linear addition of absolute values of probable errors, the result of the analysis is that the machine's stated uncertainty is 95.3 μm (0.00375 in), representing 27 ppm of part size and 75% of the specified 127 μm (0.005 in) tolerance. The analysis also notes that with machine calibration and part measurement carried out under the improved temperature conditions of (20.0 ± 0.36) °C [(68.0 ± 0.2) °F] noted in Table 7 as ideal, the machine's stated uncertainty improves to 17.6 μm (0.0021 in) which is 4.8 ppm and 14% of tolerance, that is, of maximum permissible error.

6.2 High-Accuracy Coordinate Measuring Machine

In the third column of Table 8 are shown data and results of the vendor's analysis of the stated measurement uncertainty of a commercial coordinate measuring machine (CMM) of the type used, for example, in the aerospace and automobile industries [33]. The problem is to determine under what thermal-expansion conditions it can be determined that a CMM performs within its stated uncertainty:

$$U_1/\mu\text{m} = 0.5 + [L/\text{mm}]/1200 \quad (14)$$

using a step gage with stated calibration uncertainty:

$$A/\mu\text{m} = 0.05 + [L/\text{mm}]/2000 \quad (15)$$

where U_1 is the single-axis linear uncertainty for CMMs stated in the form specified by the German industrial standard [34] and A is the vendor-stated calibration uncertainty of the step gage, and L is distance in mm.

The vendor's analysis deals with the case of using a step gage one meter in length at a temperature chosen to be 21 °C controlled to ±0.1 °C under four conditions: step gage of either steel with a CTE of (11.5 ± 0.1) ppm/°C or Zerodur with a CTE of (0.00 ± 0.05) ppm/°C and uncertainties combined either in absolute values or root-sum-of-squares. The reported result is that the machine can only be satisfactorily determined to perform to a stated uncertainty of 1.33 μm at one meter using the Zerodur gauge. When added in absolute values and root-sum-of-squares, the resulting uncertainty in measurements with the steel step gage comprise respectively 135% and 96% of the tolerance. With the Zerodur step gage, in each case they comprise less than 50%, the implication being that the use of a Zerodur gage more satisfactorily allows the machine's performance to be judged to be within the manufacturer's stated uncertainty.

6.3 X-Ray Lithography Photomask

In the fourth column of Table 8 are shown data and results of a national laboratory's analysis of the stated uncertainty required to calibrate a reference dimensional standard for x-ray lithography photomasks [35]. The analysis deals with the case of a one-gigabit DRAM device and the reductions in uncertainties required at each successive level of the process: a critical dimension (CD) of 175 nm to 200 nm, with error of overlays (EOW) on wafers of CD/2.5, image placement accuracy (IPA) on masks of EOW/3, required industrial reference metrology accuracy (IRM) of IPA/4 and required national laboratory uncertainty of IRM/4, the resulting uncertainty required of the national laboratory is 1.25–1.75 nm, shown in Table 8 as a tolerance, i.e., permissible limit on measurement uncertainty, of 1.5 nm. Based on a reference-table value of CTE for silicon known to ±3% [16], the analysis shows that measurements made at the 20 °C reference temperature to a state-of-the-art level of tempera-

ture control of 0.01 °C yield an expanded uncertainty of 1 nm, representing 0.02 ppm of positional accuracy on the 50 mm wafer and 67% of the tolerance on the stated calibration uncertainty.

For each of the three examples, Table 8 also gives calculated values of *TEI* and shows the following results. In the rocket-motor example, the worst-case uncertainties due to differential thermal-expansion effects of the measuring arm and part just meet the ANSI B89 standard condition of $TEI \leq 50\%$. In the CMM example, while the test with the Zerodur step gauge meets that condition, that with the steel step gauge does not. In the x-ray mask example, for that condition to be met a uniform part temperature known to better than 0.01 °C is required.

7. Limiting Situations in Calibrations and Measurements

Based on the results of previous sections, Table 9 shows for various measurement situations the uncertainties in length measurements in terms of increments, fractions of the dimension measured and fractions of specified tolerances on the two bases described in Sec. 3. In the middle section of Table 9 are given stated uncertainties for CTE (Δ_α) and temperature (Δ_T) combined in absolute values according to Eq. (10) to provide a stated uncertainty in length (Δ_L), and *TEI*, and comparison to a stated tolerance ($\mathcal{T}$) as in Eq. (11). In the lower section of Table 9 are given expanded uncertainti for *CTE* (U_α) and temperature (U_T) combined sum-of-squares to provide an expanded uncertair in length (U_L), a *TUI*, and comparison to an e panded-uncertainty tolerance ($\mathcal{T}$) as in Eq. 8.

7.1 Limit of Definition of Temperature

The second column in Table 9 shows that f materials having CTEs in the range of nominal v ues 2.5 ppm/°C to 25 ppm/°C (which includes mat rials from silicon through steel to aluminum), tl current ±0.0001 °C standard uncertainty of tl definition of temperature corresponds to a sta dard uncertainty in length ranging from 0.25 nm 2.5 nm at 1 meter. Given that, by international ar national standard, the length of an object is d fined at a uniform temperature of 20 °C and th uncertainty of temperature measurement is limite by that of the ITS-90 temperature scale at th reference temperature uncertainty, the secon column of Table 9 shows that the correspondin expanded uncertainty in length measurement 5×10^{-10} represents the current absolute limit fc which a standards-defined length of the materia indicated can be determined.

For reference, Table 10 shows the limiting value of relative expanded uncertainty of length mea surements (U_L/L) for material objects of low expansion materials imposed by ITS-90 compare to the expanded uncertainty in the wavelengt of the iodine-stabilized helium-neon lase

Table 9. Comparison of thermal error indices (*TEI*), based on stated uncertainties, and Thermal Uncertainty Indices (*TUI*), based o expanded uncertainties, for various situation and thermal conditions

	ITS-90	Lab 20 °C	MC goal	Primary	Secondary	Tertiary	L-screw	Piston
Dimension	1 m	1 m	70 mm	1 m	1 m	1 m	1000 mm	100 mm
Material	Si-to-Al	Si-to-Al	Si	Steel	Steel	Steel	Steel	Al
α (ppm/°C)	2.5–25	2.5–25	2.6	11.75	11.8	11.8	11.5	23.4
$(T - T_0)$			0.000 °C	0.01 °C	0.1 °C	1.0	3 °C	3 °C
Δ_α (ppm/°C)				0.03	0.03	0.6	≥0.6	
Δ_T	0.0001 °C[a]	0.001 °C	0.001 °C	0.002 °C	0.01 °C	0.1		
$\mathcal{T}$			1 nm	0.1 μm	1.25 μm	12 μm	33.3 μm/m	7.6 μm
Δ_L	0.25–2.5 nm	2.5–25 nm	0.18 nm	24 nm	0.12 μm	1.8 μm	1.8 μm/m	7.0 μm
Δ_L/L	$\geq 2.5 \cdot 10^{-10}$	$\geq 2.5 \cdot 10^{-9}$	$2.6 \cdot 10^{-9}$	$2.4 \cdot 10^{-8}$	$1 \cdot 10^{-7}$	$2 \cdot 10^{-6}$	$1.8 \cdot 10^{-6}$	$7 \cdot 10^{-5}$
TEI			18%	25%	10%	24%	5%	92%
U_α (ppm/°C)					0.035	0.035	0.7	0.7
U_T	0.0002 °C	0.0012 °C	0.0012 °C	0.0023 °C	0.012 °C	0.12 °C		
$\mathcal{T}$			1.2 nm	0.12 μm	1.4 μm	13.8 μm	38.3 μm	8.7 μm
U_L	0.5–5 nm	2.9–29 nm	0.22 nm	27.6 nm	0.14 μm	1.3 μm	2.1 μm/m	7.0 μm
U_L/L	$\geq 5 \cdot 10^{-10}$	$\geq 3 \cdot 10^{-9}$	$3.1 \cdot 10^{-9}$	$2.8 \cdot 10^{-8}$	$1.4 \cdot 10^{-7}$	$1.3 \cdot 10^{-6}$	$2.1 \cdot 10^{-6}$	$7 \cdot 10^{-5}$
TUI			18%	23%	14%	10%	5%	80%

[a] Stated uncertainty for this case was one standard deviation; all other examples were unspecified and treated as uniform distributions.

Table 10. Relative expanded uncertainty in length for low-expansion materials due to the 0.0002 °C limit of ITS-90 compared to the relative expanded uncertainty in length due to uncertainty in the I-HeNe wavelength

Matl	α (ppm/°C)	U_L/L
Steel	11.5	23.0×10^{-10}
Silicon	2.6	5.2×10^{-10}
Invar	1.0	2.0×10^{-10}
Fused quartz	0.4	0.8×10^{-10}
$^{127}I_2$-HeNe	0.25	0.5×10^{-10}
Zerodur	0.05	0.1×10^{-10}

($\delta\lambda/\lambda = 5.0\times10^{-11}$ [36]) by which the SI unit of length in engineering measurements is practically defined. Table 10 also shows the value of CTE, 0.3 ppm/°C, at which the contributions to the uncertainty in a length measurement of the uncertainty in the ITS-90 temperature scale and of the reference wavelength are equal, that is, where

$$U_L/L = \alpha U_{\mathrm{ITS}} = (U_\lambda/\lambda)_{\mathrm{HeNe}}. \qquad (16)$$

As indicated in Table 10, for materials with CTEs greater than the 3.4 ppm/°C, which value is near that of silicon and Pyrex (borosilicate glass), a lower limit of the uncertainty of any measurement of the length of a material object is imposed by the uncertainty in temperature defined by ITS-90, while for materials with CTEs less than 3.4 ppm/°C (including Invar, fused silica, and Zerodur) a larger uncertainty is imposed by the uncertainty in the wavelength of the iodine-stabilized laser.

7.2 Limit of Realizing 20 °C in the Laboratory

The third column of Table 9 shows again for materials ranging from silicon to aluminum that the practical limit of realizing 20 °C, achievable with high- but not ultimate-performance equipment such as an 8½-digit voltmeter and best laboratory practice, is about ±0.001 °C [25,37]. This temperature corresponds to an expanded uncertainty in length of 2.5 nm–25 nm at one meter. Thus, in terms of fractional length (U_T/L), 3 parts in 10^9 currently represents the lowest uncertainty with which a length of a material object can be determined.

7.3 Design Goal of M3

The fourth column of Table 9 shows the design parameters and performance goals for the Molecular Measuring Machine (M3), a laser-interferometer and STM-probe planar coordinate measuring machine being constructed at the National Institute of Standards and Technology [38]. With the SPRT-SPRT thermometry described in Table 6 in which one SPRT acts as sensor for monitoring the temperature of the part carrier and the other acts as the reference, the M3 goal is to be able to achieve for a silicon wafer of 70 mm diagonal a temperature which is uniform, stable and accurate to 0.001 °C, the current practical limit of realizing the reference temperature in a laboratory. For M3 that limit of measurement of part temperature corresponds for a silicon part to an expanded uncertainty in length of 0.22 nm at 70 mm (3.1 part in 10^9) or 18% of the machine's design goal for point-to-point position measurement.

7.4 Primary Calibration Laboratory

The fifth column of Table 9 shows operational parameters for the NIST Length Scale Interferometer, a primary-calibration facility the accuracy of which is checked through international round-robins aimed at assessing the capabilities of national laboratories in various industrialized nations to realize the definition of the meter [28]. For the steel meter-bar used in such intercomparisons, the stated 0.002 °C expanded uncertainty in part temperature and offsets of no more than 0.01 °C from the 20 °C reference temperature corresponds to 24 nm at 1 m, which is 2.4 parts in 10^8 or 25% of a nominal expanded uncertainty of 0.1 μm at a meter.

7.5 Secondary Calibration Laboratory

The sixth column of Table 9 shows operational parameters of a hypothetical secondary calibration laboratory representative of current good practice among industrial and government metrology facilities. With CTEs known to the standard-reference-material level of ±0.03 ppm/°C of Table 9, temperature controlled to a state-of-the-art facility level of ±0.01 °C, and part temperature offsets from the reference temperature of no more than 0.1 °C, the thermal-expansion contribution to length measurement expanded uncertainty corresponds to 0.14 μm at 1 meter or 1.4 parts in 10^7, which represents 14% of an expanded uncertainty of 1.25 μm at a meter representative of the uncertainties of today's high-performance CMMs.

7.6 Tertiary-Calibration/Industrial-Inspection Laboratory

The seventh column of Table 9 shows operational parameters of a tertiary calibration laboratory which can be representative of industrial part-inspection facilities. With CTEs assumed to be known to standard-reference-data values of ±5%, temperature controlled to a conventional metrology facility level of ±0.1 °C, and part temperature offsets from the reference temperature of no more than 1 °C, the thermal-expansion contribution to possible error corresponds to 1.8 μm at 1 m or 2 parts in 10^6, which represents 15% of the 12 μm tolerances on transmission housings, clutch covers, and meter-size automobile engine blocks and cylinder heads measured by commercial CMMs [39].

7.7 Change in Reference Temperature

The eighth and ninth columns of Table 9 show two examples of the effects on possible error in industrially important applications cited in research and trade journal editorials concerning the recent unadopted ISO proposal to change the standard reference temperature for dimensional measurements from 20 °C to 23 °C [40,41].

The example shown in column 8 of Table 9 is that of a calibrated steel lead screw in a machine tool or measuring machine. The CTEs of even highly controlled products such as gage blocks or lead screws is said to be known to vary from lot to lot by 5%. Here it is shown that, with a standard still calibrated at 20 °C, this stated 5% uncertainty in the CTE coupled with the 3 °C temperature shift would give rise to a possible error contribution of 1.8 parts in 10^6, which would add 1.8 μm/m or 5% to the 33.3 μm/m (0.0004 in/ft) value cited as the error of the steel lead screw of an accurate machine tool, an amount which is considered significant in terms of the machine's intended limit of permissible error.

The example shown in the last column of Table 9 is that of a nominally 100 mm-diameter (4 in) aluminum engine piston. In this case, the dimension of the part measured at a "new" reference temperature of 23 °C has an expanded uncertainty relative to that of a part designed to be measured at the "old" reference temperature of 20 °C of 7 μm or nearly the entire 7.6 μm (0.0003 in) of the initial tolerance for piston-to-cylinder fit for many engines, an effect considered likely to be improperly compensated and a major potential problem in fit and function.

8. Conclusion

This paper has examined the effects on unce tainties in dimensional measurements due to u certainties in the temperature and coefficients thermal expansions for both physical-artifact sta dards and manufactured workpieces. The motiv tions for this examination are both the trends t tighter tolerances in discrete-part manufacturin which pose great challenges in dimensional metro ogy, and also the proposed change in the standar reference temperature at which such dimensio are defined.

The paper's principal conclusion is that, unde common conditions of temperature measuremen and knowledge of coefficients of thermal expan sions of engineering materials, the contributions o thermal-expansion effects to measurement uncer tainty are frequently large, sometimes dominant and occasionally overwhelming factors relative t tolerances specified in precision-tolerance manu facturing.

This paper also shows that increased accuracy i the determination of the temperature and coeffi cient of thermal expansion of the part or standar being measured is of increasing importance whe state-of-the-art precision-tolerance parts are bein inspected. Finally, the paper's results support th view that a change in the reference temperatur from 20 °C to 23 °C, without recalibration of refer ence standards at the new temperature, can intro duce changes in dimensions and uncertainties in dimensional measurements which are substantial compared to manufacturing tolerances and industrial measurement-accuracy requirements.

9. References

[1] ISO-1, Standard Reference Temperature for Industrial Length Measurements, International Organization for Standardization, Geneva, Switzerland, 1989.

[2] American National Standard, Temperature and Humidity Environment for Dimensional Measurement, ANSI B89.6.2-1973, American Society of Mechanical Engineers, 345 E. 47th St., NY, NY 10017, 1973.

[3] N. Taniguchi, Current Status and Future Trends of Ultraprecision Machining and Ultrafine Materials, Annals of the CIRP (International Institute of Production Research), 2(5), 1–10 (1983).

[4] D. A. Swyt, Challenges to NIST in Dimensional Metrology: The Impact of Tightening Tolerances in the U.S. Discrete-Part Manufacturing Industry, NISTIR 4757, Natl. Inst. Stand. Technol., January 1992.

[5] ISO TC-3/SG-1, Reference Temperature, International Organization for Standardization, Geneva, Switzerland, April 1992.

[6] ISO, Guide to the Expression of Uncertainty in Measurement, prepared by ISO Technical Advisory Group 4 (TAG #4), Working Group 3, International Organization for Standards, Geneva, Switzerland, September 1993.
[7] NIST Technical Communications Program, Statements of Uncertainty Associated with Measurement Results, NIST Administrative Manual, Subchapter 4.09 Appendix E, Natl. Inst. Stand. Technol., October 1993.
[8] American National Standard, Methods for Performance Evaluation of Coordinate Measuring Machines, ANSI B89.1.12M-1990, American Society of Mechanical Engineers, 345 E. 47 St, NY, NY 10017, 1973.
[9] B. N. Taylor and C. E. Kuyatt, Guidelines for Evaluating and Expressing the Uncertainty of NIST Measurement Results, NIST Tech. Note 1297, October 1993.
[10] W. T. Estler, Accuracy Analysis of the Space Shuttle Solid Motor Profile Measuring Device, NISTIR 89-4171, Natl. Inst. Stand. Technol., November 1989.
[11] CRC Handbook of Tables for Applied Engineering Science, CRC Press, Cleveland, OH (1973) Al, Fe, Si, p.119; Pyrex, Fused Silica, Silicon, p. 249; Carbon Steel, Cast Iron, BeCu 25, p.118.
[12] Machinery's Handbook, Industrial Press, New York, New York (1980) p. 2270.
[13] Materials Selector 1991, Materials Engineering, Penton Publishing, Cleveland OH, December 1990, pp. 24–26, with values for SS in general.
[14] ASM Metals Reference Book, 2nd ed, American Society for Metals, Metals Park, OH 44073 (1983) Al 6061, Pure Fe, Invar (36% Ni-Fe), Gray Cast Iron, Malleable Iron (Pearlitic), Silicon, pp. 92–93.
[15] Metals Handbook, 9th ed, American Society for Metals, Metals Park OH 44073 (1978) Stainless Steel 304, p. 34, Invar, p. 794, Vol. 3, Carbon Steels 1008/1010, p. 147, v. 1, and Borosilicate Glass (Pyrex), Fused Quartz, p. 1057, v.4.
[16] Thermophysical Properties of Matter, IFI-Plenum Press, NY (1975) Al, p. 2, v. 12; Al 6061, p. 1028, v. 12; BeCu, p. 679, v. 12; Fe, p. 157, v. 12; Cast Iron, p. 1131, v. 12; Carbon Steel, p. 1131, v. 12; Pyrex, p. 1369, v. 13; Silicon, p. 154, v. 13; Fused Silica, p. 360, v. 13; Invar, p. 848, v. 12.
[17] Zerodur Product Literature, Schott Optical Glass Inc., Duryea, PA 18642 (1992).
[18] R. K. Kirby, Thermal Expansion Laboratory, National Bureau of Standards, in Ref. [2].
[19] Application Note KOBA KK25 KOBA-Check Ball Plate, Kolb and Baumann Co., Aschaffenburg, Germany D-8750 (1992).
[20] Private Communication, T. Doiron, unpublished data, Gage Block Laboratory, National Institute of Standards and Technology, Gaithersburg, MD 20899, Feb. 17, 1993.
[21] American National Standard, Precision Gage Blocks for Length Measurement, ANSI/ASME B89.1.9M-1984, American Society of Mechanical Engineers, NY, NY (1984).
[22] International Standard, Gage Blocks, ISO-3650-1978(E), International Organization for Standardization, Geneva, Switzerland (1978).
[23] N. M. Trahey, NIST Standard Reference Materials Catalogue, NIST Special Publication 260, February 1992 and Calibration Certificates for SRMs 736,738,731,739.
[24] M. Okaji and H. Imai, Precise and Versatile Systems for Dilatometric Measurement of Solid Materials, Precision Eng. **7** (4), 206–210 (1985).
[25] G. F. Strouse and B. W. Mangum, NIST Measurement Assurance of SPRT Calibrations of the ITS-90: A Quantitative Approach, in Proceedings of the Measurement Science Conference, Anaheim, CA, Jan. 1993 and Private Communication, February 5, 1993.
[26] J. Simmons, NIST Calibration User's Guide, Thermometer Calibration Uncertainties, NIST Special Publication 250, October 1991, p. 61.
[27] W. T. Estler, High-Accuracy Displacement Interferometry in Air, Appl. Opt. **24** (6), 808–815 (1985).
[28] J. S. Beers and W. B. Penzes, NIST Length Scale Interferometer Measurement Assurance, NISTIR 4998, Natl. Inst. Stand. Technol., Dec. 1992.
[29] Product Literature, Nikon 3i Laser Interferometric Measuring Machine, Nikon Corporation, Industrial Supplies and Equipment Division, Tokyo, Japan, 1992.
[30] Product Literature, Leitz LMS-2000 Laser Metrology System, Leitz-Image Micro Systems Co., Rockleigh, NJ, 1986.
[31] Private Communication, NIST Trip Report, Dr. Steve Phillips to Physicalisch-Technische Bundesanstalt, Braunschweig, Germany, Jun 1–3, 1991.
[32] T. W. Estler, Validation of Metrology of the Large Optics Diamond Turning Machine, NBSIR 85-3182(R), Natl. Bur. Stand. (U.S.) June 1985, pp. 23 and Appendix B-811.
[33] Private Communication, Peter Schafer, Carl Zeiss Inc., Division of Industrial Systems, Oberkochen, Germany, February 5, 1993.
[34] German Standard, Accuracy of Coordinate Measuring Machines, VDI/VDE 2617, Verband Deutscher Electrotechniker and Verein Deutscher Ingenieure, Beuth Verlag D-100, Berlin, December 1989.
[35] E. C. Teague, L. W. Linholm, M. W. Cresswell, W. B. Penzes, J. A. Kramar, F. E. Scire, J. S. Villarubia, J. S. Jun, Metrology Standards for Advanced Semiconductor Lithography Referenced to Atomic Spacings and Geometry, Proceedings of IEEE International Conference on Microelectronic Test Structures, March 22–25, 1993, Barcelona, Spain, Vol. 6, pp. 213–217.
[36] Recommended Radiations for Practical Realization of the Meter, Report of the 8th Meeting of the Consultative Committee on the Definition of the Meter, September 9–11, 1993, Sevres, France, to be published.
[37] Private Communication, G. Strouse, NIST Temperature Group, National Institute of Standards and Technology, Gaithersburg, MD 20899, Feb. 5, 1992.
[38] E. Teague, The National Institute of Standards and Technology Molecular Measuring Machine Project: Metrology and Precision Engineering Design, J. Vac. Sci. Technol. **B7** (6), 1898–1902 (1989).
[39] Private Communication, John Bosch, President, Giddings and Lewis, Instrument Systems Division, Nov. 1991.
[40] K. L. Blaedel, (Chairman ANSI B89.6), Comment, Precision Eng. **15** (1), 4–5 (1993).
[41] K. L. Blaedel and F. Parsons, ISO Studying Reference Temperature Change, Quality, Hitchcock Publishing Company, Carol Stream, IL, Feb 1993.

About the author: *Dennis A. Swyt is a physicist and Chief of the Precision Engineering Division at NIST. The National Institute of Standards and Technology is an agency of the Technology Administration, U.S. Department of Commerce.*

Volume 99, Number 1, January–February 1994
Journal of Research of the National Institute of Standards and Technology

[J. Res. Natl. Inst. Stand. Technol. 99, 45 (1994)]

A Null-Balanced Total-Power Radiometer System NCS1

Volume 99 | Number 1 | January–February 1994

Sunchana P. Pucic

National Institute of Standards and Technology,
Boulder, CO 80303-3328

A recently developed radiometer system NCS1 is used to calibrate thermal noise temperature at any frequency between 1.0 GHz and 12.0 GHz. Any cryogenic noise source can be measured; the upper limit of noise temperatures measured without a loss of accuracy is estimated to be about 10^5 K. For a typical hot noise source with the noise temperature of 8400 K and a reflection coefficient magnitude of 0.1, the expanded uncertainty is ≈1.8%, and the system sensitivity ≈2 K. Implemented in Type N connector, it can be easily modified to calibrate noise sources with other coaxial connectors or waveguide flanges.

Key words: calibration system; noise standard; noise temperature; null-balanced; radiometer; total power; waveguide-below-cutoff attenuator.

Accepted: October 12, 1993

1. Introduction

The Noise Calibration System Model 1 (NCS1), recently built at the National Institute of Standards and Technology, was designed to fill, in the field of thermal noise calibrations, the two overriding needs of calibration laboratories: the highest quality measuring capabilities and a price that is not prohibitive. Currently available commercial systems are not sufficiently sensitive to deliver the adequate accuracy, while the calibration radiometer systems developed previously at NIST may be too expensive to be duplicated by smaller laboratories.

The NCS1 is broadband, accurate, precise, and relatively inexpensive. Its sensitivity is adequate for its intended purpose of calibrating typical hot and cold laboratory and field noise sources (1.9 K with a 8400 K source, 0.09 K with a nominal 77 K cold load). Access to a vector network analyzer is required for reflection coefficient measurements.

The NCS1 can be easily modified to cover wider frequency and dynamic ranges, to accept noise sources with different connectors (or waveguide flanges) than the present Type N configuration, and to have a different null indicator.

2. Brief Description

The NCS1 consists of two noise standards and a null-balanced, total-power radiometer. In this implementation, one of the two standards is the NIST primary coaxial standard at the cryogenic temperature of liquid nitrogen; however, a calibrated commercial noise source may be substituted without significantly affecting performance [1]. The other standard is a commercial lossy termination held at ambient temperature.

The NCS1 is equipped with three switch-selectable input ports to accommodate the two standards and an unknown noise source, the device under test (DUT). Switching is controlled from a system control panel by the operator. Since different paths through the switch result in slightly different losses, the switch asymmetry is evaluated (by a

separate vector network analyzer), and used to calculate a correction factor (the "asymmetry correction").

A vector network analyzer is also used to evaluate reflection coefficients of the three NCS1 input ports, the nonambient standard, and the DUT. The results are used to calculate the second of the two correction factors (the "mismatch correction").

The measured values of the NCS1 input ports and the nonambient standard reflection coefficients are stored in look-up tables used by the NCS1 software and need to be only periodically re-evaluated.

The radiometer uses heterodyning to economically cover a broad frequency range, to facilitate frequency selectivity, and to allow for elective future expansion. Since RF sections of the radiometer require bandlimiting to an octave each (Sec. 3.3), there are four front ends corresponding to the four octaves covered (1–2 GHz, 2–4 GHz, 4–8 GHz, and 8–12 GHz). Selection of the appropriate front end is achieved from the system control panel.

A double-balanced mixer downconverts the RF noise to the 30 MHz IF frequency. Both sidebands are used; each has a bandwidth of about 4 MHz. Most of the system gain is achieved in the IF section. A precision waveguide-below-cutoff (WBCO) attenuator attenuates the different noise powers generated by the two standards and the DUT to the same power, thereby achieving a balanced operation mode.

An unbiased square-law diode serves as a detector. Nulling and resolution control are implemented at the post-detection stage. A strip-chart recorder functions as a low-cost null indicator.

Excluding the NIST primary coaxial standard, the NCS1 is constructed of commercially available components and housed in an ordinary equipment rack (Fig. 1). In order to minimize drifting due to ambient temperature variations, the radiometer and the ambient temperature standard are contained in a temperature-controlled enclosure. The temperature control is achieved by a small commercial water circulator housed in the same rack. All components are fastened to and are in good thermal contact with a brass plate, which is held at a uniform temperature by circulating water. Heat-generating components (amplifiers and mixers) have been positioned downstream from passive components. Off-line computer support is written in BASIC.

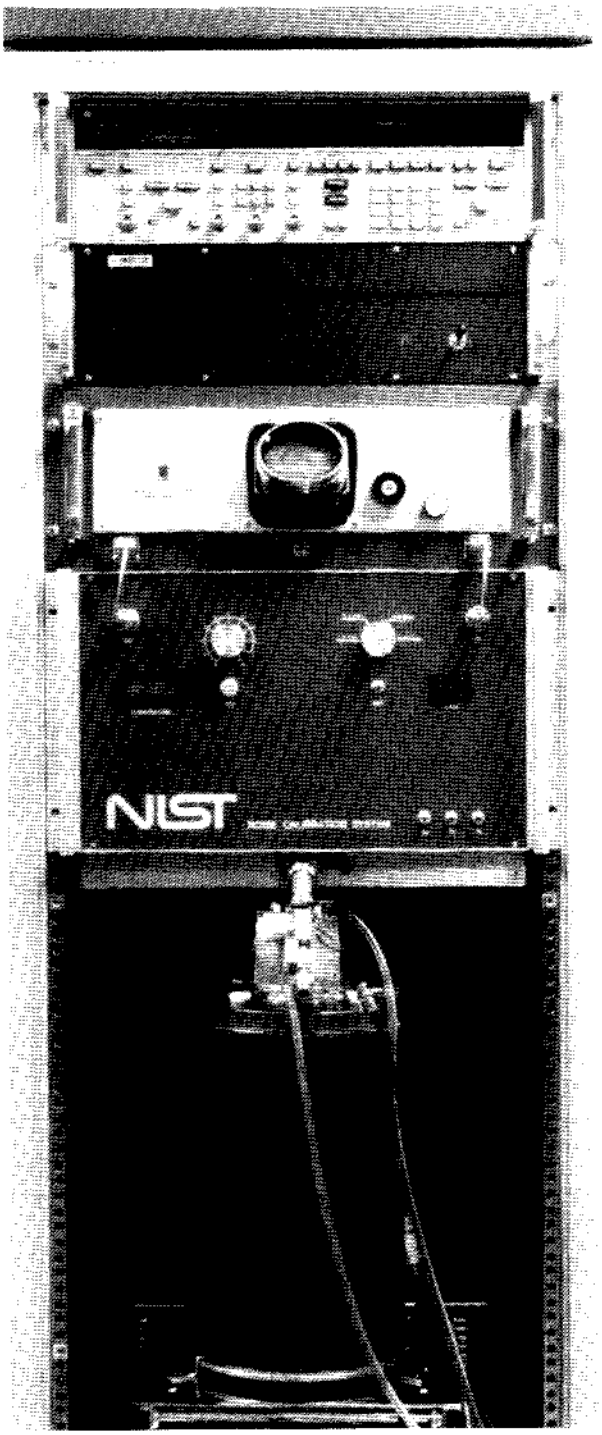

Fig. 1. Noise calibration system 1.

3. Noise Calibration System Model 1

A block diagram of the Noise Calibration System Model 1 is shown in Fig. 2. In the following sections, the two standards are briefly overviewed, and the radiometer is described in more detail.

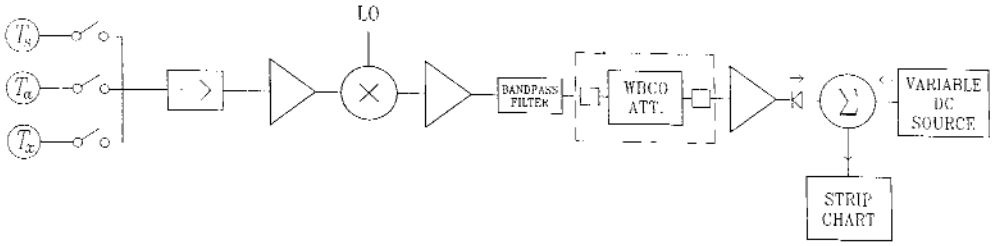

Fig. 2. NCS1 block diagram.

3.1 Cryogenic Temperature Standard

The NIST primary coaxial cryogenic noise standard is described in [2]. Briefly, it consists of a lossy termination with its connecting network (a beaded air-line, an adaptor, and the connector), a water jacket surrounding the output section, and a Dewar holding the liquid nitrogen at atmospheric pressure. All components are housed in an electrically conductive enclosure.

The temperature of the termination is uniform and held constant at the temperature of the liquid nitrogen, which is corrected for the small variations in the static pressure due to the head loss to evaporation, and the barometric pressure. The water circulating within a water jacket locks the temperature of the output section of the connecting network (the adaptor and the connector) to the ambient temperature. The temperature gradient along the length of the coaxial air-line is assumed to be linear with distance between the cryogenic termination and the room temperature connector.

The noise temperature at the output of the primary cryogenic standard, T_s, has therefore three calculable components: the major contribution of the lossy termination at the cryogenic temperature, and the minor contributions from the temperature transitional region (the low-loss coaxial air-line), and from the ambient temperature region (the low-loss adapter and connector). The expression used to calculate the output temperature [2] is incorporated into the NCS1 software.

3.2 Ambient Temperature Standard

The ambient temperature standard is a lossy termination whose temperature is held constant by circulating water. Its temperature is measured by a calibrated thermometer. Since every component of this standard is at the same (ambient) temperature, the losses in the connecting network are irrelevant. The output noise temperature of the ambient standard is simply its thermodynamic temperature T_a.

3.3 NCS1 Radiometer

The principle of the NCS1 is illustrated by the simplified block diagram in Fig. 3. The simplified radiometer consists of only four components: an isolator, a RF amplifier, a WBCO attenuator, and a receiver containing a square law detector. The input switch is omitted, and the noise sources attach directly to the single input port.

The radiometer input signal is the broadband noise generated by the three noise sources: the two noise standards and the DUT. Each of the three sources is sequentially attached to the radiometer input port, and the noise power is adjusted by the attenuator so that the receiver balances in all three cases.

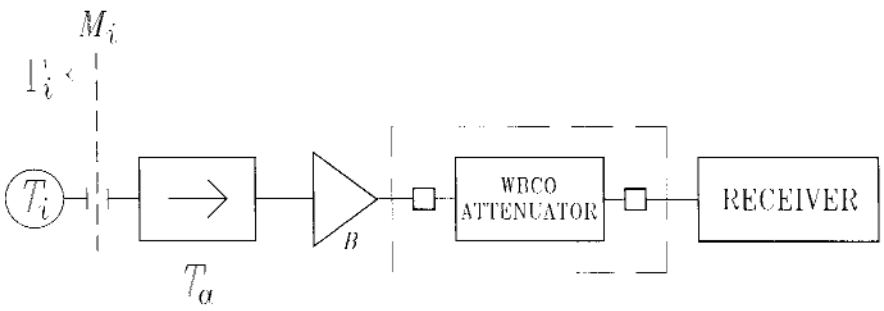

Fig. 3. Simplified system block diagram.

Following [3] and [4], the available noise temperature T_x of the DUT can be calculated by comparing it to the available noise temperatures T_s and T_a of the two standards, according to

$$T_x = T_a + \frac{M_s}{M_x}\,(T_s - T_a)\,\frac{10^{-(A_a - A_x)/10} - 1}{10^{-(A_a - A_s)/10} - 1}\,, \qquad (1)$$

where M_s/M_x is the mismatch correction at the input reference plane, and A_a, A_s, and A_x are the attenuator settings (in dB) needed for balance.

Three features help convert the idealized radiometer above into a workable instrument:

- In order to protect the connectors and facilitate the operation, an electrically operated single-pole, triple-throw coaxial switch, the input switch, is placed at the system input, effectively creating three separate, dedicated system input ports. The nonambient and ambient temperature standards and the DUT are then sequentially *switched into* the radiometer.

  There are two consequences of that arrangement: the different paths through the input switch result in different losses and require an *asymmetry* correction, and the finite isolation between the paths cause leakage, which, however, becomes negligible with a proper switch selection.

- In order to economically broaden the frequency coverage, heterodyning is employed. Since the input signal is wideband, it must be bandlimited ahead of the mixer, to avoid intermixing the out-of-band signals. The use of a double-balanced mixer, which suppresses second-order intermixing products, allows the RF sections preceding it to be a full octave wide. The bandlimiting is achieved by means of the RF amplifiers preceding the mixer, since passive filters resonate in their "far out-of-band" region and, therefore, fail to effectively achieve the bandlimiting goal. The same bandlimiting also eliminates problems of the noise signal mixing with harmonically related and out-of-band spurious signals originating in the local oscillator. The input noise signal is downconverted to 30 MHz, the value dictated by the commercial WBCO attenuator. Both sidebands are used, so the measured noise signal power is the *mean* of the powers contained in the two symmetrical bands, 60 MHz apart and filtered to be 4 MHz wide, centered around the LO frequency. The spectrum of the noise sources is assumed to be essentially flat within the resulting 64 MHz averaging interval.

  The fact that the noise is measured at LO ± IF and *not* precisely at the LO frequency, combined with the non-negligible electrical length of the input section in front of the isolator, results in a *broadband mismatch error* [1], [5].

- In order to implement a fully null-balanced system, the post- detection stage of the receiver includes DC nulling circuitry built around an operational amplifier. A strip-chart recorder serves as a null indicator.

Figure 4 shows a schematic diagram of the implemented radiometer.

The radiometer front ends are configured with the help of four switches, mounted on the control panel and labeled by the octaves they form, "1-2," "2–4," "4–8," and "8–12." The four switches control electrically operated internal switches, which are transparent to the user. There are two mixers in the radiometer, because no mixer covering the full 1 GHz to 12 GHz band was available. The resistive pads in front ends help equalize the signal at the mixer input (since RF amplifiers have all different gains). Numerous 3 dB and 6 dB pads inserted in the IF system improve amplifier stability by controling the internal reflections.

The total IF gain of the system is partitioned between the pre-attenuator and post-attenuator sections. Although any amplifier saturation in the post-attenuator section is inconsequential (so one is tempted to put all the amplifiers there), a certain amount of gain must precede the attenuator for two reasons: to make the noise contribution of the attenuator negligible in comparison with a much stronger (amplified) signal at the attenuator input, and to reduce the attenuator vulnerability to the electromagnetic interference.

3.3.1 The *available* noise temperature T_x of the DUT is calculated from the system equation [3]

$$T_x = T_a + \frac{M_s}{M_x}\cdot\frac{\eta_{sw_s}}{\eta_{sw_x}}\,(T_s - T_a)\,\frac{10^{-(A_a - A_x)/10} - 1}{10^{-(A_a - A_s)/10} - 1}\,, \qquad (2)$$

where, as before, T_s and T_a are the available noise temperatures of the two standards, M_s/M_x is the mismatch correction at the input reference plane, and A_a, A_s, and A_x are the attenuator settings needed for balance. Furthermore, η_{sw_s}/η_{sw_x} is the

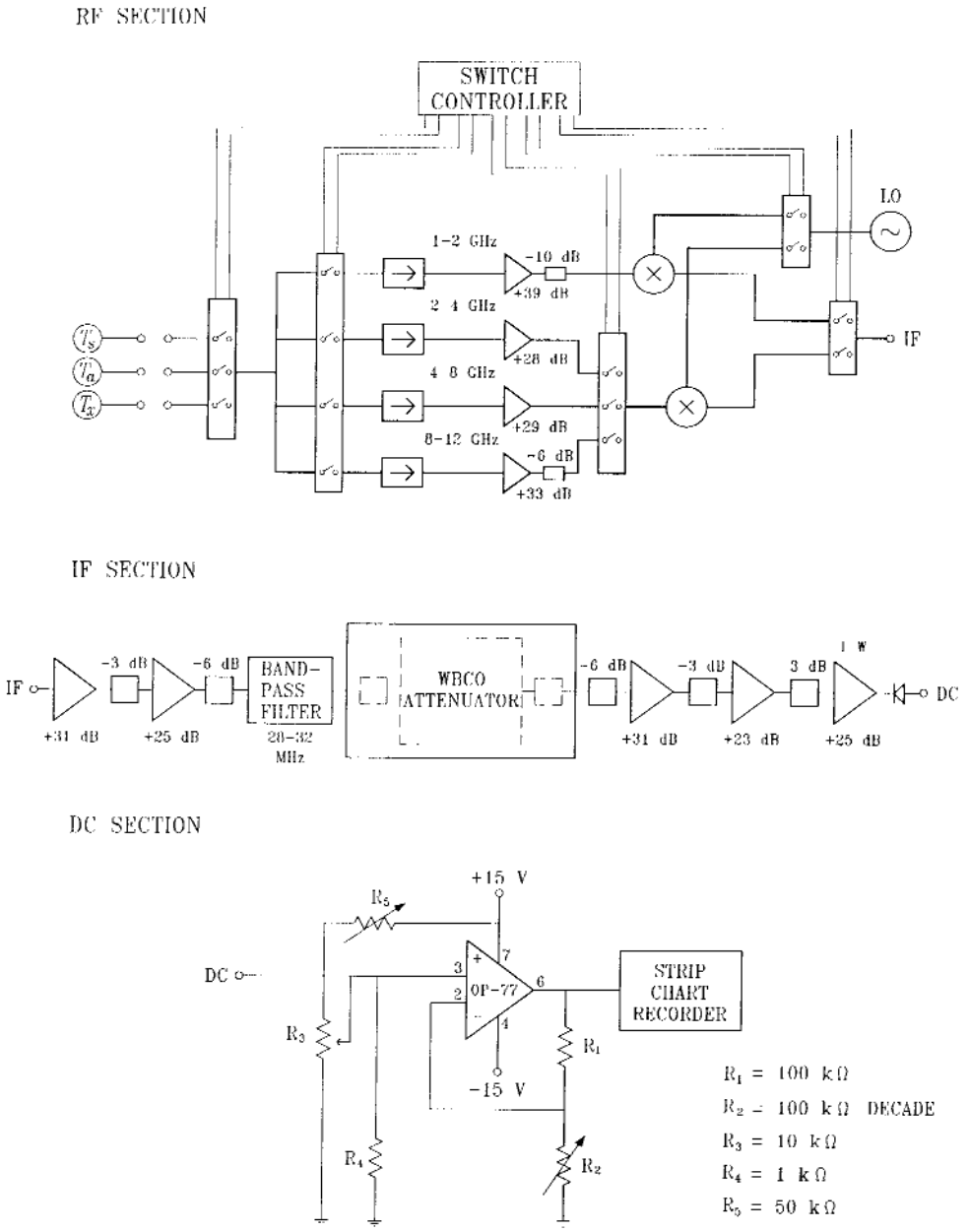

Fig. 4. Schematic diagram of NCS1.

input path asymmetry correction, a consequence of slightly different efficiencies of the two sides of the input switch. Both the mismatch correction and the asymmetry correction are evaluated using a vector network analyzer.

The analysis of uncertainty is presented in detail in [1]. Briefly, there are eight significant standard uncertainty components arising from systematic effects: two pertain to the standards and the rest to the radiometer and the DUT. The contribution of the random effects is small. The combined standard uncertainty is calculated by a root sum of squares (RSS) method. The expanded uncertainty is calculated by multiplying the combined standard uncertainty by the coverage factor of 2. For a typical DUT with a noise temperature of 8400 K and a reflection coefficient of 0.1, the expanded uncertainty is approximately 150 K.

3.3.2 System Sensitivity The sensitivity (the minimum detectable signal) of a radiometer with negligible short-term gain fluctuations is defined [6,7] as the minimum input signal noise temperature difference required to produce an output signal noise temperature having a signal-to-noise ratio of 1. It is given by

$$\Delta T_{\min} = \frac{T_{in} + T_{cRD}}{\sqrt{B \cdot \tau}} \quad (3)$$

where T_{in} is the available noise temperature of the noise source attached to the radiometer input, T_{cRD} is the effective input noise temperature of the radiometer, B is the limiting pre-detection system bandwidth, and τ is the integration time of the post-detection circuitry.

The effective input noise temperature of the radiometer has been experimentally shown to vary between 300 K and 800 K and is higher in the higher frequency bands. The limiting pre-detection system bandwidth B is set to 4 MHz by an 8-pole band-pass filter preceding the WBCO attenuator. The integration time of the post-detection circuitry τ is about 5 s. (The limiting post-detection frequency response, that of the strip-chart recorder, is $\approx$15 Hz, but the trace is visually integrated by the operator over 5 s or so.)

A typical system sensitivity, expressed in kelvins, for a DUT with noise temperature of 8400 K measured at 2 GHz, with T_{cRD} of $\approx$350 K, is 1.9 K. Under the same conditions, the system sensitivity for a cold load of (nominally) 77 K is 0.09 K.

3.3.3. Dynamic Range The dynamic range of the NCS1 is primarily determined by the WBCO attenuator. Based on the calibration data, the attenuator transfer function does not significantly depart from linearity between 20 dB and the highest calibrated value of 75 dB, for a dynamic range of at least 55 dB. However, the NCS1 dynamic range may be limited by active elements preceding the attenuator if driven into saturation, or the leakage of the signal. The verified dynamic range for the implemented radiometer is 15 dB. Additional tests would be needed to determine its full dynamic range.

3.3.4 Operation *External equipment needed:* A microwave generator having a stable, unmodulated output signal at +10 dBm is required to serve as a local oscillator. Liquid nitrogen and a barometer are needed for the operation of the NIST primary cryogenic standard. Access to a vector network analyzer is also necessary to evaluate the mismatches and asymmetries at the NCS1 input.

Front end characterization: Once measured, data on the reflection coefficients and the input switch efficiencies are stored in appropriate computer files and require only periodic checking. The frequency of the periodic checks depends on the calibration load, the previous wear of the input switch, and the extent of mechanical disturbances and ambient temperature variations incurred by the system since the previous check. A change in the real and imaginary parts of the reflection coefficients of the radiometer of $\approx$0.007 and a change in efficiencies of 0.1% require a new front end characterization. The software data update procedure is menu-driven.

Preparations for noise measurement: The reflection coefficient of the DUT must be measured before each calibration at all frequencies of interest. The NCS1 hardware, including the water circulator, should be turned on several hours ahead of the measurements in order for the system to reach thermal equilibrium. If the cryogenic standard is the nonambient standard, it must be filled with liquid nitrogen to the appropriate (marked) level. To prevent a possible damage due to freezing, water surrounding its output section must circulate at all times the standard is filled with liquid nitrogen. Manufacturer instructions guide a warm-up period for a DUT and a commercial nonambient standard, if such is used. After selecting the front end corresponding to the measurement frequency, the noise source with the lowest noise temperature (the cryogenic standard, if used with a hot DUT; the ambient standard if the secondary hot standard is substituted for the cryogenic standard) is switched into the input port and the WBCO attenuator adjusted to center the strip-chart trace. The input to the strip-chart recorder is momentarily grounded; no deflection of the center line verifies a true zero input signal.

Because of linearity, the lowest attenuator setting must not be below 20 dB.

The system resolution is checked as follows: the DUT is switched into the radiometer, and the trace brought back to the center by the appropriate attenuator adjustment. A stable baseline is established. The attenuator setting is changed by a small amount ΔA, typically 0.01 dB, causing the trace to deflect by a small amount Δd. The resolution can be adjusted by varying the gain of the post-detection operational amplifier (using a small decade counter on the front panel labeled "GAIN").

Measurement procedure: A full noise calibration consists of at least five measurement sets. Each set involves switching the nonambient standard, the

ambient standard, and the DUT into the system input, and adjusting the WBCO attenuator to maintain the trace on the strip chart centered. The software prompts the operator to input the attenuator dial setting. The resulting DUT noise temperature and associated statistical data are displayed on the monitor, allowing the operator to increase the number of measurements in a set if the standard deviation is unsatisfactorily large (greater than 25 K or so for a 9000 K device).

The system stability and general performance are checked by comparing the nonambient standard traces of each consecutive measurement set. A deflection from the previous position on the strip-chart indicates excessive drift (and should prompt a water circulator check), or some malfunction. The operator can direct the software to disregard the previous measurement set or to keep the set and increase the number of measurements.

The computer printout consists of a single sheet, showing the input data, the calculated noise temperature of the DUT, and the combined standard uncertainty and its components, as well as the expanded uncertainty (Table 1).

4. Discussion

The NCS1 has been designed to be an inexpensive system compatible with requirements of laboratories needing the highest achievable accuracy in thermal noise calibrations in the microwave part of the spectrum.

The radiometer is a total-power radiometer, as opposed to a switching (Dicke) radiometer [8,9]. The driving force behind the switching concept is drift. In the laboratory environment, because of the availability of inexpensive water cooling, the NCS1's sensitivity ($\approx$3 K), and the short time necessary to complete a measurement (minutes), drift is not a problem.

Similar to the switching, but unlike the other total-power radiometers at NIST [4], the NCS1 radiometer is a null-balanced instrument. Balancing is achieved in the IF section by a WBCO attenuator. Nulling occurs in the dc section by the operational amplifier circuit (Fig. 4).

Balancing allows the circuitry following the balancing device to be nonlinear, a major advantage. Tight linearity requirements are imposed on a balancing device, though. Based on a theoretical analysis and confirmed by calibration [10], the precision WBCO attenuator used in the system has a remarkably linear functional relationship between the coil separation and output power in a range of at least 55 dB.

The advantage of nulling is not only that the circuitry following the nulling device need not be linear, but also that its frequency response and thermal loading are immaterial [11]. Nulling speeds up the operations, since the strip-chart recorder that follows the nulling circuit in the NCS1 does not require settling time.

The commercial precision WBCO attenuator used in NCS1 is tuned to 30 MHz. The tuning circuit does not, however, provide sufficiently narrow and constant IF bandwidth, so a separate bandpass filter is required. This 4 MHz filter is the band-limiting element in the NCS1.

In practical terms, the commercial availability of a 30 MHz WBCO attenuator determines the IF frequency of the system. Since the uncertainty arising from the broadband mismatch increases rapidly with increasing IF frequency [1], a WBCO attenuator with a lower cutoff frequency is preferable.

A 30 MHz IF frequency also limits the expansion of the NCS1 frequency coverage of bands below approximately 250 MHz, since the frequency selectivity of the measurements would be compromised by the relatively wide 65 MHz averaging interval.

To expand the coverage to frequency bands above 12 GHz, a (secondary) noise standard must replace the NIST coaxial cryogenic standard, which cannot be used above that limit. New RF sections, each no more than an octave wide, would have to be integrated into the system. Frequency-sensitive uncertainties would increase, but there are no theoretical reasons limiting the upward frequency expansion. An alternative coaxial connector or a waveguide flange may be installed to replace the present precision Type N female connector. If the input switch is equipped with additional poles with appropriate connectors, the NCS1 can provide a calibration service in multiple connectors. Each path would need to have its efficiency determined. Care would have to be taken regarding the mechanical and thermal requirements of the input section; because of the broadband mismatch uncertainty the input section of the radiometer must be short, and at the ambient temperature.

The radiometer sensitivity could easily be improved by replacing the present RF amplifiers (noise figure 2.5 dB–4.5 dB, depending on the band), with low-noise amplifiers.

Because of nulling, the requirements on the output device of the NCS1 are low: stability over several minutes required for a measurement, and sufficient sensitivity and resolution. The strip-chart recorder can be replaced by a voltmeter or an A/D converter for on-line processing.

Table 1. A calibration report

Device: 12345
Test Number: 90346
Frequency: 3.0 GHz
Operator: RLB
Measurement Date: 04-30-1990
Time: 12:05:19

Comments: nonambient standard = NIST primary cryogenic coaxial standard

T_x	T_{ne}	Comb.Std. Uncert.	Expand Uncert.	T_x ENR	T_{ne} ENR	Expand. Uncert.
K	K	K	K	dB	dB	dB
8368	8353	±60	±120	14.45	14.44	±.06

Sources of Uncertainty:	u_c
Non-ambient Standard	0.82 %
Ambient Standard	0.10 %
Connector	0.07 %
Mismatch Factor	0.01 %
Switch Asymmetry	0.13 %
Isolator	0.04 %
Broadband Mismatch	0.10 %
Attenuator	0.06 %
Random Effects	0.01 %
Combined Standard Uncertainty	0.72 %
EXPANDED UNCERTAINTY (k=2)	1.44 %

Input (Measurement) Data

M_{na}: 0.996
M_x: 0.995
Γ_{Rna}: (+0.055)+i(-0.009)
Γ_{Rx}: (+0.056)+i(-0.008)
Γ_{na}: (+0.010)+i(+0.054)
Γ_x: (-0.001)+i(+0.043)
Asymm:0.9981

T_a: 297.4 K
T_{na}: 84.0 K
T_{eR}: 284 K
Bprss:625.0 mmHg

Attenuator settings (dB)

Nonambient Standard	Ambient Standard	DUT
21.500	23.480	35.202
21.500	23.479	35.202
21.500	23.481	35.201
21.500	23.480	35.199
21.500	23.479	35.200

Acknowledgment

The author gratefully acknowledges the support of the following individuals and organizations: William C. Daywitt, for invaluable insights, discussions and encouragement; Robert L. Billinger, for creative contributions to the system's design, implementation and check-out; Rohde Wakefield, for writing the excellent software; David F. Wait, for support during the project's long development phase, and for performing the system check-out; Edward Andrusko, George J. Counas, Richard L. Ehret, George M. Free, John R. Juroshek, William A. Kissick, Galen H. Koepke, Neil T. Larsen, Dean G. Melquist and Keith C. Roe, for giving much appreciated advice, lending and sometimes donating parts, providing laboratory space, and performing demanding measurements; and the Calibration Coordination Group of the Defense Department and Norman J. Leck in particular, for continuous support.

5. References

[1] S. P. Pucic, Evaluation of uncertainties of the null-balanced total radiometer system NCS1, J. Res. Natl. Inst. Stand. Technol. **99**, 65 (1994).

[2] W. C. Daywitt, A coaxial noise standard for the 1 GHz to 12.4 GHz frequency range, Natl. Bur. Stand. (U.S.) Tech. Note 1074 (1984).

[3] S. P. Pucic, Derivation of the system equation for the NCS1, a new null-balanced total radiometer system, J. Res. Natl. Inst. Stand. Technol. **99**, 35 (1994).

[4] W. C. Daywitt, Radiometer equation and analysis of systematic errors for the NIST automated radiometers, Natl. Inst. Stand. Technol. Tech. Note 1327 (1989).

[5] S. Perera, Broadband Mismatch Error in Noise Measurement Systems, CPEM Digest (1992).

[6] D. F. Wait, The sensitivity of the Dicke radiometer, J. Res. Natl. Bur. Stand. (U.S.) **71C**, 127–157 (1967).

[7] J. D. Kraus, Radio Astronomy, 2nd edition, Cygnus-Quasar Books, (1986) pp. 7.1–7.7.

[8] C. K. S. Miller, W. C. Daywitt, M. G. Arthur, Noise standards, measurements, and receiver noise definitions, Proc. IEEE **55**, 865–877 (1967).

[9] J. S. Wells, W. C. Daywitt, and C. K. S. Miller, Measurement of effective temperatures of microwave noise sources, IEEE Tran. Instr. Meas. **13**, 17–28 (1964).

[10] R. T. Adair and D. H. Russell, A calibration service for 30 MHz attenuation and phase shift, Natl. Bur. Stand. (U.S.) Spec. Publ. 250-32 (1988).

[11] P. K. Stein, Measurement Engineering, 3rd ed., Vol. I, pp.71, Stein Engineering Services, Inc. (1964).

About the author: *Sunchana P. Pucic is an electronics engineer in the Microwave Metrology Group of the Electromagnetic Fields Division at NIST. The National Institute of Standards and Technology is an agency of the Technology Administration, U.S. Department of Commerce.*

Volume 99, Number 1, January–February 1994
Journal of Research of the National Institute of Standards and Technology

[J. Res. Natl. Inst. Stand. Technol. 99, 55 (1994)]

Derivation of the System Equation for Null-Balanced Total-Power Radiometer System NCS1

Volume 99 | Number 1 | January–February 1994

Sunchana P. Pucic

National Institute of Standards and Technology,
Boulder, CO 80303-3328

A system equation of a recently developed null-balanced, total-power radiometer system is rigorously derived. Delivered noise power and temperature is related to available power (temperature) through an extension of the mismatch factor to broadband systems. The available power ratio α_g, the available gain G_g, and the delivered power ratio (efficiency) η_l are defined. Properties of idealized, but in principle realizable components such as an infinitely directive isolator and a lossless matched waveguide-below-cutoff attenuator are used. A cascading technique is repeatedly applied to the fundamental noise equation. Mathematically modeling the experimental procedure of sequentially attaching the two noise standards and the unknown source to the system input, we obtain the system of three equations that can be solved for the noise temperature of the unknown noise source.

Key words: broadband; calibration; noise power; noise temperature; null-balanced; system equation; total power radiometer section.

Accepted: October 12, 1993

1. Introduction

The system equation of a recently developed Noise Calibration System Model 1 (NCS1) is rigorously derived in this article. The NCS1, recently built at the National Institute of Standards and Technology, is used to measure thermal noise from coaxial noise sources. It consists of two noise standards and a null-balanced, total-power radiometer. The radiometer downconverts the amplified RF noise signal to a 30 MHz IF frequency. A precision waveguide-below-cutoff (WBCO) attenuator is used to achieve a balanced operations mode. An unbased square law diode serves as a detector. Nulling and resolution control are implemented at the post-detection, DC stage. The system is described in more detail in the accompanying articles [1] and [2].

The noise power available from a noise source and measured by the NCS1 is calculated according to the system equation. This article presents a rigorous derivation of that equation. Initially, the equation is derived for an idealized, simplified system (the simplified equation). Modifications of the simplified system needed to actually implement the NCS1, and the resulting modifications of the simplified system equation, are described later. Deviations from ideal behavior are treated in [2].

2. Derivation of the Simplified System Equation

2.1 Basic Considerations

Several topics are briefly reviewed, in preparation for a derivation of the system equation.

2.1.1 Symbols In the following text, terms a noise source and a noise generator are used interchangeably; the subscript g designates a general, unspecific origin of the noise signal (e.g., P_g). The specific noise sources are identified with subscripts s for a noise standard (e.g., P_s) and x for the

unknown (e.g., P_x). Terms the unknown noise source and the DUT (the device under test) are used interchangeably. The subscript a stands for the ambient temperature (as in P_a).

Capital letter subscripts designate parts of the radiometer. The capital A stands for the attenuator, G for the amplifier, I for the isolator, and SW for the input switch.

For reflection coefficients within the radiometer, $\vec{\Gamma}$ signifies a reflection coefficient looking backward, in the direction opposite to the net power flow.

The subscript i in many of the quantities signifies that quantity's dependency on the existing input conditions. Initially, i stands for 1, 2, or x, that is, the conditions of having the noise standard 1, the noise standard 2, or the unknown noise source x attached to the input. Later on, i stands for s, a, or x, that is, the conditions of having the nonambient noise standard, the ambient noise standard, or the unknown noise source x attached to the input.

2.1.2 The Measurement Quantity The quantity measured by the NCS1 is the electromagnetic noise power P, in watts; however, it is the noise temperature T, in kelvins (K), that is customarily reported. Neglecting quantum effects, the two quantities are proportional to each other according to the well known relationship

$$P = kBT, \tag{1}$$

where k is the Boltzmann constant $= 1.38 \cdot 10^{-23}$ J/K, and B is the system noise bandwidth in hertz.

The quantities P and T are the *available* noise power and the *available* temperature: the power or temperature that would be delivered by a source to a load, such as a power meter, under the ideal conditions of a complex conjugate match.

In contrast, the *delivered* power P_{del} (or temperature T_{del}) is the power (temperature) that is actually delivered to a (generally mismatched) load.

2.1.3 The Mismatch Factor The available and the delivered powers (temperatures) are related by

$$P_{del} = MP, \tag{2}$$

and

$$T_{del} = MT, \tag{3}$$

where M is the mismatch factor, a real number between 0 (total mismatch), and 1 (perfect match). The mismatch factor is a function of the reflection coefficients of the source and the load. Power delivered to a load from sources having the same available power, but different reflection coefficients, is therefore variable and dependent on the input conditions.

In broadband systems of bandwidth B, the mismatch factor, if used as in Eqs. (2) and (3) is strictly defined as

$$M = \int_B M(f) g \mathrm{d}f, \tag{4}$$

where g is the transfer function of the radiometer, and f is the frequency.

In principle, the mismatch factor can be evaluated according to Eq. (4). However, as long as the elements constituting M do not change appreciably across the measurement band, the use of a constant mismatch factor evaluated conveniently at mid-band produces negligible errors. Proper engineering design must assure a compliance with Eq. (4) and the error analysis must evaluate a deviation from the ideal conditions [3,4].

2.1.4 Passive Two-Ports If a noise generator with the available noise temperature T_g is connected to the input of a *passive*, linear two-port held at the temperature T, the available temperature T_{out} at the output of the two-port can be calculated from fundamental thermodynamic principles. It is given by [5, 3] by

$$T_{out} = T_g \alpha_g + T(1 - \alpha_g). \tag{5}$$

The quantity α_g is a ratio of the available power at the output of the two-port to the available power at the input of the two-port: $\alpha_g \equiv P_{out}/P_{in}$. The quantity α_g is an *in situ* quantity: it depends not only on the parameters of the two-port, but also on those of the two-port's environment [5]. Specifically, it depends on the reflection coefficient looking into the network preceding the two-port, that is, the (possibly equivalent in a Thevenin sense) generator. This dependence on the input conditions is indicated by the subscript g. The quantity α_g characterizes the lossiness of the two-port and has a value between 0 (an infinitely lossy two-port) and 1 (a lossless two-port). A full definition of α_g, applied to the specific passive two-port within its environment, is given in Sec. 2.3.

The first term $T_g \alpha_g$ in Eq. (5) describes how the input noise signal is modified by a passage through the two-port. The second term $T(1-\alpha_g)$ describes the noise contribution of the two-port itself.

2.1.5 Active Two-Ports If a noise source with the available noise temperature T_g is connected to

the input of an *active* linear two-port such as an amplifier, the available temperature T_{out} at the output of the two-port is given by

$$T_{out} = G_g (T_g + T_{eg}). \quad (6)$$

The quantity G_g is the available gain of the active two-port. Similar to α_g, it is a ratio of the available power at the output of the two-port to the available power at the input of the two-port, $G_g \equiv P_{out}/P_{in}$. As an *in situ* quantity, it is dependent on the input conditions, as emphasized by the subscript g. A full definition, applied to the specific active two-port within its environment, is given in Sec. 2.3.

The quantity T_{eg} in Eq. (6) accounts for the noise contribution of the active two-port, a function of the circuit design and only marginally dependent on the physical temperature. The noise that is generated by the active two-port and is available at its output, is referred to its input as the *effective input noise temperature* T_{eg}. The subscript g emphasizes its dependency on the reflective properties of the (possibly equivalent) generator (Sec. 2.3).

2.1.6 A Cascade From the definitions of α and G it follows that for a cascaded chain of n elements, the overall $\alpha_{casc} = \alpha_1 \alpha_2 \ldots \alpha_n$, and $G_{casc} = G_1 G_2 \ldots G_n$.

2.2 Basic Assumptions

The derivation of the system equation is based on repeated applications of Eqs. (5) and (6) to the elements of the cascaded chain of the radiometer. The conditions assumed to hold are:

- Steady state
- Single-mode propagation in the transmission lines
- Lossless transmission lines and ideal connectors
- Linear elements throughout, except for the square-law power detector
- Broadband components across the bandwidth B
- Thermal noise (i.e., noise having a Gaussian amplitude distribution and a flat power spectrum across the noise bandwidth B) generated by the noise sources
- All passive components in the radiometer at the ambient temperature T_a
- A linear WBCO attenuator in its dial settings.

2.3 The Simplified Radiometer System

For the purpose of deriving the system equation, the radiometer is reduced to essential components: an isolator, an RF amplifier, a WBCO attenuator with its matching pads (Sec. 2.3.2 and [6]), and a receiver containing a square law detector (Fig. 1). The lossiness of the input section of the radiometer is combined with the lossiness of the isolator. The isolator itself is initially treated as a simple lossy, reciprocal two-port, and later (Sec. 2.3.2) it assumes the nonreciprocal properties. The amplifier is the element assumed to define the system bandwidth.

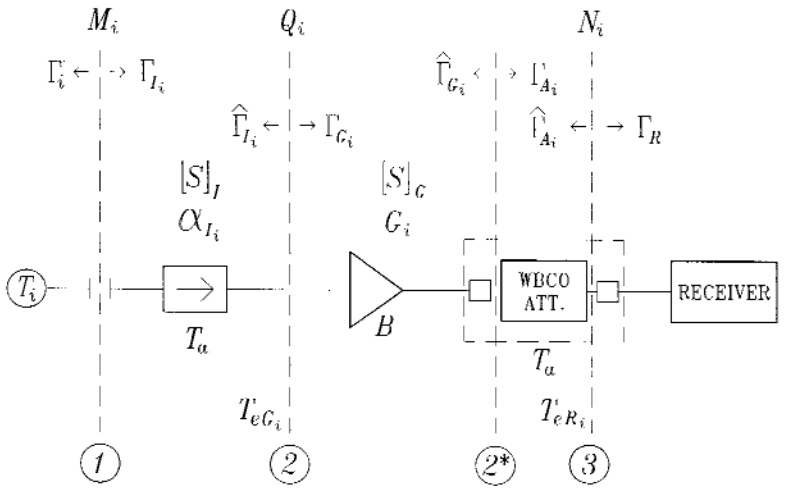

Fig. 1. Simplified system block diagram.

The two noise standards are characterized by their available noise temperatures T_1 and T_2 and their reflection coefficients Γ_1 and Γ_2. The DUT has a known (measured) reflection coefficient Γ_x. Its available temperature is the quantity under test.

The radiometer input signal is the broadband noise generated by the three noise sources: the two noise standards and the DUT. The three sources are sequentially attached to the radiometer input port and the noise power is adjusted by the attenuator so that the receiver measures the same power in all three cases.

The radiometer reflection coefficient (at the input plane 1 in Fig. 1) is Γ_{I_i}. In general, it varies with the attenuator setting, since it depends on the (variable) Γ_{A_i}, according to [7]:

$$\Gamma_{I_i} = S_{11_I} + \frac{S_{12_I} S_{21_I} \Gamma_{G_i}}{1 - S_{22_I} \Gamma_{G_i}}, \tag{7}$$

while the term Γ_{G_i} is, in turn, given by

$$\Gamma_{G_i} = S_{11_G} + \frac{S_{12_G} S_{21_G} \Gamma_{A_i}}{1 - S_{22_G} \Gamma_{A_i}}. \tag{8}$$

In the preceding two equations, the S-parameters $[S]_I$ characterize the isolator, while $[S]_G$ pertain to a cascade of the amplifier and the left-sided matching pad of the WBCO attenuator.

The effective input noise temperature of the amplifier T_{eG_i} varies with the input conditions. The effective input noise temperature of the receiver T_{eR_i} varies with both the input conditions and the attenuator settings.

2.3.1 Equations Modeling the Measurement Procedure The measurement procedure consists of attaching the two noise standards and the DUT to the radiometer input port in sequence, and adjusting the attenuator settings until a balanced condition is achieved.

With the first noise standard (with available noise power kBT_1 and reflection coefficient Γ_1) attached to the radiometer input, the receiver detects a certain amount of delivered power P_{del}:

$$kB\{[T_1\alpha_{I_1} + T_a(1-\alpha_{I_1}) + T_{eG_1}]G_1 \cdot \alpha_{A_1} + T_a(1-\alpha_{A_1}) + T_{eR_1}\} \cdot N_1 = P_{del}. \tag{9}$$

The term G_1 (and likewise G_2 and G_x in the following equations) refers to the available gain of the amplifier/left-matching-pad cascade (Sec. 2.1.6).

As the second noise standard (with available noise power kBT_2 and reflection coefficient Γ_2) is attached to the radiometer input, the attenuator is adjusted so that the receiver detects *the same* delivered power P_{del} as previously:

$$kB\{[T_2\alpha_{I_2} + T_a(1-\alpha_{I_2}) + T_{eG_2}]G_2 \cdot \alpha_{A_2} + T_a(1-\alpha_{A_2}) + T_{eR_2}\} \cdot N_2 = P_{del}. \tag{10}$$

Finally, as the DUT (with available noise power kBT_x and reflection coefficient Γ_x) is attached to the radiometer input, the attenuator is again adjusted so that the receiver detects the same delivered power P_{del} as in the previous two cases:

$$kB\{[T_x\alpha_{I_x} + T_a(1-\alpha_{I_x}) + T_{eG_x}]G_x \cdot \alpha_{A_x} + T_a(1-\alpha_{A_x}) + T_{eR_x}\} \cdot N_x = P_{del}, \tag{11}$$

where k is the Boltzmann constant, B is the limiting system bandwidth, T_i $(i = 1,2,x)$ is the available noise temperature of the noise sources attached to the input, and α_{I_i} and α_{A_i} are the available power ratios (Sec. 2.1), *in situ* quantities. They are defined for the specific passive two-ports *within* their respective environments [5], as

$$\alpha_{I_i} = \frac{(1-|\Gamma_i|^2) \cdot |S_{21_I}|^2}{(1-|\bar{\Gamma}_{I_i}|^2)|1-S_{11_I}\Gamma_i|^2} \tag{12}$$

for the isolator, and

$$\alpha_{A_i} = \frac{(1-|\bar{\Gamma}_{G_i}|^2) \cdot |S_{21_{A_i}}|^2}{(1-|\bar{\Gamma}_{A_i}|^2)|1-S_{11_{A_i}}\bar{\Gamma}_{G_i}|^2} \tag{13}$$

for the attenuator.

In Eqs. (12) and (13) S_{21_I}, S_{11_I} and $S_{21_{A_i}}$, $S_{11_{A_i}}$ are the S-parameters of the isolator and the attenuator. The S-parameters of the attenuator vary with the attenuator setting.

The terms Γ_i, $\bar{\Gamma}_{I_i}$, $\bar{\Gamma}_{G_i}$, and $\bar{\Gamma}_{A_i}$ in the same equations are the reflection coefficients shown in Fig. 1. The fact that α_{I_i} and α_{A_i} have reflection coefficients looking either directly into the sources (Γ_i), or indirectly into the sources through one or more two-ports ($\bar{\Gamma}_{I_i}$, $\bar{\Gamma}_{G_i}$, or $\bar{\Gamma}_{A_i}$), explicitly shows their dependency on the input conditions.

T_{eG_i} and T_{eR_i} are the effective input noise temperatures, in kelvins, of the amplifier and the receiver. The effective input noise temperature T_{eG_i} of the RF amplifier depends on the input conditions, i.e., on the reflection coefficients of the three noise sources Γ_i. The effective input noise temperature of the receiver T_{eR_i} depends on the reflection coefficients of the three noise sources, as well as on the

reflection coefficient looking backward into the attenuator at its three different settings $\hat{\Gamma}_{A_i}$.

The available gain of the amplifier/left-matching-pad combination G_i, *in situ* quantity, is given by

$$G_i = \frac{(1-|\hat{\Gamma}_{I_i}|^2)\cdot|S_{21_G}|^2}{(1-|\hat{\Gamma}_{G_i}|^2)|1-S_{11_G}\hat{\Gamma}_{I_i}|^2} \tag{14}$$

The terms $\hat{\Gamma}_{I_i}$ and $\hat{\Gamma}_{G_i}$ in Eq. (14) explicitly show the dependency of the available gain G_i on the input conditions. In the case of $\hat{\Gamma}_{I_i}$, this dependency is direct:

$$\hat{\Gamma}_{I_i} = S_{22_I} + \frac{S_{12_I}S_{21_I}\Gamma_i}{1-S_{11_I}\Gamma_i}. \tag{15}$$

In the case of $\hat{\Gamma}_{G_i}$, the dependency is indirect, through the $\hat{\Gamma}_{I_i}$ dependency on the input conditions:

$$\hat{\Gamma}_{G_i} = S_{22_G} + \frac{S_{12_G}S_{21_G}\hat{\Gamma}_{I_i}}{1-S_{11_G}\hat{\Gamma}_{I_i}}. \tag{16}$$

A mismatch factor N_i is defined at the plane 3 in Fig. 1 as

$$N_i = \frac{(1-|\hat{\Gamma}_{A_i}|^2)(1-|\Gamma_R|^2)}{|1-\hat{\Gamma}_{A_i}\Gamma_R|^2}, \tag{17}$$

where Γ_R is the reflection coefficient looking into the receiver, and $\hat{\Gamma}_{A_i}$ is the reflection coefficient-looking backward into the attenuator, defined as

$$\hat{\Gamma}_{A_i} = S_{22_{A_i}} + \frac{S_{12_{A_i}}S_{21_{A_i}}\hat{\Gamma}_{G_i}}{1-S_{11_{A_i}}\hat{\Gamma}_{G_i}}. \tag{18}$$

2.3.2 Idealized Elements Assumptions Equations (9)–(11) simplify considerably under the following assumptions:

- Infinitely directive ($S_{12_I}=0$), but not necessarily lossless or matched isolator
- Large gain preceding the attenuator
- Lossless WBCO attenuator ($\alpha_{A_i}=1$)

The first assumption results in the following simplifications:

$\Gamma_{I_i} = \Gamma_I(=S_{11_I})$; $\hat{\Gamma}_{I_i} = \hat{\Gamma}_I(=S_{22_I})$; and $\hat{\Gamma}_{G_i} = \hat{\Gamma}_G(=S_{22_G})$

$G_i = G$

$T_{eG_i} = T_{eG}$; $T_{eR_i} \neq f\{\Gamma_i\}$.

Because of the second assumption, the temperature of the input noise signal, once it reaches the input of the receiver, is much higher than the receiver effective input noise temperature T_{eR_i}. Consequently, the *variability* of the receiver effective input noise temperature, due to changes in the reflection coefficient of the receiver equivalent source $\hat{\Gamma}_{A_i}$ (which in turn are related to different attenuator settings), becomes negligible: T_{eR_i} becomes the constant T_{eR}.

The implications of the third assumption are discussed next. An ideal WBCO attenuator is inherently a lossless device, because the attenuation is achieved by the input signal propagating under the below-cutoff conditions. The input signal is therefore partially reflected and partially transmitted; no component of the input signal is absorbed, so there are no losses. (Small losses within the imperfect metal walls of the implemented attenuator can be neglected in this derivation.) The term α_{A_i} becomes 1, and consequently its noise contribution $T_a(1-\alpha_{A_i})$ vanishes.

The concept of attenuation is valid only in a nonreflecting environment [7]. The WBCO attenuator has a pair of (lossy) matching pads that are placed at the input and output ports to fulfill the requirement. The two reference planes (planes 2* and 3 in Fig. 1) are positioned between the WBCO attenuator proper and the matching pads, assuring a good bilateral match, while maintaining the lossless character of the WBCO attenuator proper.

The mismatch factor N_i depends on Γ_R and $\hat{\Gamma}_{A_i}$ [Eq. (17)]. The attenuator padding assures $\Gamma_R = \hat{\Gamma}_G \approx 0$. The condition $\Gamma_R = 0$ reduces the expression for the mismatch factor N_i to $(1-|\hat{\Gamma}_{A_i}|^2)$. Under the assumption that $\Gamma_G = 0$, the expression for $\hat{\Gamma}_{A_i}$, in turn, reduces to $S_{22_{A_i}}$. The WBCO attenuator, postulated to be a lossless device, must satisfy the losslessness condition $|S_{22_{A_i}}|^2 = (1-|S_{21_{A_i}}|^2)$ [7]. Under the assumptions that the attenuator is lossless and matched, the expression for the mismatch factor N_i is drastically simplified to $N_i = |S_{21_{A_i}}|^2$.

With all of the above simplifications in mind, the initial set of three Eqs. (9)–(11) now become

$$kB\{[T_1\alpha_{I_1} + T_a(1-\alpha_{I_1}) + T_{eG}]\,G + T_{eR}\}|\,S_{21_{A_1}}|^2 = P_{del}, \tag{19}$$

$$kB\{[T_2\alpha_{I_2} + T_a(1-\alpha_{I_2}) + T_{eG}]\,G + T_{eR}\}|\,S_{21_{A_2}}|^2 = P_{del}, \tag{20}$$

$$kB\{[T_x\alpha_{I_x} + T_a(1-\alpha_{I_x}) + T_{eG}]\,G + T_{eR}\}|\,S_{21_{A_x}}|^2 = P_{del}. \tag{21}$$

It is advantageous to implement the system in such a manner that the temperature of one of the two standards is set at the ambient temperature T_a (e.g., setting $T_2 = T_a$ in the second standard in the previous equations). Equation (20) then simplifies to

$$kB\{[T_a + T_{eG}]G + T_{eR}\}|S_{21_{A_a}}|^2 = P_{del}. \quad (22)$$

For readability, the temperature of the first standard T_{s_1}, is now relabeled T_s. In the implemented system, this standard is at the cryogenic temperature. By dividing Eqs. (19) and (21) by Eq. (22), canceling the common terms, and rearranging, we obtain:

$$\alpha_{I_s}(T_s - T_a)|S_{21_{A_s}}|^2 = (T_a + T_e)(|S_{21_{A_a}}|^2 - |S_{21_{A_a}}|^2) \quad (23)$$

$$\alpha_{I_x}(T_x - T_a)|S_{21_{A_x}}|^2 = (T_a + T_e)(|S_{21_{A_a}}|^2 - |S_{21_{A_x}}|^2), \quad (24)$$

where T_e stands for $(T_{eG} + T_{eR}/G)$, a simple additive constant which drops out of the system of equations in the next step.

Equations (23) and (24) combine into

$$\frac{T_x - T_a}{T_s - T_a} = \frac{\alpha_{I_s}}{\alpha_{I_x}} \cdot \frac{|S_{21_{A_s}}|^2}{|S_{21_{A_x}}|^2} \cdot \frac{|S_{21_{A_a}}|^2 - |S_{21_{A_x}}|^2}{|S_{21_{A_a}}|^2 - |S_{21_{A_s}}|^2}. \quad (25)$$

A mismatch factor M_i $(i = s, x)$, shown in Fig. 1, is defined as

$$M_i = \frac{(1 - |\Gamma_i|^2)(1 - |\Gamma_I|^2)}{|1 - \Gamma_i^* \Gamma_I|^2}. \quad (26)$$

The ratio $\alpha_{I_s}/\alpha_{I_x}$ for an isolator with infinite isolation $(S_{12_I} = 0)$ reduces to a ratio of the mismatch factors at the isolator input, M_s/M_x.

The unknown temperature T_x of the DUT can, then, be calculated from

$$T_x = T_a + \frac{M_s}{M_x}(T_s - T_a)\frac{(|S_{21_{A_a}}|^2/|S_{21_{A_x}}|^2) - 1}{(|S_{21_{A_a}}|^2/|S_{21_{A_s}}|^2) - 1}. \quad (27)$$

By expressing $|S_{21_{A_i}}|^2$ in terms of the attenuator dial settings, in decibels, we obtain the resulting *simplified system equation:*

$$T_x = T_a + \frac{M_s}{M_x}(T_s - T_a)\frac{10^{-(A_a - A_x)/10} - 1}{10^{-(A_a - A_s)/10} - 1}. \quad (28)$$

The WBCO attenuator needs to be calibrated in order to verify that its output is indeed linear with the dial setting.

Under the set of assumptions stated above, the available temperature of the DUT can be determined by knowing the available noise temperatures of the two standards T_s and T_a; by determining the mismatch ratio M_s/M_x [(from a vector network analyzer measurements of the appropriate reflection coefficients, Eq. (26)]; and by reading the three attenuator dial settings A_s, A_a, and A_x.

2.3.3 Alternative Expressions Equation (28) may also be written using the Y-factor notation as

$$T_x = T_a + \frac{M_s}{M_x}(T_s - T_a)\frac{Y_x - 1}{Y_s - 1} \quad (29)$$

where Y_x and T_s are defined in an obvious way from Eq. (28). The measured noise temperature of a hot DUT can be expressed in terms of the excess noise ratio (ENR), in decibels, as

$$ENR = 10 \log \frac{T_x - T_0}{T_0}, \quad (30)$$

where T_0 is standardized to 290 K, somewhat less than room temperature. The ENR pertains to noise in excess of 290 K (the hot noise sources); sources with temperatures below 290 K (such as cryogenic sources) cannot be characterized by it.

3. The NIST Noise Calibration System Model 1 (NCS1)

A block diagram of the Noise Calibration System Model 1 is shown in Fig. 2. The implemented radiometer differs from the idealized radiometer (Sec. 2) as follows:

- A single-pole, triple-throw coaxial switch is placed at the system input. The presence of this input switch creates three separate system input ports, with three different paths leading to the rest of the radiometer. The paths are modeled as passive linear two-ports [3] in cascade with the rest of the radiometer. Their presence results in the *asymmetry* correction to the simplified system equation.
- Heterodyning is implemented. Both sidebands are used, resulting in the measured noise signal power being the *mean* of the powers contained in the two symmetrical bands centered around the local oscillator (LO) frequency. Assuming ideal behavior, the heterodyning process is transparent to the system equation derivation and its applicability.

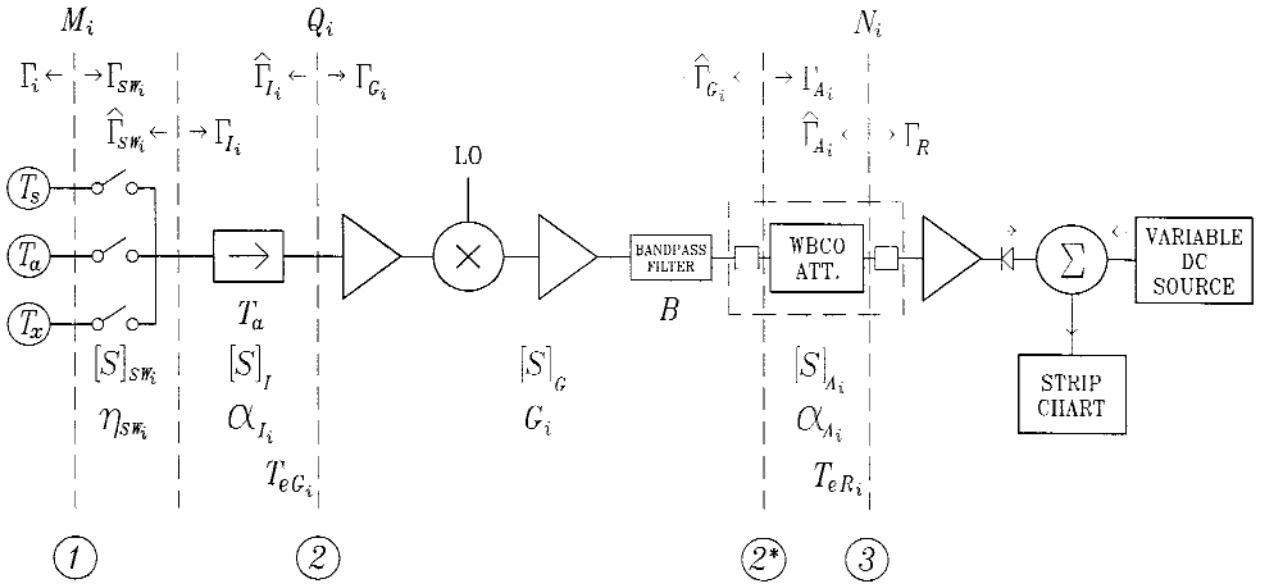

Fig. 2. NCS1 block diagram.

- Nulling circuitry is included in the post-detection (dc) stage of the receiver to implement a fully null-balanced system.

3.1 System Equation

By modeling the input switch paths as three different two-ports (at the ambient temperature) preceding the isolator (Fig. 3), taking into account the assumptions in Sec. 2.3.2, and applying the cascading formulas from Sec. 2.1.6, we can rewrite the three equations describing the measurement procedure [Eqs. (19), (20), and (21)] as

$$kB\{[[T_1\alpha_{SW_1}+T_a(1-\alpha_{SW_1})]\alpha_{l_1}+T_a(1-\alpha_{l_1})+ T_{eG}]\,G+T_{eR}\}|S_{21_{A_1}}|^2=P_{del}\,, \tag{31}$$

$$kB\{[[T_2\alpha_{SW_2}+T_a(1-\alpha_{SW_2})]\alpha_{l_2}+T_a(1-\alpha_{l_2})+ T_{eG}]\,G+T_{eR}\}|S_{21_{A_2}}|^2=P_{del}\,, \tag{32}$$

and

$$kB\{[[T_x\alpha_{SW_x}+T_a(1-\alpha_{SW_x})]\alpha_{l_x}+T_a(1-\alpha_{l_x})+ T_{eG}]\,G+T_{eR}\}|S_{21_{A_x}}|^2=P_{del}\,, \tag{33}$$

where α_{SW_i}, $i=1, 2, x$ describes the lossiness of the paths through the input switch.

By grouping terms together, we easily reduce the above equations to

$$kB\{[T_1\alpha_{l_1}+T_a(1-\alpha_{l_1})+T_{eG}]\,G+T_{eR}\}$$

$$|S_{21_{A_1}}|^2=P_{del}, \tag{34}$$

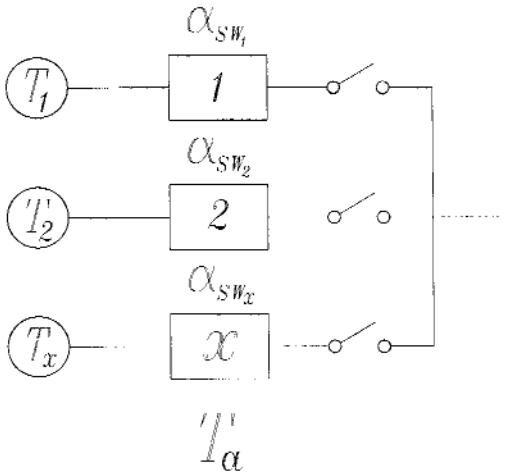

Fig. 3. Input switch.

$$kB\{[T_2\alpha_2 + T_a(1-\alpha_2) + T_{eG}]\,G + T_{eR}\}$$

$$|S_{21_{A_2}}|^2 = P_{del}, \tag{35}$$

and

$$kB\{[T_x\alpha_x + T_a(1-\alpha_x) + T_{eG}]\,G + T_{eR}\}$$

$$|S_{21_{A_x}}|^2 = P_{del}, \tag{36}$$

where α_i, $i = 1, 2, x$ describes the available power ratio of the combined switch/isolator two-port,

$$\alpha_i = \alpha_{SW_i}\,\alpha_{1_i} \tag{37}$$

Equations (34)–(36) have the same form as Eqs. (19)–(21) describing the simplified radiometer, Sec. 2.3.2, and can be rewritten by simply following the previous derivation as

$$\frac{T_x - T_a}{T_s - T_a} = \frac{\alpha_s}{\alpha_x} \cdot \frac{|S_{21_{A_x}}|^2}{|S_{21_{A_x}}|^2} \cdot \frac{|S_{21_{A_a}}|^2 - |S_{21_{A_r}}|^2}{|S_{21_{A_a}}|^2 - |S_{21_{A_s}}|^2}. \tag{38}$$

3.2 Switch Efficiency

One can define another quantity, a *delivered power ratio*, $\eta_l \equiv P_{del_{out}}/P_{del_{in}}$, which describes the lossiness of a linear two-port. The quantity η_l has a character of an ordinary efficiency. The subscript l signifies its dependence on the load, since, analogously to α_g, it is an *in situ* quantity.

For the input switch in Fig. 3 the efficiencies of each path are defined as

$$\eta_{SW_i} = \frac{(1-|\Gamma_l|^2)\cdot|S_{21_{SW_i}}|^2}{(1-|\Gamma_{SW_i}|^2)|1-S_{22_{SW_i}}\Gamma_l|^2}, \tag{39}$$

where $S_{21_{SW_i}}$ and $S_{22_{SW_i}}$ refer to the S-parameters of the different paths through the input switch, and Γ_l and Γ_{SW_i} are the reflection coefficients.

Referring to Fig. 4, we have a simple expression relating an α_g to an η_l [5]:

$$\alpha_g M_2 = \eta_l M_1, \tag{40}$$

where M_1 and M_2 are the two mismatch factors bracketing the two-port.

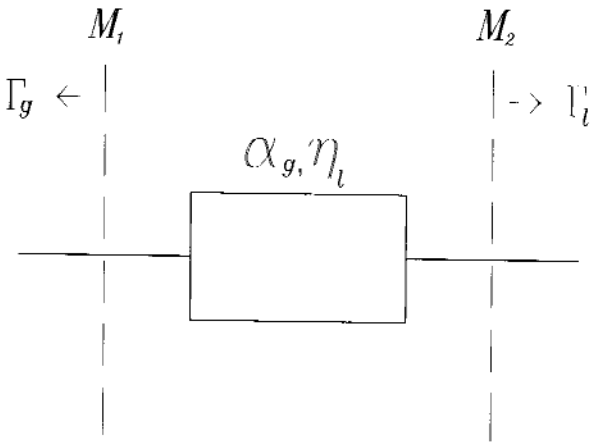

Fig. 4. A two-port.

Applying Eq. (40) to the ratio α_x/α_s, we can show that the simplified system Eq. (28) becomes

$$T_x = T_a + \frac{M_s}{M_x} \cdot \frac{\eta_{SW_s}}{\eta_{SW_x}} (T_s - T_a) \frac{10^{-(A_a - A_x)/10} - 1}{10^{-(A_a - A_s)/10} - 1}. \tag{41}$$

Equation (41), the full-fledged system equation, is used by the NCS1 software to calculate the noise temperature of the noise source under calibration.

4. Conclusion

The system equation for the new null-balanced, total-power radiometer is derived interactively with the system design. The result is a well-characterized noise calibration instrument with a complete mathematical model. A rigorous derivation of the system equation facilitates a rigorous analysis of uncertainties, which in turn forms the foundation for accurate measurements.

Acknowledgment

The author would like to thank William C. Daywitt and David F. Wait for their generous help and many useful discussions, and the Calibration Coordination Group of the Department of Defense for their support.

5. References

[1] S. P. Pucic, A null-balanced total-power radiometer system NCS1, J. Res. Natl. Inst. Stand. Technol. **98**, 45 (1994).
[2] S. P. Pucic, Evaluation of uncertainties of the null-balanced total-power radiometer system NCS1, J. Res. Natl. Inst. Stand. Technol. **98**, 65 (1994).
[3] W. C. Daywitt, Radiometer equation and analysis of systematic errors for the NIST automated radiometers, NIST Technical Note 1327 (1989).
[4] S. Perera, Broadband Mismatch Error in Noise Measurement Systems, CPEM Digest (1992).
[5] C. K. S. Miller, W. C. Daywitt, M. G. Arthur, Noise standards, measurements, and receiver noise definitions, Proc. IEEE **55**, 865–877 (1967).
[6] B. O. Weinschel and G. U. Sorger, Waveguide below cutoff attenuation standard, Internal report 90-95R, Weinschel Engineering (1964).
[7] D. M. Kerns and R. W. Beatty, Basic theory of waveguide junctions and introductory microwave network analysis, Pergamon Press (1967).

About the author: *Sunchana P. Pucic is an electronics engineer in the Microwave Metrology Group of the Electromagnetic Fields Division at NIST. The National Institute of Standards and Technology is an agency of the Technology Administration, U.S. Department of Commerce.*

Volume 99, Number 1, January–February 1994
Journal of Research of the National Institute of Standards and Technology

[J. Res. Natl. Inst. Stand. Technol. 99, 65 (1994)]

Evaluation of Uncertainties of the Null-Balanced Total-Power Radiometer System NCS1

Volume 99 | Number 1 | January–February 1994

Sunchana P. Pucic

National Institute of Standards and Technology,
Boulder, CO 80303-3328

Standard uncertainties are evaluated for the null-balanced, total-power, heterodyned radiometer system with a switched input that was recently developed at NIST to calibrate thermal noise sources. Eight significant sources of uncertainty due to systematic effects are identified, two attributable to the two noise standards, and one each to connectors, the input mismatch, the input switch asymmetry, the isolator, the broadband mismatch and the attenuator. The combined standard uncertainty of a typical coaxial noise source calibration at a representative frequency of 2 GHz is about 1%. A strategy for reducing uncertainties is discussed.

Key words: calibration; coverage factor; noise temperature; null-balanced; systematic effects; random effects; thermal noise; total power radiometer; uncertainty analysis.

Accepted: October 12, 1993

1. Introduction

This article presents a detailed analysis of uncertainties associated with a new instrument (Noise Calibration System 1, or NCS1) for calibrating noise temperature. The instrument was recently developed at the National Institute of Standards and Technology, and is described in the accompanying articles [1] and [2]. Briefly, it consists of two noise standards and a total-power, null-balanced, heterodyned radiometer. One of the noise standards is a blackbody radiator at ambient temperature. In the present implementation of the system, the other standard is also a blackbody radiator, at liquid nitrogen temperature—the NIST primary coaxial cryogenic standard [3] However, any stable, calibrated noise source with noise temperature other than ambient and equipped with a proper connector can be substituted (with some degradation in performance, as discussed in this article).

A single-pole, triple-throw switch at the radiometer input provides dedicated ports for the two standards and the noise source under test (the sources). As presently implemented, NCS1 can calibrate coaxial noise sources with noise temperatures between cryogenic and 3×10^5 K, in a frequency range from 1 GHz to 12 GHz. Access to an external vector network analyzer to characterize the system's input ports is required.

A system equation describing the NCS1's functioning [2] is amended to explicitly show the inherent uncertainty in the determination of the noise temperature of the unknown noise source:

$$T_x = T_a + \frac{M_s}{M_x} \cdot \frac{\eta_{sw_s}}{\eta_{sw_x}} (T_s - T_a) \frac{10^{-(A_a - A_x)/10} - 1}{10^{-(A_a - A_s)/10} - 1} \pm \upsilon_c, \quad (1)$$

where

- T_x, T_a, and T_s are the available noise temperatures of the unknown noise source, the ambient temperature standard, and the nonambient temperature standard, respectively;
- M_s/M_x is a ratio of mismatch factors at the two input ports of the system dedicated to the nonambient standard and the noise source under

test (DUT). The two mismatch factors are defined as

$$M_i = \frac{(1-|\Gamma_i|^2)(1-|\Gamma_{SW_i}|^2)}{|1-\Gamma_i \Gamma_{SW_i}|^2}, \quad i = s, x, \tag{2}$$

where Γ_i and Γ_{SW_i} are the reflection coefficients in Fig. 1.

- The term η_{SW_s}/η_{SW_x} is a ratio of the efficiencies of the two (slightly different) paths of the input switch, associated lengths of coaxial lines, and input connectors.

  An efficiency η is defined as a ratio of the power delivered to the output and the power delivered to the input of a linear two-port, $\eta = P_{del_{out}}/P_{del_{in}}$. Specifically, in the case of the input switch, assuming the isolator to provide infinite isolation,

$$\eta_{SW_i} = \frac{(1-|\Gamma_i|^2)\cdot|S_{21_{SW_i}}|^2}{(1-|\hat{\Gamma}_{SW_i}|^2)|1-S_{11_{SW_i}}\Gamma_i|^2}, \quad i = s, x, \tag{3}$$

where $S_{11_{SW_i}}$ and $S_{21_{SW_i}}$ are the S-parameters of the two paths of the input switch;

- The terms A_a and A_x in Eq. (1) stand for the attenuator dial settings, in dB, needed to balance the system; and
- The last term explicitly denotes the combined standard uncertainty u_c associated with the NCS1. It is addressed in the rest of the article.

The system equation [2] can be written in a shorthand form as

$$T_x = T_a + M\,\eta_{SW}\,(T_s - T_a)\,Y. \tag{4}$$

The terms in Eq. (4) correspond to their counterparts in Eq. (1) in a straightforward manner; the uncertainty u_c is omitted in Eq. (4). Both Eq. (1) without u_c and Eq. (4) are referred to as "the system equation" and used in the rest of this article.

1.1 Method of Evaluating Uncertainties

Uniform distributions are assumed for the Type B evaluation of uncertainties [4] associated with systematic effects. The standard uncertainty is $a/\sqrt{3}$, where a stands for the mean value of the upper and lower limits of the distribution of the

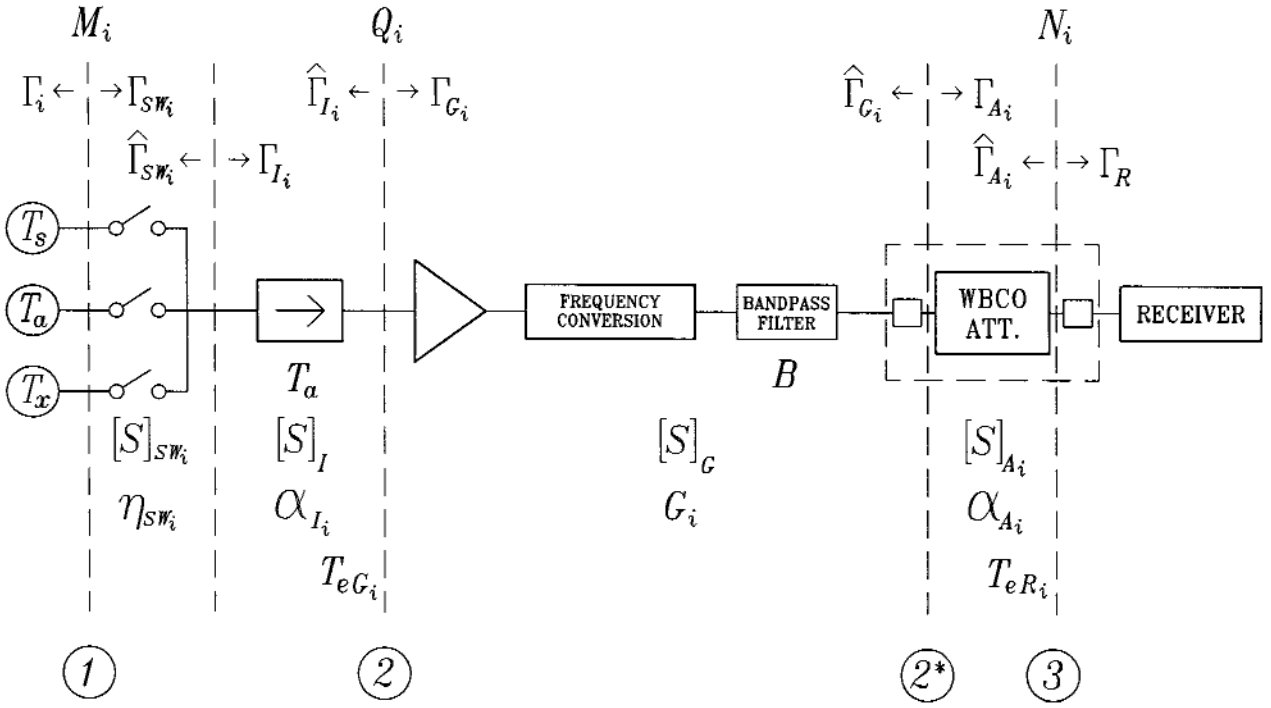

Fig. 1. A block diagram of NCS1.

quantity in question. Small random variations of uncertain origin are assumed to be normally distributed. Their effects are quantified by the experimental standard deviation of the mean of N measurements [5], [6], which is Type A evaluation of uncertainty. Due to practical considerations and because the Type A uncertainty is small compared to the Type B uncertainties, a decision has been made to ordinarily make only five measurements.

In accordance with NIST policies [7], both the combined standard uncertainty v_c and the expanded uncertainty U are reported. The combined standard uncertainty v_c is calculated by the RSS method of combining Type A and Type B uncertainty components. The coverage factor k in the expanded uncertainty has the value of 2.

2. Standard Uncertainties Arising from Systematic Effects (Type B)

There are eight significant Type B uncertainties in the NCS1. Uncertainties that are much smaller than these eight are not discussed, with the exception of the nonlinearity uncertainty. This uncertainty is addressed because the assumption of the radiometer linearity is central to the derivation of the system equation.

In general, the system Eq. (1) (or its compact version, Eq. (4) is differentiated with respect to those input quantities that are explicitly present in the equation (the temperatures of the nonambient and ambient standards, the mismatch factor ratio, the input switch efficiency ratio, and the attenuation). In three instances the system equation needs to be first *corrected* for the input quantity in question (in the case of the uncertainties associated with the isolator, the connector, and the "broadband mismatch"), and then the uncertainty in the correction factor is evaluated.

2.1 Numerical Values

The calculation of the uncertainties, as performed by the NCS1 software, substitutes the actual values of those parameters that are measured, or the conservative estimates of those that are impractical to measure. In particular, complex reflection coefficients are measured and used in the calculations. However, to obtain numerical values for the individual uncertainties in the following sections, all values are chosen to be conservatively representative of parameters encountered during a typical measurement at the arbitrarily chosen frequency of 2.0 GHz. Since the phases of the reflection coefficients are too variable to justify using some typical value, magnitudes only are used in the calculations of the uncertainties involving reflection coefficients.

Calculations are performed for two different system configurations: when the nonambient noise standard is the primary NIST cryogenic coaxial standard, and when a commercial hot source is used instead. The cryogenic standard has a smaller uncertainty (at 2 GHz, $T_s = 83\ \text{K} \pm 2.9\ \text{K}$), but is not well matched (assumed $|\Gamma_s| = 0.2$); the uncertainty of a commercial solid state noise source is necessarily larger (assumed to be $T_x = 8400\ \text{K} \pm 140\ \text{K}$), but its impedance is fairly close to 50 Ω (assumed $|\Gamma_x| = 0.1$).

The values of other input quantities entering into the calculations of most of the Type B uncertainties are: the temperature of the ambient standard $T_a = 296$ K, the magnitudes of the reflection coefficients of the radiometer port dedicated to the standard, $|\Gamma_{sw_s}| = 0.1$, and to the DUT, $|\Gamma_{sw_x}| = 0.1$.

Values of those input quantities that are particular to a specific uncertainty analysis are given in a corresponding section.

2.2 Nonambient Temperature Noise Standard

2.2.1 NIST Primary Coaxial Cryogenic Noise Standard If the NCS1 is configured with the NIST primary coaxial cryogenic noise standard serving as a nonambient standard, the uncertainty analysis proceeds as follows.

Source of Uncertainty: The uncertainty in the output temperature of the primary coaxial cryogenic standard, in kelvins, are given by [3]

$$\delta T_s = \pm 1.66 \pm 0.85\sqrt{f}, \tag{5}$$

where f stands for frequency in GHz.

Relative Standard Uncertainty: Assuming a uniform distribution, the relative standard uncertainty in the measurand T_x, in percent, due to the uncertainty in the temperature of the cryogenic standard δT_s is given by

$$\frac{\delta T_x}{T_x} = \pm \frac{T_s}{T_x}\left|\frac{T_x - T_a}{T_s - T_a}\right| \frac{\delta T_s}{T_s} \cdot \frac{100\%}{\sqrt{3}}. \tag{6}$$

For typical values (Sec. 2.1), this standard uncertainty is 0.76%.

2.2.2 Secondary Noise Standard Any stable, calibrated noise source with noise temperature other than ambient and equipped with a proper connector can be used as a nonambient temperature standard in place of the NIST primary coaxial standard.

Source of Uncertainty: The source of uncertainty δT_s, in kelvins, must be supplied by the calibration report accompanying the noise source which is to serve as the NCS1 standard. A typical commercial hot solid state noise source, calibrated at NIST at 2 GHz, may have its output reported as 8400 K ± 140 K.

Relative Standard Uncertainty: As in the case of the NIST cryogenic standard, the relative standard uncertainty, in percent, due to the uncertainty in temperature of the (secondary) noise standard, is given by

$$\frac{\delta T_x}{T_x} = \frac{T_s}{T_x}\left|\frac{T_x - T_a}{T_s - T_a}\right| \frac{\delta T_s}{T_s} \cdot \frac{100\%}{\sqrt{3}}. \tag{7}$$

For a typical value for the noise temperature of 8400 K ± 140 K, this standard uncertainty is 0.96%.

2.3 Ambient Temperature Standard

Source of Uncertainty: There are two sources of the uncertainty in the temperature of the ambient standard: the extent of a temperature gradient in the termination, and the measurement of the temperature.

The ambient temperature standard is contained in a temperature-controlled enclosure and isolated from potentially different temperatures at the radiometer input ports by a length of line and the input switch, both of which are contained in the same enclosure. Additionally, the temperature difference between the enclosure and the surrounding space is small, both temperatures being nominally ambient. Therefore, the temperature gradient in the ambient temperature standard is assumed to be negligible. Based on the type of the thermometer used to measure the ambient temperature, we can estimate this temperature with an uncertainty of $\delta T_a \approx 0.4$ K.

Relative Standard Uncertainty: The relative standard uncertainty, expressed in percent, is

$$\frac{\delta T_x}{T_x} = \frac{T_a}{T_x}\left|\frac{T_x - T_s}{T_a - T_s}\right| \frac{\delta T_a}{T_a} \cdot \frac{100\%}{\sqrt{3}}. \tag{8}$$

For typical values from Sec. 2.1, this uncertainty is 0.11% for the NCS1 system equipped with the NIST primary cryogenic standard, and negligible if a commercial hot source is used instead.

2.4 Isolator

Corrected System Equation: The derivation of the system equation [Eq. (1)] is based on the assumption of perfect isolation of the radiometer input [2]. An isolator is inserted between the reference planes 1 and 2 (Fig. 1) to provide the desired isolation. However, the isolation of any isolator is noninfinite, and the resulting effects are discussed below.

In the following discussion, the input switch is assumed to be ideal (lossless and reflectionless) and therefore transparent, which results in the following simplifications: $\Gamma_{SW_i} = \Gamma_{l_i}$, $\tilde{\Gamma}_{SW_i} = \Gamma_i$, and $\eta_{SW_i} = 1$. Furthermore, the heterodyning is assumed to be transparent, too.

The *corrected* system equation is derived following the procedure outlined in [2]. The two noise standards (with noise temperatures T_s and T_a), and the unknown noise source (with noise temperature T_x) are sequentially attached to the radiometer input, and the waveguide-below-cut-off (WBCO) attenuator is adjusted until the noise power delivered to the receiver P_{del} is the same in all three cases ($i = s, a, x$):

$$kB\{[T_i\alpha_{l_i} + T_a(1-\alpha_{l_i}) + T_{eG_i}]G_i\alpha_{A_i} + T_a(1-\alpha_{A_i}) + T_{eR_i}\}N_i = P_{del}, \tag{9}$$

where α_{l_i} and α_{A_i} are the available power ratios of the isolator and the attenuator, respectively, G_i is the available gain of the section between the reference planes 2 and 2* (Fig. 1), T_{eG_i} and T_{eR_i} are the effective noise temperatures defined in the reference planes 2 and 3, and N_i is the mismatch factor in the reference plane 3.

Assuming, as in [2] that the attenuator is lossless ($\alpha_{A_i} = 1$), and that the system gain preceding it is high enough for the noise contribution of the receiver to be negligible ($T_{eR_i} = 0$), the three equations become

$$kB[T_i\alpha_{l_i} + T_a(1-\alpha_{l_i}) + T_{eG_i}]G_i N_i = P_{del}, \quad i = s, a, x \tag{10}$$

The mismatch factor N_i reduces to $|S_{21_{A_i}}|^2$ for a lossless attenuator inserted in the reflectionless environment [2]. Following the procedure described in [2] and neglecting third- and higher-order terms, we obtain the corrected system equation

$$T_x = T_a + Y\frac{G_s}{G_x}\frac{\alpha_{l_s}}{\alpha_{l_x}}(T_s - T_a) + \frac{T_a}{G_x\alpha_{l_x}}[Y(G_s - G_a) - (G_x - G_a)] + \frac{1}{G_x\alpha_{l_x}}[Y(G_s T_{eG_s} - G_a T_{eG_a}) - (G_x T_{eG_x} - G_a T_{eG_a})], \tag{11}$$

where Y stands for

$$Y=\frac{\frac{|S_{21_{A_a}}|^2}{|S_{21_{A_x}}|^2}-1}{\frac{|S_{21_{A_a}}|^2}{|S_{21_{A_s}}|^2}-1}. \tag{12}$$

If the isolation were taken to be infinite, the available gain terms G_i and the effective input noise temperatures T_{eG_i} would become independent of the input conditions, and the ratio $\alpha_{I_s}/\alpha_{I_x}$ would reduce to M_x/M_s [2]. Equation (11) would then become the system equation [Eq. (1)], adjusted to reflect the assumption of the ideal input switch ($\eta_{sw_s}/\eta_{sw_x}=1$).

Source of Uncertainty: The correction (a full difference between the corrected and idealized system equations) consists of two terms:

$$\epsilon_I=\epsilon_{T_{eG}}+\epsilon_G, \tag{13}$$

where $\epsilon_{T_{eG}}$ and ϵ_G describe the corrections due to the variability of the effective input noise temperature T_{eG} and the available gain G, respectively, as a function of the changes of the input impedance. Specifically

$$\epsilon_{T_{eG}}=\frac{1}{G_x\alpha_{I_x}}[Y(G_s T_{eG_s}-G_a T_{eG_a})-$$

$$(G_x T_{eG_x}-G_a T_{eG_a})], \tag{14}$$

and

$$\epsilon_G=(T_x-T_a)\left(\frac{G_s}{G_x}-1\right)$$

$$+\frac{T_a}{\alpha_{I_x}}\left[Y\left(\frac{G_s}{G_x}-\frac{G_a}{G_x}\right)-\left(1-\frac{G_a}{G_x}\right)\right]. \tag{15}$$

"Variable T_{eG}" Correction: Experimental evaluation of the system has shown that changes of the effective input noise temperature with the maximal possible variation of the input impedance (a sliding short) is still below the system resolution; $\epsilon_{T_{eG}}$ is therefore neglected, (that is, Eq. (14) becomes equal to zero), and Eq. (13) reduces to $\epsilon_I=\epsilon_G$.

Variable G Uncertainty: The source of the uncertainty is the sensitivity of the available gain G_i in Eq. (15) to the changes in the input impedances Γ_i. The available gain of the amplifier/left matching pad combination is given by

$$G_i=\frac{(1-|\tilde{\Gamma}_{I_i}|^2)\,|S_{21_G}|^2}{(1-|\tilde{\Gamma}_{G_i}|^2)|1-S_{11_G}\tilde{\Gamma}_{I_i}|^2}. \tag{16}$$

If third- and higher-order terms are neglected and the assumption that $\tilde{\Gamma}_{G_i}\approx 0$ (assuring the reflectionless environment for the attenuator [2]) is taking into account, the ratio of the available gain terms G_s/G_x in Eq. (15) becomes

$$\frac{G_s}{G_x}\approx 1-|\tilde{\Gamma}_{I_s}|^2+|\tilde{\Gamma}_{I_x}|^2+2\,Re\{(\tilde{\Gamma}_{I_s}-\tilde{\Gamma}_{I_x})\,S_{11_G}\}$$

$$\approx 1+|S_{21}\,S_{12}|_I^2\,(|\Gamma_x|^2-|\Gamma_s|^2)+$$

$$+2\,Re\{(S_{21}\,S_{12})_I\,(\Gamma_s-\Gamma_x)\,(S_{22_I}^*-S_{11_G})\}. \tag{17}$$

An analogous expression holds for the G_a/G_x ratio in Eq. (15).

The term $|S_{12}\,S_{21}|_I^2$ in Eq. (17) is much smaller than unity even for a poor isolator, and, furthermore, it also multiplies a *difference* of the squares of the magnitudes of the reflection coefficients, so their product can be safely neglected. With that in mind, the worst-case expression for the ϵ_G term becomes

$$\epsilon_G\le 2|T_x-T_a||S_{21}S_{12}|_I\,(|S_{22_I}|+|S_{11_G}|)(|\Gamma_s|+|\Gamma_x|)+$$

$$+2\,\frac{T_a}{\alpha_{I_x}}\,|S_{21}\,S_{12}|_I\,(|S_{22_I}|+|S_{11_G}|)\,[Y(|\Gamma_s|+|\Gamma_a|)$$

$$+|\Gamma_x|+|\Gamma_a|]. \tag{18}$$

Relative Standard Uncertainty: The quantity ϵ_G in Eq. (18) is taken to be uniformly distributed, with the relative standard uncertainty of

$$\frac{\delta T_x}{T_x}=2\left\{\left|1-\frac{T_a}{T_x}\right|\,|S_{21}\,S_{12}|_I\,(|S_{22_I}|+|S_{11_G}|)(|\Gamma_s|+|\Gamma_x|)\right.$$

$$+\frac{T_a}{T_x\alpha_{I_x}}\,|S_{21}\,S_{12}|_I\,(|S_{22_I}|+|S_{11_G}|)\,[Y(|\Gamma_s|$$

$$\left.+|\Gamma_a|)+|\Gamma_x|+|\Gamma_a|]\right\}\cdot\frac{100\%}{\sqrt{3}}. \tag{19}$$

The factor Y is ordinarily measured. However, in order to estimate a typical uncertainty, it is here approximated [2] by

$$Y \approx \left| \frac{T_x - T_a}{T_s - T_a} \right|. \quad (20)$$

Under the following assumptions: an isolator with $|S_{21}\, S_{12}|_I \approx 0.003$ (corresponding to 50 dB isolation) and $|S_{22}| \approx 0.1$, $\alpha_{l_x} \approx 0.95$, $|\Gamma_a| \approx 0.01$, $|S_{11G}| \approx 0.1$, other values from the list of typical values in Sec. 2.1, the relative standard uncertainty is 0.05% for the NCS1 system equipped with the NIST primary cryogenic standard, and 0.03% if a commercial hot source is used instead.

2.5 Connector

Corrected System Equation: Both the nonambient standard and the DUT have connectors that are reflective and lossy; those parameters are also partially nonrepeatable. The connectors are modeled as two-ports of efficiencies η_{CNN_s} and η_{CNN_x} that are each in cascade with the input ports of the radiometer. The corrected system equation becomes

$$T_x = T_a + \frac{\eta_{CNN_s}}{\eta_{CNN_x}} \cdot \frac{M_s}{M_x} \cdot \frac{\eta_{SW_s}}{\eta_{SW_x}} (T_s - T_a) Y. \quad (21)$$

Source of Uncertainty: Following the reasoning in [8], we assume that, for type N connectors, the efficiency ratio $\eta_{CNN_s}/\eta_{CNN_x}$ in Eq. (21) reduces to $(1 + C_1\sqrt{f} + C_2 f)$, where the constants C_1 and C_2 have been experimentally determined to have the values of $C_1 = 0.00087/\sqrt{3}$} and $C_2 = 0.035$, and f is the frequency in GHz. (For a connector with a center conductor different in diameter, the constant C_1 is scaled by a factor $(D/D_{7mm})^2$ since the loss in an uniform coaxial structure is proportional to the square of the magnetic field's magnitude.)

The constant C_1 encompasses components of connector variability arising from both systematic and random effects. Since the noise temperature measurements are performed without connecting and disconnecting the connectors (of the nonambient standard or the DUT), the random component cannot be assumed to average out.

The reference plane defined for calculating the connector uncertainty during a noise temperature measurement is assumed to be *to the left of the connector* in Fig. 1. In other words, a DUT is calibrated "stripped" of its own connector. In practice, the connector contribution to the combined standard uncertainty in noise measurements is so small for precision connectors in good condition and for frequencies in the microwave region of the spectrum that this assumption is admissible. The uncertainty arising in the connectors is at present an incompletely explored topic needing further study. The importance of resolving this issue becomes even greater with smaller connectors and higher frequencies.

Relative Standard Uncertainty: The entire correction (a difference between Eq. (21) and the system equation [Eq. (4)]) is uncertain, with ϵ_{CNN} having a uniform distribution with upper and lower limits of

$$\epsilon_{CNN} = (T_x - T_a)\left(1 - \frac{\eta_{CNN_s}}{\eta_{CNN_x}}\right). \quad (22)$$

Substitution of experimental constants for the (1 − efficiency ratio) term in Eq. (22) results in the relative connector standard uncertainty (in percent) of

$$\frac{\delta T_x}{T_x} = \left(\frac{0.087}{\sqrt{3}} + 0.035\right)\sqrt{f}\left|1 - \frac{T_a}{T_x}\right|/\sqrt{3}. \quad (23)$$

For typical values listed in Sec. 2.1, this standard uncertainty is 0.07% whether the NIST primary cryogenic standard or a commercial hot source is used.

2.6 Mismatch Factor

Source of Uncertainty: The mismatch factors between the nonambient standard and the radiometer, and between the DUT and the radiometer, are calculated from the reflection coefficient measurements [2]. Since only a *ratio* of the mismatch factors is used in the system equation, the uncertainties associated with the measurements of the reflection coefficients partially cancel.

The ratio of the mismatch factors M_s and M_x can be approximated in a well-matched system ($|\Gamma| \ll 1$) by

$$\frac{M_s}{M_x} \doteq 1 - (a_s - a_{r_s})^2 - (b_s - b_{r_s})^2 + (a_x - a_{r_x})^2 + (b_x + b_{r_x})^2, \quad (24)$$

where a_i and b_i stand for the real and imaginary parts of the measured (complex) reflection coefficients: Γ_s and Γ_x, looking into the sources (the nonambient standard or the DUT), and Γ_{SW_s} and Γ_{SW_x}, looking into the radiometer ports dedicated to the nonambient standard and the DUT. The relative uncertainty of that ratio can be approximated by

$$\frac{\delta(M_s/M_x)}{(M_s/M_x)} \doteq 2(A + B), \quad (25)$$

where A and B are defined as

$$A=(a_x-a_{\mathrm{sw}_x})(\delta a_x-\delta a_{\mathrm{sw}_x})-$$

$$(a_s-a_{\mathrm{sw}_s})(\delta a_s-\delta a_{\mathrm{sw}_s}), \tag{26}$$

$$B=(b_x+b_{\mathrm{sw}_x})(\delta b_x+\delta b_{\mathrm{sw}_x})-$$

$$(b_s+b_{\mathrm{sw}_s})(\delta b_s+\delta b_{\mathrm{sw}_s}). \tag{27}$$

It is assumed that the real and imaginary parts of the reflection coefficient are measured with an equal uncertainty of 0.005, which is independent of the magnitude of the reflection coefficients, as long as they are reasonably small (≤ 0.1 or so). With these provisions, Eq. (25) reduces to

$$\frac{\delta M_s/M_x}{M_s/M_x}\doteq 2|(b_x+b_{\mathrm{sw}_x})-(b_s+b_{\mathrm{sw}_s})|$$

$$(0.005+0.005). \tag{28}$$

Relative Standard Uncertainty: The relative standard uncertainty in T_x due to the uncertainty in the measurement of the reflection coefficients used in the calculation of the mismatch factor ratio, in percent, is given by

$$\frac{\delta T_x}{T_x}=\left|1-\frac{T_a}{T_x}\right|\frac{\frac{\delta M_s}{M_x}}{\frac{M_s}{M_x}}\cdot\frac{100\%}{\sqrt{3}}. \tag{29}$$

For typical values given in Sec. 2.1, this standard uncertainty is 0.07% for the NCS1 system equipped with the NIST primary cryogenic standard and 0.01% if a commercial hot source is used instead.

2.7 Asymmetry

Source of Uncertainty: The nonambient standard and the DUT are each attached to their own, dedicated input port. The input signals originating in the two sources, therefore, take slightly different paths to the rest of the radiometer. The two paths consist of a connector, a length of coaxial line, and one side of the input switch, and are modeled as two two-ports in cascade with the rest of the radiometer input [2]. The efficiencies of the two-ports, labeled "switch efficiencies" for short, enter into the system equation [Eq. (4)] as the *asymmetry correction* $\eta_{\mathrm{sw}_s}/\eta_{\mathrm{sw}_x}$.

The efficiency of a two-port depends on both th two-port and its environment, and so cannot b simply and directly measured. However, in a wel matched system, the efficiency can be approxi mated by

$$\eta^*=\frac{|S_{21}|^2}{1-|S_{11}|^2}, \tag{30}$$

which depends on the two-port alone and can b calculated from the S-parameters measured b conventional methods.

It is convenient to express the ratio of the ap proximate efficiencies in logarithmic terms:

$$\frac{\eta_{\mathrm{sw}_s}}{\eta_{\mathrm{sw}_x}}\approx\frac{\eta^*_{\mathrm{sw}_s}}{\eta^*_{\mathrm{sw}_x}}=\frac{10^{\frac{\eta^*_{\mathrm{sw}_s}}{10}}}{10^{\frac{\eta^*_{\mathrm{sw}_x}}{10}}}=10^{\frac{\Delta\eta^*_{\mathrm{sw}}}{10}}, \tag{31}$$

where $\Delta\eta^*_{\mathrm{sw}}$ stands for the difference (in dB) of the approximate efficiencies of the two paths.

Equation (4) becomes

$$T_x=T_a+\frac{M_s}{M_x}\cdot 10^{\frac{\Delta\eta^*_{\mathrm{sw}}}{10}}(T_s-T_a)Y \tag{32}$$

Based on experimental data, the uncertainty in the measurements of $\Delta\eta^*_{\mathrm{sw}}$, $\delta(\Delta\eta^*_{\mathrm{sw}})$, is estimated to be typically 0.01 dB for low-loss two-ports.

Relative Standard Uncertainty: The relative uncertainty in T_x (in percent) due to the uncertainty in the measurement of the input switch asymmetry is given by

$$\frac{\delta T_x}{T_x}=\left|1-\frac{T_a}{T_x}\right|\frac{\ln 10}{10}\cdot\delta(\Delta\eta^*_{\mathrm{sw}})\cdot\frac{100\%}{\sqrt{3}}. \tag{33}$$

For typical values (Sec. 2.1), this standard uncertainty is 0.13% whether the NIST primary cryogenic standard or a commercial 'hot source is used.

2.8 Broadband Mismatch

Corrected System Equation: A radiometer is a broadband instrument and ought to be described by a system equation that reflects that fact:

$$\int_B T_x g\,df=\int_B[T_a+M\eta Y(T_s-T_a)]\,g\,df, \tag{34}$$

where B stands for the limiting system bandwidth, M is a ratio of mismatch factors at the reference

plane 1 (Fig. 1), η is a ratio of the input switch efficiencies, and Y is the system balancing factor defined in Eqs. (4) and (1). The transfer function g is taken to be 1 within the band, and to vanish outside of the band.

The above equation reduces to Eq. (4) if all terms are independent of frequency. The noise temperatures T_i are broadband by definition. Components of a noise measurement system determining the factor Y are manufactured to be broadband within the bandwidth of interest B. In the case of the NCS1, the mixer that downconverts the RF noise to the IF frequency, the WBCO attenuator used to balance the IF noise signals, and the square law detector that produces a dc output all satisfy the requirement. If the η term in Eq. (34) is also assumed to be broadband, the *corrected* system equation becomes

$$T_x = T_a + \frac{\int_B M_s g\,df}{\int_B M_x g\,df}\eta\,(T_s - T_a)\,Y. \qquad (35)$$

The mismatch factors M_s and M_x are not directly measured. Instead, the mismatch factors M_{s_0} and M_{x_0} are calculated from the measurements of the reflection coefficients, performed at the single (operating) frequency f_0. Since reflection coefficients in general vary strongly with frequency, and the integration process indicated by Eq. (35) is not performed, an error issues.

Source of Uncertainty: The difference between the corrected and idealized system equations is taken to represent the limits of the broad band mismatch uncertainty; the quantity ϵ_{bbm} is assumed to be uniformly distributed, with upper and lower bounds of

$$\epsilon_{bbm} = (T_x - T_a)\left(\frac{\int_B M_s g\,df/M_{s_0}}{\int_B M_x g\,df/M_{x_0}} - 1\right). \qquad (36)$$

The mismatch factors M_{i_0}, $i = s,x$ are a function of the reflection coefficients of the noise sources Γ_i and of the radiometer input ports Γ_{sw_i} [2]. If the following assumptions can be made: an ideal (reflectionless, lossless, symmetrical) input switch, an infinitely isolating isolator, and a lossless uniform transmission line of a length l between the switch input and the isolator, the mismatch factors at the operating frequency f_0 are given by

$$M_{0_i} = \frac{(1-|\Gamma_i|^2)(1-|S_{11_1}|^2)}{\left|1-\Gamma_i S_{11_1} e^{-j\frac{4\pi l}{v} f_0}\right|^2}, \qquad (37)$$

where v is the velocity of light in the transmission line.

Substituting the Eq. (37) into Eq. (36), neglecting third- and higher-order terms, and performing the integration over the range in Fig. 2, we obtain the expression for the limits of broadband mismatch uncertainty [9].

$$\epsilon_{bbm} \leq 2|T_x - T_a|\,Re\,\{S_{11_1}(\Gamma_s - \Gamma_x)\}$$
$$\left[1 - \cos\left(\frac{4\pi l}{v} f_{IF}\right) \operatorname{sinc}\left(\frac{2\pi l}{v} B\right)\right]. \qquad (38)$$

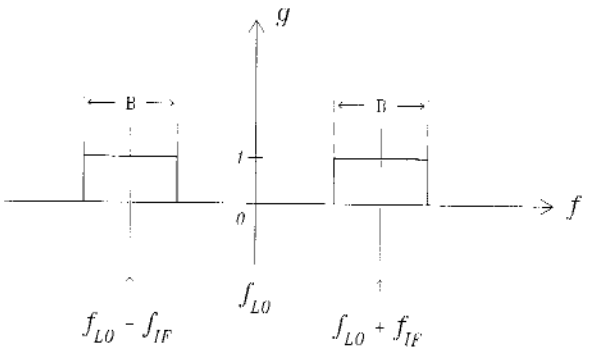

Fig. 2. The integration range.

Relative Standard Uncertainty: The relative standard uncertainty due to broadband mismatch in a reasonably matched coaxial systems $\delta T_x/T_x$, in percent, is given by

$$\frac{\delta T_x}{T_x} = 2\left|1 - \frac{T_a}{T_x}\right| Re\,\{S_{11_1}(\Gamma_s - \Gamma_x)\}\left[1 - \cos\left(\frac{4\pi l f_{IF}}{v}\right)\right.$$
$$\left.\operatorname{sinc}\left(\frac{2\pi l}{v} B\right)\right]\frac{100\%}{\sqrt{3}}. \qquad (39)$$

For the purpose of getting the numerical value here, the most unfavorable phasing of the reflection coefficients Γ_s and Γ_x is assumed, resulting in the addition of their magnitudes. For the radiometer with a bandwidth of 4 MHz, an IF frequency of 30 MHz, and an isolator with the magnitude of its S_{11} parameter of 0.1, and a length of the line at the input of 0.2 m, the standard uncertainty is 0.1% with the NIST primary cryogenic standard, or

0.07% if a (better matched) commercial hot source is used.

2.9 Attenuator

The attenuator used in the NCS1, a 30 MHz, precision waveguide-below-cutoff attenuator, serves as a nulling device. The following analysis is valid when the attenuator is operated at an attenuation that is sufficiently high (above 20 dB, which, together with the insertion loss of 12 dB, puts the total *minimal* attenuation at 32 dB). At attenuation values lower than that, the deviation of the attenuation from linearity with respect to the coil separation distance is pronounced due to multiple modes being present.

The attenuator, with its tuned circuits at the input and output ports, has been observed to change its bandwidth as a function of the attenuation setting. A separate (system-limiting) 4 MHz bandpass filter, centered around 30 MHz has been therefore inserted ahead of the attenuator.

Source of Uncertainty: The uncertainty in the value of A_i for a precision waveguide-below-cutoff attenuator is given in [10] by

$$\delta A_i = kA_i + C, \tag{40}$$

where $k = 0.0003$, and $C = 0.003$ dB.

Relative Standard Uncertainty: The relative standard uncertainty in the DUT's noise temperature traceable to the attenuator is given by

$$\frac{\delta T_x}{T_x} = \left|1 - \frac{T_a}{T_x}\right| \frac{\ln 10}{10} \cdot k[K_1(A_x - A_a) - K_2(A_s - A_a)] \cdot \frac{100\%}{\sqrt{3}}, \tag{41}$$

where

$$K_1 = \frac{10^{-(A_a - A_x)/10}}{10^{-(A_a - A_x)/10} - 1}, \tag{42}$$

and

$$K_2 = \frac{10^{-(A_a - A_s)/10}}{10^{-(A_a - A_s)/10} - 1}. \tag{43}$$

Since only the differences in attenuation are used, the constant C in Eq. (40) drops out of consideration. For (experimentally obtained) values of attenuation of $A_a = 22.87$ dB, $A_x = 34.54$ dB, and $A_s = 20.95$ dB, and with the typical values for other parameters from Sec. 2.1, the relative uncertainty is 0.06% for the NCS1 system equipped with the NIST primary cryogenic standard, and negligible if a commercial hot source is used instead.

2.10 Linearity

Source of Uncertainty: In order to accurately measure different noise power levels of the two noise standards and the DUT, a radiometer has to be linear within the specified dynamic range.

In the case of a balanced instrument such as the NCS1, the linearity requirement applies to the signal path up to and including the balancing mechanism. Referring to Fig. 1, the section of the NCS1 radiometer that needs to be linear extends between the input ports and the output of the WBCO attenuator. Any nonlinearity beyond the attenuator affects all three noise powers equally (since they had been adjusted to the same level), and therefore cancels out.

The likely causes of deviation from linearity are: saturation in the RF amplifier; insufficient power of the local oscillator, causing the mixer to become nonlinear in the signal [11]; saturation in IF amplifiers preceding the attenuator; and a nonlinear behavior of the attenuator.

Instead of verifying the linearity of the individual components, the overall system linearity has been experimentally investigated. A fixed attenuator of approximately 3 dB is inserted between the isolator and the RF amplifier. A measurement of the noise temperature of the DUT is performed in the usual manner. The procedure is repeated a sufficient number of times and averaged to obtain a statistically convergent estimate of T_x. The attenuator is then removed, and the measurements of T_x repeated.

The obtained null difference has proven conclusively that no deviation from linearity exists, within the resolution of the NCS1 system.

3. Standard Uncertainties Arising from Random Effects (Type A)

The effects of the Type A uncertainties are quantified by calculating the standard deviation of the mean of N independent measurements of the noise temperature of the unknown source T_x, according to

$$\sqrt{\frac{\sum_{i=1}^{N}(T_{x_i}-\overline{T}_x)^2}{N(N-1)}} \tag{44}$$

where T_{x_i} stands for the ith measured value and $\overline{T}_x$ for the mean of N measurements. The intermediate results of Eq. (44) are displayed after each measurement so the operator can select how many need to be performed. Since the Type A uncertainties are overshadowed by the Type B uncertainies in this system (by an order of magnitude), N can be chosen to be small (but no less than 5).

A representative value for the experimental standard deviation of the mean of five independent measurements of the noise temperature T_x is 4 K for a 8400 K source, or 0.05 %.

4. Combined Uncertainty

The combined standard uncertainty is calculated by the RSS method. The coverage factor in the expanded uncertainty k is 2. Table 1 presents the typical uncertainties for a noise source having the noise temperature of 8400 K, measured at 2 GHz with either the NIST primary coaxial cryogenic standard, or a commercial hot source serving as a (non ambient) standard.

5. Discussion

Based on the results of the analysis of the uncertainties inherent to the measurement procedure, several comments regarding the performance of the NCS1 seem appropriate. The overall reported accuracy of the NCS1 is comparable to the accuracies of various noise measurement systems at NIST, if those were calculated by the same method. However, it compares unfavorably with the measurement accuracies of most other physical quantities. Some measures that would improve the NCS1 accuracy are discussed here.

From Table 1, the most effective measure to improve the overall accuracy of the NCS1 would be an improvement of the nonambient primary noise standard's accuracy. The improvement persists whether a more accurate standard is used directly by NCS1 or a secondary commercial source, calibrated against a better primary standard having lower associated uncertainties, is used. A redesign of the primary noise standard is beyond the scope of this work, however.

Several standard uncertainties associated with the NCS1, as shown in Table 1, are proportional to the difference between the noise temperatures of the DUT and the nonambient standard. Relatively cool sources (such as commercially available hot/cold loads or solid state noise sources with $T_x \approx 1400$ K) can be calibrated with better accuracy than more popular hot sources of $T_x \approx 9000$ K.

Table 1: Typical NCS1 uncertainties with either a NIST primary coaxial standard or a calibrated hot noise source standard

Source of uncert.	NCS1 with NCST coax. standard	NCS1 with hot source standard
Nonambient std.	0.76%	0.96%
Ambient std.	0.11%	negl.
Isolator	0.05%	0.03%
Connector	0.07%	0.07%
Mismatch	0.07%	0.01%
Switch asymmetry	0.13%	0.13%
Broadband mismatch	0.10%	0.07%
Attenuator	0.06%	negl.
Linearity	negl.	negl.
Random effects	0.03%	0.03%
Comb. std. uncert.	0.80%	0.97%
Expanded Uncert.	1.60%	1.95%

The NCS1 ambient standard accuracy can be improved readily, by using a better thermometer, by employing a four-wire resistance measuring technique, and by having an accurate voltmeter. A decrease in the uncertainty in the ambient standard from the present 0.4 K to 0.1 K would propagate into a decrease in the standard uncertainty arising from the ambient standard uncertainty from the present 0.11% to a negligible 0.03%.

Adding additional 25 dB of isolation practically eliminates the uncertainty traceable to isolation, but adds bulk and significantly increases the cost of the radiometer, since a separate extra isolator is needed for each octave.

The standard uncertainty associated with the broadband mismatch increases fast with the increasing length of the input transmission line, the IF frequency and the system bandwidth. The input section must be kept as compact as possible. A 5 MHz WBCO attenuator, replacing the 30 MHz attenuator used in the implemented NCS1, coupled with a 4 MHz bandpass filter, would reduce the standard uncertainty from 0.1% to a negligible 0.003%.

In some applications, overriding accuracy demands might prompt the elimination of the input

switch. Although causing more connector wear and slowing the operations, it removes the uncertainty associated with switch asymmetry entirely and, by shortening the physical length of the input signal path, also decreases the uncertainty associated with the broadband mismatch. Additional small accuracy gain is made because the switch non-repeatability contribution to the Type A uncertainty is eliminated.

The uncertainty asssociated with random effects can be reduced in several ways. Selecting truly low-noise RF amplifiers with a sufficient gain (to make the mixer noise contribution negligible) would lessen the system noise contribution and therefore the random scatter. So would lowering the noise contribution of the passive components in the input section. Specifically, the switches need to be selected for their low losses, and the interconnecting coaxial lines kept as short as possible. An attempt to reduce the noise contribution by cooling the input section components must be done advisedly, however, since the derivation of the system equation presupposes them to be at the same temperature as the ambient standard.

The simple expedient of increasing the number of measurements also reduces the Type A uncertainty. Since each measurement compares the unknown noise temperature to that of the noise standards, the system drift over a longer period of time needed to perform an increased number of measurement is not a limiting factor. The gain in accuracy due to the random scatter reduction, marginal at present, might be worth the effort if the Type B uncertainties were reduced.

Acknowledgment

The author wishes to thank her senior colleague, William C. Daywitt, for his generous help and encouragement, and the Calibration Coordination Group of the Department of Defense for support.

6. References

[1] S. P. Pucic, Null-balanced total-power radiometer system NCS1, J. Res. Natl. Inst. Stand. Technol. **98**, 45 (1994).
[2] S. P. Pucic, Derivation of the system equation for Null-balanced total-power radiometer system NCS1, J. Res. Natl. Inst. Stand. Technol. **98**, 55 (1994).
[3] W. C. Daywitt, A coaxial noise standard for the 1 GHz to 12.4 GHz frequency range, Natl. Bur. Stand. (U.S.) Tech. Note 1074 (1984).
[4] Guide to the expression of uncertainty in measurement, ISO/TAG 4/WG 3: June 1992.
[5] C. Eisenhart, Expression of the uncertainties of final results, Science **160**, 1201–1204 (1968).
[6] K. A. Brownlee, Statistical Theory and Methodology in Science and Engineering, Willey & Sons (1965).
[7] B. N. Taylor and C. E. Kuyatt, Guidelines for evaluating and expressing the uncertainties of NIST measurement results, Natl. Inst. Stand. Technol. Tech. Note 1297 (1993).
[8] W. C. Daywitt, Radiometer equation and analysis of systematic errors for the NIST automated radiometers, Natl. Inst. Stand. Technol. Tech. Note 1327 (1989).
[9] S. Perera, Broadband Mismatch Error in Noise Measurement Systems, CPEM Digest (1992).
[10] R. T. Adair and D. H. Russell, A calibration service for 30 MHz attenuation and phase shift, Natl. Bur. Stand. (U.S.), Spec. Publ. 250–32 (1988).
[11] S. A. Maas, Microwave Mixers, Artech House (1986).

About the author: *Sunchana P. Pucic is an electronics engineer in the Microwave Metrology Group of the Electromagnetic Fields Division at NIST. The National Institute of Standards and Technology is an agency of the Technology Administration, U.S. Department of Commerce.*

Volume 99, Number 1, January–February 1994
Journal of Research of the National Institute of Standards and Technology

[J. Res. Natl. Inst. Stand. Technol. 99, 77 (1994)]

Cryogenic Blackbody Calibrations at the National Institute of Standards and Technology Low Background Infrared Calibration Facility

Volume 99 Number 1 January–February 1994

R. U. Datla, M. C. Croarkin, and A. C. Parr

National Institute of Standards and Technology,
Gaithersburg, MD 20899-0001

The Low Background Infrared Calibration Facility (LBIR) at the National Institute of Standards and Technology has been in operation for calibration measurements of the radiant power emitted from infrared radiation (IR) sources, such as cryogenic blackbodies, for more than 2 years. The IR sources are sent to NIST by customers from industry, government, and university laboratories. An absolute cryogenic radiometer is used as the standard detector to measure the total radiant power at its aperture. The low background is provided by a closed cycle helium refrigeration system that maintains the inner parts of the calibration chamber at 20 K. The radiance temperature of the blackbody is deduced from the measured power and compared with the blackbody temperature sensor data. The calibration procedures and data analysis are illustrated using the measurements of a typical blackbody.

Key words: blackbody calibrations; cryogenic blackbodies; cryogenic radiometer; electrical substitution radiometry; low background infrared radiation calibrations; radiometry.

Accepted: November 19, 1993

1. Introduction

The national need to establish a primary standard reference for calibrating infrared sensors led to the establishment, in 1989, of the Low Background Infrared Calibration Facility (LBIR) at the National Institute of Standards and Technology. This facility has been serving a variety of users from industry and government laboratories by providing calibrations of cryogenic blackbody sources. These sources are used by the customer for calibrations of their infrared sensor systems. An absolute cryogenic radiometer (ACR) of the electrical substitution type has been developed as the standard reference detector for the LBIR calibrations. The ACR measures the total radiant power incident on its precision aperture. Its operating range for radiant power measurements is 20 nW to 100 μW with an expanded uncertainty of ±1% (95% confidence level). The physical description of the ACR and its characterization as an absolute detector for radiant power measurements have been described in Ref. [1]. The LBIR chamber is shown in Fig. 1.

The cylindrical vacuum tank housing the ACR detector and the customer blackbody source is made of stainless steel and is 152 cm long and 60 cm in diameter. Two shields made of copper (shown in the cutaway portion of Fig. 1) separated by a 2.54 cm gap are cooled by a helium refrigerator which circulates cooled helium gas (15 K) through copper lines vacuum brazed to these shields. The inner shield operates at 20 K and provides the low thermal radiation background inside the chamber. The inner surface of the inner shield has a highly

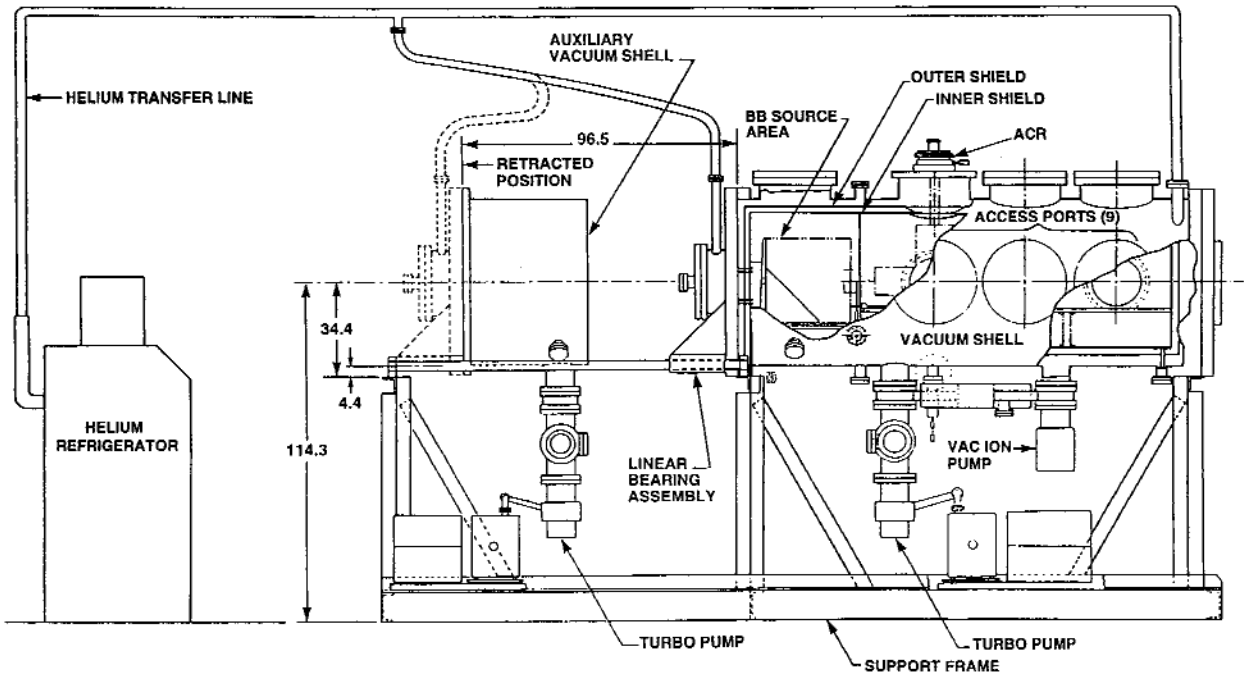

Fig. 1. LBIR chamber with partial cutaway showing the major features of the apparatus.

absorbent black coating of IITRI MH-2200 paint[1] to reduce scattered radiation. The ACR can be placed in any of the three ports of the LBIR chamber, which are located at distances of approximately 30 cm, 65 cm, and 100 cm from the blackbody source under test. The placement of the ACR can be chosen so that the radiant power at its aperture is in the ACR measurement range. A complete description of the facility can be found in a previous publication [3].

The general requirements for blackbody calibrations are described in Sec. 2 of this article. The procedures for handling the cryogenics of the calibration setup and the procedures adopted for measurements and analysis are described in Sec. 3. A recent blackbody calibration illustrates the procedures. The blackbody in question has two sensors and is referred to as BB in this paper.

2. Calibration Requirements

Calibration requirements fall into two categories: 1) needs established by the customer and 2) needs of the NIST LBIR facility. A typical customer requirement for the BB is as follows: 1) measure the radiant power at the ACR aperture for the blackbody temperature range of 200 K to 400 K in increments of 25 K for the source aperture diameter of 650 μm and 2) calibrate the temperature sensors of the source by comparing with the deduced radiance temperature. NIST issues guidelines to the customer for preparing the blackbody source to conform to the vacuum and allowable contaminant level specifications of the LBIR chamber. The NIST requirement specifies that the partial pressure of hydrocarbons (beyond approximately 45 u) should not exceed 1.33×10^{-8} Pa for a total base pressure of 1.33×10^{-6} Pa. Other requirements are described in detail in Ref. [3]. NIST also supplies the customer with a mounting plate and guidelines for installing the plate on the blackbody source [3].

3. Calibration Procedures

3.1 Cryogenic Apparatus and Preparation for Measurements

The blackbody is integrated into the LBIR chamber after testing its vacuum integrity. Cryoconditioning of the LBIR chamber follows with the inner shield of the chamber being cooled to approximately 20 K and the outer shield being cooled to approximately 40 K. The blackbody mounting

[1] Certain commercial equipment, instruments, or materials are identified in this paper to specify adequately the experimental procedure. Such identification does not imply recommendation or endorsement by the National Institute of Standards and Technology, nor does it imply that the materials or equipment identified are necessarily the best available for the purpose.

shelf and the main chamber have separate cold helium feeds with flow control valves to allow diversion of additional coolant to the blackbody, if needed. The cryoshields have several silicon diode thermometers attached at various points. These thermometers are monitored during calibration to ensure stability of the IR environment.

In order to provide a steady background flux for the ACR, a copper disk separates the blackbody chamber from the ACR chamber. This disk, called the isothermal plate, is moderately thermally insulated from the inner shield. The isothermal plate is fitted with an aperture that blocks the background radiation from the blackbody chamber without limiting the field of view of the ACR aperture. Complete isolation of the ACR chamber is achieved, if necessary, by a shutter in front of the isothermal plate that can be operated by remote control. The shutter is thermally anchored to the isothermal plate with a flexible copper braid. The temperature of the isothermal plate and shutter are monitored by three precision silicon diode thermometers. The isothermal plate is controlled to 0.05 K by using an integral heating element and the temperature is held at 22 K.

3.2 Measurements

Figure 2 shows the calibration setup inside the LBIR chamber. Blackbody sensor data and radiant power data are collected at each blackbody temperature and aperture setting specified by the customer. Data are collected and recorded at approximately one second intervals for a period of three minutes at each setting. These data form the basis for estimating the repeatability of the instrumentation. Cryogenic preparation of the ACR and the complete calibration sequence are repeated on three different days to test the reproducibility of the entire measurement system.

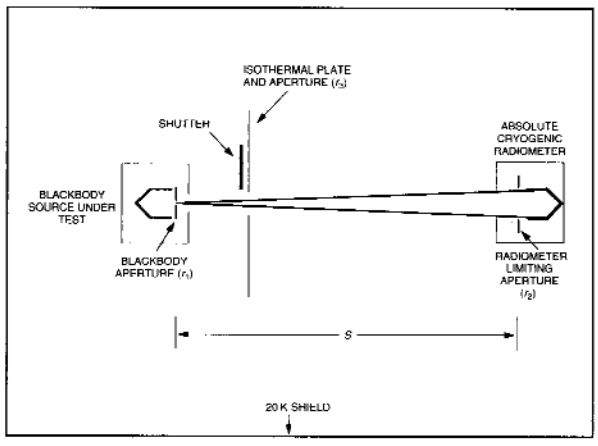

Fig. 2. Blackbody calibration setup inside the LBIR chamber.

3.2.1 Blackbody Temperature Sensors The blackbody temperature is generally measured by platinum resistance thermometers (PRTs) mounted on the blackbody core. Voltages across the PRTs measured by a multimeter, and currents supplied by a constant current source are converted to resistance values using Ohm's law. The resistances are converted to temperature values if the customer provides data on the calibration of the PRT sensors. Nominal settings on the external temperature control electronics of the BB and measured temperatures for the BB sensors are shown in columns 1, 2, and 4 of Table 1. Experimental standard deviations from the 1 s repetitions at each setting on each day are shown in columns 3 and 5 of the same table.

3.2.2 Radiant Power The radiant power at the ACR aperture is measured as follows: The radiation from the blackbody is blocked from the ACR receiver by using the shutoff position on the blackbody aperture wheel (if available). The electrical heater power to the ACR receiver is set to a value higher (preferably 20% to 30%) than the expected radiant power from the blackbody so that the temperature controller servo (ac bridge) can maintain a constant temperature at the ACR cone by varying the amount of electrical power. Preliminary estimates of radiant power at the ACR aperture are made using the Stefan-Boltzmann law and the approximate distance between the ACR aperture and the blackbody aperture. After the ac bridge is balanced, the ACR is allowed to receive the blackbody radiation by turning the aperture wheel to a chosen aperture position. If the customer blackbody is equipped with a fixed aperture, the 152 mm (6 in) shutter in front of the isothermal plate is used for blocking the blackbody radiation. The difference between the initial electrical power setting with the shutter closed and the final electrical power setting with the shutter open is the radiant power at the ACR aperture. Data is taken continuously at one second intervals for at least 3 min with the shutter open, in order to determine the repeatability of the instrumentation.

3.2.3 Geometry The measurement of the radius of the blackbody aperture, r_1 (see Fig. 2), corrected for thermal contraction at 20 K, is supplied by the customer. The radius of the ACR aperture, r_2, has been measured by the Precision Engineering

Table 1. Experimental data

Nominal (K)	Sensor 1 (K)	Std. dev. (K)	Sensor 2 (K)	Std. dev. (K)	Measured power (nW)	Average power (nW)	Std. dev. of average (nW)
200	199.897	0.002	199.281	0.002	71.9	71.5	0.5 (0.6%)
	199.874	0.005	199.332	0.005	72.0		
	199.947	0.002	199.328	0.003	70.6		
225	224.780	0.003	224.266	0.004	113.5	113.3	0.1 (0.1%)
	224.728	0.003	224.276	0.006	113.4		
	224.823	0.004	224.306	0.004	113.0		
250	249.662	0.004	249.268	0.004	171.3	172.0	0.4 (0.2%)
	249.639	0.007	249.288	0.008	172.6		
	249.733	0.005	249.322	0.004	172.2		
275	274.685	0.003	274.408	0.002	252.6	252.5	0.2 (0.1%)
	274.644	0.006	274.394	0.007	252.2		
	274.719	0.006	274.443	0.004	252.8		
300	299.531	0.007	299.329	0.007	358.4	358.0	0.4 (0.1%)
	299.521	0.003	299.346	0.004	357.3		
	299.588	0.005	299.389	0.004	358.4		
325	324.412	0.005	324.346	0.006	497.6	494.6	1.4 (0.3%)
	324.457	0.005	324.375	0.005	492.8		
	324.446	0.003	324.379	0.004	493.4		
350	349.306	0.003	349.378	0.003	665.8	664.8	0.8 (0.1%)
	349.337	0.008	349.395	0.011	663.7		
	349.445	0.006	349.479	0.006	664.8		
375	374.047	0.005	374.284	0.005	882.2	878.3	2.0 (0.2%)
	374.069	0.003	374.292	0.003	875.7		
	374.171	0.006	374.377	0.007	877.0		
400	399.026	0.005	399.362	0.005	1138.0	1137.1	1.3 (0.1%)
	399.056	0.004	399.379	0.004	1134.6		
	399.131	0.004	399.444	0.003	1138.8		

Division at NIST at room temperature in three different orientations. The average radius is corrected for thermal contraction as explained in Ref. [1].

The distance, S, between the blackbody aperture and the ACR limiting (precision) aperture is measured in two parts. The user measures the distance between the blackbody aperture and the front surface of a reference tab on the blackbody mounting plate as required by NIST [3], and NIST personnel measure the distance from the front surface of the tab to the ACR aperture. The chamber measurement is assisted by a Kaman proximity sensor [4] located internally to determine the final location of the reference tab to the ACR aperture before the chamber is evacuated. The measurements are made at ambient temperature and corrected for thermal contraction due to cooling of the chamber and the ACR to 20 K and 2 K, respectively. The radius of the aperture in the isothermal plate, r_3, shown in Fig. 2, is chosen to limit the background flux from the blackbody front surface. However, it will allow the full cone of light from the blackbody aperture to reach the ACR aperture. The geometrical measurements for the BB are given in Table 2.

3.2.4 Radiance Temperature The following equation deduced from the Stefan-Boltzmann law is used to convert the radiant power to radiance temperature, T:

$$T = \left[\frac{P}{F_1 A_1 \sigma_M}\right]^{1/4} \tag{1}$$

where

$$F_1 = (1/2)\,[z - [z^2 - 4x^2 \cdot y^2]^{1/2}]\,,$$

$$x = \frac{r_2}{S},\ y = \frac{S}{r_1},\ z = 1 + (1 + x^2)\,y^2,$$

Table 2. Geometric data for BB calibration

	Meas. value	Std. dev. mean
1. Radius (r_2) of the ACR aperture at 2.2 K	1.4971 cm	5×10^{-5} cm
2. Distance between the apertures (S)	30.77 cm	0.042 cm
3. BB aperture radius (r_1):		

Nominal mm	Measured at ambient mm	Deduced 20 K mm	Std. dev. mean mm
0.325	0.3251	0.3244	0.0013

and $A_1=\pi r_1^2$ is the area of the blackbody aperture; P is the radiant power and σ_M is the Stefan-Boltzmann constant, and equal to 5.67051×10^{-8} W m^{-2} K^{-4}. The expression for the configuration factor, F_1, given above is taken from Ref. [5] and to a first order approximation reduces to $\pi r_2^2/S^2$. The quantities r_1, r_2, and S have already been defined, and their measured values at room temperature are adjusted to cryogenic temperatures using the standard reference data for contraction of materials [6].

3.3 Analysis

3.3.1 Diffraction Correction It has been established in the literature [7, 8] that the radiation from the blackbody incident at the ACR aperture will not be solely determined according to geometrical optics because of diffraction effects at both limiting and nonlimiting apertures in the beam path. Therefore, diffraction losses at each one of the apertures in the beam path are estimated by using the procedures published in Refs. [7] and [8]. The measured radiant power values and the deduced radiance temperatures are corrected for the total diffraction loss which is a product of the fractional losses at each aperture in the beam path. The calculated correction factors ($\Delta P/P$) given as a percentage of the measured power values for the BB are listed in Table 3 for various temperatures. The corresponding correction factor ($\Delta T/T$) for the radiance temperature is approximately 1/4 of the correction ($\Delta P/P$) for the radiant power.

Table 3. Calculated diffraction correction (ΔP) given as a percentage of the measured radiant power (P). Systematic uncertainty (Type B) in the correction due to approximations in the calculations is ±10% of $\Delta P/P$.

Nominal blackbody temp. (K)	Diff. corr. $\Delta P/P$	Uncer. (1 σ)
200	1.3%	±0.13%
225	1.2%	±0.12%
250	1.1%	±0.11%
275	1.0%	±0.1%
300	0.9%	±0.09%
325	0.8%	±0.08%
350	0.8%	±0.08%
375	0.7%	±0.07%
400	0.7%	±0.07%

3.3.2 Measurement Uncertainties The uncertainties in the measurements are analyzed according to guidelines under development by the International Organization for Standardization (ISO) [9]. Uncertainties are caused by either systematic or random effects. Uncertainties from systematic effects (here after called systematic uncertainties for simplicity) are of the following types for this experiment: 1) uncertainties in theoretical corrections applied to measured data such as the uncertainties associated with the diffraction corrections; 2) uncertainties in the measured values of parameters that remain constant during the calibration. Examples of such uncertainties are the parameters that characterize the ACR response [1] which do not change during the ACR power

measurements. These uncertainties are Type B uncertainties according to Ref. [9] Subclause 3.3.3. Uncertainties from random effects (hereafter called random uncertainties for simplicity) arise from the statistical variation in the measurements during the calibration experiment. This type of variation is inherent in the blackbody PRT sensor measurements of temperature and the ACR measurements of radiant power during the calibration experiment. These are Type A uncertainties [9].

Uncertainty in Radiant Power

The uncertainty in the ACR measurement of the radiant power is analyzed as follows: For each nominal temperature, radiant power data (P_i) are collected every 1-1/2 s for approximately 3 min, leading to approximately 120 data points. An average, $\bar{P}$, and standard deviation, s_{rpt}, are calculated from this data. The standard deviation, s_{rpt}, is a measure of the repeatability of the measurements in each set, and in general, the ACR data show very good repeatability. The measurement process is repeated three different times to estimate a standard deviation, s_{rpr}, for reproducibility. The average over the three runs is calculated as:

$$\bar{\bar{P}}=\frac{1}{3}\sum_{j=1}^{3}\bar{P}_j$$

a standard deviation (s_t) is calculated from

$$s_t^2=\sum_{j=1}^{3}(\bar{P}_j-\bar{\bar{P}})^2/2\,. \tag{4}$$

The standard deviation (s_t) is a measure of both repeatability and reproducibility of measurements [10] according to

$$s_t^2\approx s_{rpr}^2+s_{\mathrm{rpt}}^2/120\,. \tag{5}$$

Although more repetitions of the entire measurement process would be desirable for better statistics, time constraints limit the number of repetitions. The radiant powers, $\bar{P}_j$, and the average powers, $\bar{\bar{P}}$, for the BB are given in columns 6 and 7, respectively, of Table 1. The standard deviations of the means, $s_t/\sqrt{3}$, are given in column 8.

Two sources of systematic uncertainty are evaluated as Type B following Ref. [9]. The standard uncertainty (i.e., 1 σ level) in the diffraction correction to the measured radiant power is based on diffraction theory used to calculate the correction. This standard uncertainty is estimated to be $\pm 10\%$ [7, 8] of the calculated correction based on scientific judgment (Sec. 4.6 Ref. [11]), as shown in column 3 of Table 3 for the BB. The standard uncertainty in the characterization of the radiometer as given in Ref. [1] is 0.12% of the measured radiant power. The standard uncertainty due to systematic effects is then the square root of the sum of the squares of the two components.

The random and systematic uncertainties are listed separately in the calibration report. The combined standard uncertainty (u_c) is reported as the square root of the sum of the squares of all of the components. However, it should be noted that other methods of combining components of uncertainty from systematic and random effects are in practice for calculating the total uncertainty [12]. Therefore, all components of uncertainty are listed to give the customer the choice of using an alternative method.

The radiant power data from Table 1 after correction for diffraction loss are shown in column 6 of Table 4. The uncertainty components associated with the average power are shown in columns 7 and 8, and the combined standard uncertainty, u_c, is given in column 9.

Uncertainty in the Blackbody Sensor Data

The Type A (random) uncertainty in the blackbody PRT sensor data is analyzed as follows: The PRT sensor data are collected in conjunction with the ACR power measurements. In general, the standard deviations for the PRT sensor data are homogeneous and negligibly small. Repeated sets of data are averaged to obtain the mean and the corresponding standard deviation analogously to the method discussed earlier for the ACR power measurements. The mean temperature values of the BB with associated standard deviations are shown in columns 2 through 5 of Table 4.

Radiance Temperature and Calibration Uncertainty

The final radiance temperatures for the calibration report are obtained by the least-squares analysis of temperatures, T_{ij} ($i=1,\ldots,n$; $j=1,\ldots,3$), deduced from Eq. (1), as a function of blackbody sensor readings, X_{ij} ($i=1,\ldots,n$; $j=1,\ldots,3$), for each aperture setting.

In order to evaluate a confidence band for the variability of the calibration curve, the following statistical procedure is adopted. The calibration equation is assumed to follow the model

$$T_{ij}=a_0+a_1X_{ij}+a_2X_{ij}^2+a_3X_{ij}^3+\ldots.+a_kX_{ij}^k+\epsilon_{ij}, \tag{6}$$

Table 4. Average blackbody sensor data and radiant power corrected for diffraction effects at the ACR aperture for the BB

Nominal (K)	Sensor 1 data (K)	Std. dev. (K)	Sensor 2 data (K)	Std. dev. (K)	Average power nW	Syst. uncer. nW	Random uncer. nW	Comb. uncer. u_c (1 σ) nW
200	199.906	0.003	199.313	0.003	72.4	0.1	0.5	0.5 (0.6%)
225	224.777	0.003	224.282	0.004	114.6	0.2	0.1	0.2 (0.2%)
250	249.678	0.005	249.293	0.005	173.9	0.3	0.4	0.5 (0.3%)
275	274.683	0.005	274.415	0.005	255.0	0.4	0.2	0.5 (0.2%)
300	299.547	0.005	299.355	0.005	361.2	0.5	0.4	0.6 (0.2%)
325	324.429	0.005	324.367	0.005	498.6	0.7	1.4	1.6 (0.3%)
350	349.362	0.006	349.429	0.007	669.8	1.0	0.8	1.3 (0.2%)
375	374.120	0.005	374.331	0.005	884.5	1.2	2.0	2.3 (0.3%)
400	399.071	0.005	399.395	0.004	1144.6	1.6	1.3	2.1 (0.2%)

where $a_0, \ldots, a_k$ are to be estimated, and ϵ_{ij}, the random errors associated with the measurements T_{ij}, are assumed to be independent with heterogeneous variances σ_{ij}^2. The σ_{ij} are estimated by s_{ij} from approximately 120 data points for each run. Weighted least squares [13] accounts for the heterogeneity of variances where the weights, w_i, are calculated from the empirical variances by

$$w_{ij} = 1/s_{ij}^2 . \tag{7}$$

The standard deviations associated with the T_{ij} are an order of magnitude larger than the standard deviations associated with the X_{ij} data, and, therefore, random uncertainties associated with the measurements X_{ij} are assumed to be negligible for the purpose of the least squares analysis. The degree, k, for the polynomial in Eq. (6) is determined by a goodness-of-fit test [14] which compares the agreement among groups of three runs with the overall fit to the data. The lowest degree polynomial which satisfies the goodness-of-fit criterion is taken as the calibration curve.

Given a future blackbody sensor setting, X_h, its calibrated radiance temperature value is given by

$$T_h = a_0' + a_1' X_h + a_2' X_h^2 + a_3' X_h^3 + \ldots + a_k' X_h^k , \tag{8}$$

where $a_0', \ldots, a_k'$ are least-squares estimates from calibration data. The random component of uncertainty associated with the predicted value is computed as

$$U_{\text{random}} = [(k+1)\, F\,(95; k+1, n-k-1)]^{1/2}\, s(T_h) . \tag{9}$$

The constant $F(95; k+1, n-k-1)$ is the upper 95 percentile of Snedecor's F-distribution with $k+1$ degrees of freedom in the numerator and $n-k-1$ degrees of freedom in the denominator, and $s(T_h)$ is the standard deviation of the predicted value, T_h. This uncertainty, based on the Working-Hoetelling confidence bands for the calibration curve, is valid for all future applications of the calibration curve as long as the model holds [15]. The details of the statistical analysis can be found in Ref. [15, 16]. A software package, OMNITAB [17], is used for the statistical computations.

Data for the least-squares analysis of the BB are shown in Table 5. Temperature as measured by PRT sensor 1 is used as the independent variable, X. The analysis confirms that a linear function ($k=1$) is sufficient for describing the data, and the following equation

$$T_h = a_0' + a_1' (X_h) \tag{10}$$

gives the predicted radiance temperature (T_h) for a blackbody temperature (X_h) measured by PRT

Table 5. Data for the least-squares analysis of the BB

Nominal (K)	Sensor 1 (K) X	Radiance temperature (K) T	Standard deviation (K) s	Weight W
200	199.897	201.427	3.500	0.0798
	199.874[a]	201.539[a]	1.420	0.4957
	199.947	200.546	2.130	0.2203
225	224.780	225.736	2.990	0.1116
	224.728	225.666	1.384	0.5224
	224.823	225.506	1.975	0.2564
250	249.662	250.135	2.100	0.2278
	249.639	250.593	1.166	0.736
	249.733	250.463	1.865	0.2875
275	274.6849	275.575	1.102	0.8239
	274.644	275.466	1.319	0.5751
	274.719	275.605	1.101	0.8244
300	299.5309	300.683	0.715	1.9545
	299.5211	300.462	1.135	0.7760
	299.588	300.683	0.887	1.2702
325	324.412[a]	326.342[a]	0.830	1.4529
	324.457	325.600	0.603	2.7502
	324.446	325.658	1.076	0.8641
350	349.306	350.931	0.644	2.4084
	349.337	350.657	0.997	1.0056
	349.445	350.807	0.869	1.3233
375	374.047[a]	376.500[a]	0.660	2.2930
	374.069	375.766	0.816	1.5003
	374.171	375.915	1.467	0.4647
400	399.026	401.171	0.872	1.3164
	399.056	400.866	1.266	0.6242
	399.131	401.240	1.217	0.6748

[a] Data with standardized residuals from the linear fit exceeding 2.5. These outliers are not included in the final analysis.

sensor 1. The estimated coefficients and associated standard deviations are:

$$a_0' = -1.096;\ s(a_0') = 0.244$$

$$a_1' = 1.007;\ s(a_1') = 0.001\ .$$

The percentage uncertainty in the deduced radiance temperature, $\delta T/T$, is given by Eq. (1) and the theory of uncertainty propagation [18]. An approximation on a Taylor series expression gives the relationship between the variables as

$$\delta T/T \sim \delta P/4P + \delta r_1/2r_1 + \delta r_2/2r_2 + \delta S/2S\ . \qquad (11)$$

The first term on the right hand side of Eq. (11) shows the relationship to the contribution from the uncertainty in the radiant power which has both Type A and Type B components as discussed above. The last three terms in Eq. (11) show the relationship to the contributions from the uncertainties in the measurement of the geometrical quantities, r_1, r_2, and S. A summary of the percentage uncertainties in the geometrical measurements (Table 2) and their propagated uncertainties for radiance temperature measurements are given in Table 6.

The predicted NIST radiance temperature from the calibration equation for each average value of temperature measured by PRT sensor 1 is given in Table 7 for the BB calibration. The uncertainty

Table 6. Uncertainties in the measurements of geometrical quantities for the BB

Quantity	Uncertainty in measurement (1 σ)	Propagated uncer. for temperature measurement (1 σ)
1) Distance between apertures ($\delta S/S$)	0.136%	0.068%
2) Radius of ACR aperture ($\delta r_2/r_2$)	0.003%	0.002%
3) Radius of BB aperture ($\delta r_1/r_1$)	0.2%	0.1%
	Total[a]	0.12%

[a] Square root of sum of squares of 1, 2, and 3 given above.

Table 7. Predicted radiance temperatures and uncertainties for BB

Nominal	Sensor 1 data	Predicted radiance temp	ACR char.	Systematic uncertainties			1 σ *random* uncertainties	Expanded uncer. (U)
				Geometry meas.	Diff. cal.	Total b		
	(K)	(K)	(K)	(K)	(K)	(K)	(K)	(K)
200	199.906	200.3	0.06	0.24	0.07	0.25	0.10	0.7 (0.4%)
250	224.777	225.4	0.07	0.26	0.07	0.28	0.08	0.7 (0.3%)
250	249.678	250.4	0.08	0.30	0.08	0.32	0.07	0.7 (0.3%)
275	274.683	275.6	0.09	0.33	0.05	0.35	0.05	0.8 (0.3%)
300	299.547	300.7	0.09	0.36	0.06	0.38	0.04	0.8 (0.3%)
325	324.429	325.8	0.10	0.39	0.07	0.41	0.04	0.8 (0.3%)
350	349.362	350.9	0.11	0.42	0.07	0.44	0.04	0.9 (0.3%)
375	374.120	375.8	0.11	0.45	0.08	0.47	0.05	1.0 (0.3%)
400	399.071	400.9	0.12	0.48	0.08	0.5	0.07	1.0 (0.3%)

components due to systematic effects are listed separately based on Eq. (11): 1) the uncertainty in the power $\delta P/4P$, due to the characterization of the ACR as an absolute detector [1] is listed in column 4; 2) the uncertainty in defining the geometry as given in Table 6 is shown in column 5; and 3) the uncertainty in diffraction calculations due to approximations is shown in column 6. The total systematic component, b, which is the root sum of squares, is given in column 7. The Type A component, $s(T_h)$, of the uncertainty is obtained from least-squares analysis, and the expanded uncertainty, U, as shown in column 9, is obtained by expanding Eq. (9) as follows [19]:

$$U = [(k+1)\,F(95;\,k+1,\,n-k-1)]^{1/2}$$
$$[s^2(T_h) + \mathrm{b}^2]^{1/2}\,. \qquad (12)$$

The multiplying factor in Eq. (12) for $n = 27$, $k = 1$ for the BB experimental data is 2.6. The value shown in parenthesis in column 9 is the expanded uncertainty given as a percentage of the measured temperature.

The statistical procedure that leads to Eq. (12) did not take into account possible correlations between Type B uncertainties because of the relationship between variables shown in Eq. (11). However, calculations of expanded uncertainty, U, using the complete covariance matrix and least square fitting using appropriate weights have been carried out and the results are found to be the same as given by Eq. (12). The calibration constants in Eq. (10) also are found to be essentially same as reported earlier.

Figure 3 shows the temperature value from PRT sensor 1 plotted on the X-axis and the measured radiance temperatures (Table 5) and corresponding

predicted radiance temperature (Table 7) on the Y-axis. The solid line in Fig. 3 connects the predicted radiance temperature values and represents Eq. (10). Figure 4 shows the 95% confidence band for the difference between the calibrated temperature and the PRT temperature. The expanded uncertainty given in Table 7 is within 0.5%.

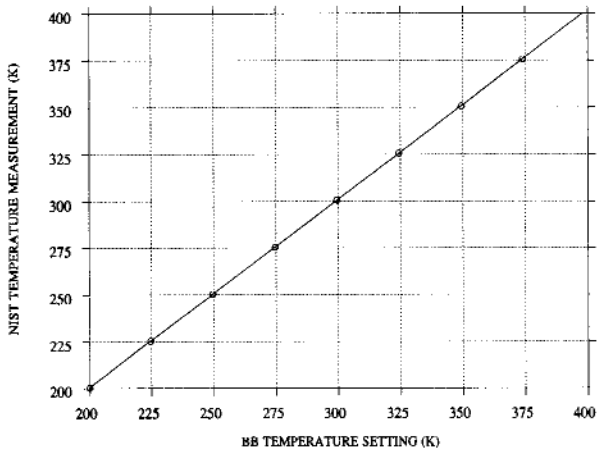

Fig. 3. Measured temperatures and calibrated radiance temperature from polynomial fit plotted as a function of blackbody temperature setting using PRT sensor 1.

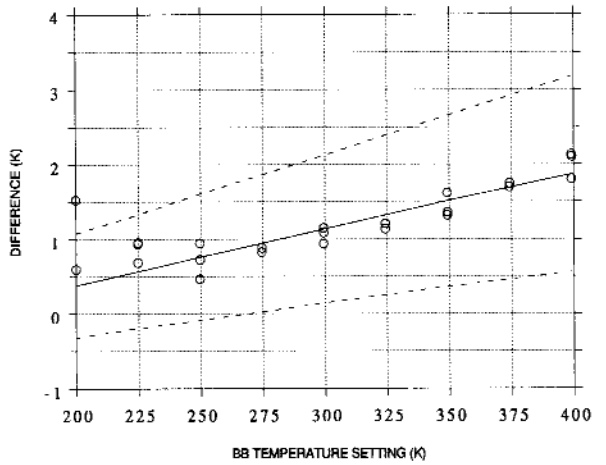

Fig. 4. Solid line: Difference between the deduced radiance temperature and the temperature measured by the blackbody PRT sensor 1 plotted as a function of blackbody temperature setting. The points represent the same for measured radiance temperatures and are not all of equal weights. Dashed lines: Upper and lower bounds of 95% confidence bands.

However, it is always an open question why for example, at the nominal blackbody temperature of the 400 K does the temperature sensor 1 measure 399.071 K whereas the radiance temperature is 400.9 K as shown in Table 7. The calibration curve does not address the effects of systematic errors such as unaccounted scattered light entering the ACR, aperture warming of the blackbody etc. However, experimental designs to eliminate such systematic effects are planned and implemented within the time allotted for customer calibrations. The experimental checks show these effects should be negligible. For future calibrations, spectral instrumentation is also being added to address this question further by measuring the emittance from the blackbody as a function of wavelength between 2 μm to 30 μm and comparing it with the currently assumed value of unity.

4. Summary

The LBIR facility is in operation for customer blackbody calibrations using the ACR as the absolute detector. The experimental procedure and analysis of data that generate the calibration report for the customer are described in detail, and a recent blackbody calibration at the facility serves as an example of the procedure. Calibration uncertainties in radiance temperatures of less than 1% have been realized for typical flux levels of 25 nW and above at the ACR aperture. Experimental procedures to reduce systematic uncertainties are continuously investigated and implemented to improve the accuracy of measurements. Future improvements of noise control in the ACR operation could allow measurements down to 10 nW at the ACR aperture with 1% uncertainty. Capability for measuring spectral emittance of customer sources in the 2 to 30 micrometer wavelength region is being developed.

Acknowledgments

The authors are indebted to S. Ebner and J. Proctor of NIST for their efficient operation of the LBIR instrumentation. We are also indebted to C. C. Hoyt and P. Miller of CRI, Inc., for giving effective training on the ACR operation.

About the authors: *Dr. Raju Datla, a physicist, is the group leader of the IR Radiometry Group of the Radiometric Physics Division at NIST. Ms. Carroll Croarkin is a statistician in the Statistical Engineering Division at NIST. Dr. Albert Parr, a physicist, is the Chief of the Radiometric Physics Division at NIST. The National Institute of Standards and Technology is an agency of the Technology Administration, U.S. Department of Commerce.*

Disclaimer

References made in this paper to particular brand names or specific suppliers of a service are made for ease of understanding by the reader and do not constitute an endorsement of products or service by the National Institute of Standards and Technology over other competitive suppliers of similar products or service.

5. References

[1] R. U. Datla, K. Stock, A. C. Parr, C. C. Hoyt, P. J. Miller, and P. V. Foukal, Characterization of an Absolute Cryogenic Radiometer as a Standard Detector for Radiant Power Measurements, Appl. Opt. **31**, 7219 (1992).

[2] IIT Research Institute, 10 West 35th Street, Chicago, IL 60616.

[3] S. C. Ebner, A. C. Parr, C. C. Hoyt, Imaging Infrared: Scene Simulation, Modelling, and Real Image Tracking; SPIE **1110**, 49 (1989).

[4] Kaman Instruments Corporation, 1500 Garden of the Gods Road, Colorado Springs, CO 80933-7463.

[5] C. L. Wyatt, Radiometric System Design, MacMillan, NY, (1987) pp. 37–38.

[6] A. F Clark, Thermal Expansion, Chapter 3 in Materials at Low Temperatures, P. R. Reed and A. F. Clark, eds., American Society for Metals (1983) p. 95.

[7] W. H. Steel, M. De, J. A. Bell, Diffraction Corrections in Radiometry. J. Opt. Soc. Amer. **62**, 1099 (1972).

[8] L. P. Boivin, Diffraction Corrections in the Radiometry of Extended Sources, Appl. Opt. **15**, 1204 (1976).

[9] ISO Guide to the Expression of Uncertainty in Measurement, prepared by ISO Technical Advisory Group 4 (TAG 4), Working Group 3 (WG 3) 1993.

[10] J. Neter, W. Wasserman, and M. H. Kutner, Applied Linear Statistical Models, Sec. Ed., Richard D. Irwin, Inc., Homewood, IL 60430 (1985) p. 539.

[11] B. N. Taylor and C. E. Kuyatt, Guidelines for Evaluating and Expressing the Uncertainty of NIST Measurement Results, NIST Technical Note 1297 (1993).

[12] Eisenhart, C., Precision Measurement and Calibration: Statistical Concepts and Procedures, H. H. Ku, ed., NBS Special Publication 300, Vol. I (1969).

[13] N. Draper and H. Smith, Applied Regression Analysis, Second Ed., Wiley & Sons, NY (1981) pp. 108–116.

[14] Reference [10] pp. 109–122.

[15] Reference [10] p. 154.

[16] M. G. Natrella, Experimental Statistics, John Wiley, NY (1966) ch. 5.

[17] S. T. Peavy, S. G. Bremer, R. N. Varner, and D. Hogben, OMNITAB 80: An Interpretive System for Statistical and Numerical Data Analysis, NBS Special Publication 701 (1986).

[18] H. H. Ku, Notes on the use of Propagation of Error Formulas, Precision Measurement and Calibration: Statistical Concepts and Procedures, H. H. Ku, ed., NBS Spec. Publ. 300, Vol. I (1969).

[19] K. Eberhardt, Staff member of NIST Statistical Engineering Division, (Private Communication).

Volume 99, Number 1, January–February 1994
Journal of Research of the National Institute of Standards and Technology

Conference Report

INTERNATIONAL CONFERENCE ON MACHINING OF ADVANCED MATERIALS Gaithersburg, MD July 20–22, 1993

Report prepared by

Said Jahanmir

Ceramics Division,
Materials Science and Engineering Laboratory,
National Institute of Standards and Technology,
Gaithersburg, MD 20899-0001

1. Introduction

Advanced materials, such as ceramics and composites, are the building blocks of technology; but the high cost associated with their machining and finishing is a major barrier to the use of these materials in commercial applications. In some cases, current machining methods cannot be used and innovative techniques or modifications of existing methods are needed. The development of new machining technologies for advanced materials requires interdisciplinary research and collaboration between industry, government, and universities. The International Conference on Machining of Advanced Materials was held at the National Institute of Standards and Technology, Gaithersburg, Maryland on July 20–22, 1993 to strengthen communication and technology transfer among researchers and engineers involved in machining of advanced materials. This conference was cosponsored by the National Institute of Standards and Technology—Ceramics Division, the National Science Foundation—Materials Processing and Manufacturing Program, and the U.S. Navy—Manufacturing Technology Program. The conference was endorsed by the American Society of Mechanical Engineers, the American Ceramic Society, and Ceramic Industry Magazine.

The conference was attended by more than 250 people from 12 different countries representing industry, government, and universities. More than 56 percent of the attendees were from industry. A total of 64 presentations were made at the conference. A highlight of the conference was a presentation by Dr. John McTague, Vice President of Ford Motor Company, who stressed the importance of government/industry cooperation in research and technology development.

2. Conference Summary

To accommodate the large number of papers without having parallel sessions, the papers were divided into oral presentations and posters. In addition to the 48 papers contained in the proceedings (published as NIST Special Publication 847), 16 other presentations were made without publication. The following is a summary of the papers included in the proceedings.

2.1 Grinding of Technical Ceramics

The topics covered in this section included both experimental evaluation and theoretical modeling of the grinding process. A new technique, "helical scan grinding," was described for obtaining a high

degree of surface finish even with a wheel containing coarse diamond grit. The performance of single-layer diamond abrasive tools was evaluated in another paper to develop guidelines for the design and implementation of these tools for grinding of ceramics. An electro-discharge trueing operation was described for metal-bonded diamond grinding wheels to achieve a higher grinding ratio and lower grinding forces than conventional means of trueing. A new Technique, based on self-sharpening of the diamond wheels, was presented for increasing the material removal rate during grinding of ceramics. The controlling effect of grinding fluids on the material removal process was described and a new additive was proposed for improving the drilling rate of alumina ceramics by diamond abrasive drills. One of the papers emphasized the importance of a systems approach in grinding of ceramics. In this approach, the machine tool, diamond wheel, work material, operational factors, and cost of the machining cycle were examined to design cost-effective production processes for ceramic grinding. A simple model was presented relating grinding forces to the operational parameters in grinding. The basic process of grinding was modeled analytically by describing the stress field caused by sliding microindentation of brittle materials. The papers in this section presented information on grinding of alumina, silicon nitride, silicon carbide, tungsten carbide, zirconia, and alumina fiber-reinforced composites.

2.2 Characterization of Machined Surfaces

Nondestructive techniques were described for the characterization of surface roughness and machining-induced subsurface damage in ceramics. In one paper, a sharply focused ultrasonic transducer was used to generate short-duration pulses for the detection of subsurface damage in silicon nitride. In a second paper, the surface morphology of ultrasonically machined glass, alumina, and zirconia were evaluated by surface profiling and scanning electron microscopy to determine the material removal process. An indentation technique was used to measure the residual stresses in ground and polished soda lime glass, Ni-Zn ferrite, and silicon nitride, and the results were compared with x-ray diffraction measurements. Optical scattering methods were successfully applied to detect subsurface defects in ground and polished silicon nitride samples. As an in-process method, acoustic emission sensors were used to detect chatter and surface patterns in cylindrical grinding.

2.3 Effect of Grinding on Strength

The effects of grinding-induced damage on strength and surface quality of silicon nitride, alumina, and other types of ceramics and ceramic composites were reported. The effects of cutting speed, depth of cut, diamond grit size, grinding direction, ceramics grain size and microstructure on strength were evaluated in several papers. Also, the relationships between grinding parameters and residual stress were determined by x-ray diffraction. It was shown that the magnitude of compressive residual stress in silicon nitride increases as the chip thickness is increased in grinding. The bending strength of various ceramics was shown to be dependent on the grinding direction with respect to the direction of the tensile axis. The strength of samples ground in the longitudinal direction (i.e., parallel to the tensile axis) did not depend on the grinding condition, even when the removal rate was increased by a factor of 60. However, the strength of samples ground in the transverse direction (i.e., perpendicular to the tensile axis) was affected by the parameters used in grinding. The magnitude of the strength in the transverse direction was generally lower than the samples ground in the longitudinal direction. However, the reduction in strength was related to the specific grinding conditions used and the ceramic microstructure, such as the grain size. It was also reported that the specific grinding energy is a function of ceramic grain size.

2.4 Precision Machining

The papers in this section were focused on both single-point diamond turning and "ductile" regime precision grinding. The wear mechanisms on the diamond tools used in single-point cutting were found to be primarily controlled by solid state diffusion rather than abrasion. Micro-Raman spectroscopy was used to determine the residual stresses in germanium crystals machined by single-point turning. A new design concept for ultra-precision grinding machines with vertical spindles was proposed for "ductile" regime grinding of ceramics. Several papers described new methods for trueing and dressing of diamond wheels for the generation of precision aspheric surfaces. The electrolytic in-process dressing technique was reviewed in particular and some recent results were presented. Two papers showed that "ductile" regime grinding can improve the surface finish and strength of silicon nitride components if the machining-induced damage from rough grinding is removed.

.5 Free-Abrasive Machining

Free-abrasive machining refers to the processes /here material is removed by loose-abrasive parti-les. The ultrasonic machining process was evalu-ted for machining of feldspathic porcelain (a lental ceramic material). It was found that the)ending strength and fatigue resistance were im-)roved by ultrasonic machining as compared to :onventional grinding and lapping techniques. An :nergy-based model was proposed for cutting of :arbon-reinforced polymer composites by water jet ınd abrasive water jet machining. Two papers were 'ocused on new concepts for polishing. In one)aper, mechanochemical polishing of silicon ıitride was achieved by incorporating chromium)xide particles into the grinding wheel. In the second paper, a magnetic-abrasive finishing technique was effectively used to polish tungsten carbide.

2.6 Turning and Milling

Conventional techniques of turning and milling are routinely used for fabrication of metallic materials; however, their use for advanced materials is limited to "softer" ceramics, metal-matrix composites, and polymeric composites. Machining of advanced materials is often difficult and requires development of new cutting tools and machining porcedures. In one paper, the machining processes used for ceramic dental restoration materials were reviewed; and statistical design of experiments was shown to be an effective means for the optimization of the machining process with respect to the surface roughness and removal rate. In another paper, the machinability of several dental materials, such as glass-ceramics, lucite-reinforced ceramics, dental hybrid composites, and hydroxyapatite, were evaluated with respect to surface quality. Several types of aluminum-matrix composites containing ceramic reinforcements were machined by turning to select suitable cutting tool materials. It was found that deposition of a diamond film on a silicon nitride tool gives the lowest wear rate among all the tool materials and coatings tested. In a similar study, performance of different tool materials, such as cemented carbide, alumina composites, sialon, cubic boron nitride, and polycrystalline diamond, were evaluated for machining of carbon and glass fiber-reinforced phenolic resin composites. The mechanisms of tool wear in turning of fiber-reinforced polymers were studied with both plain and coated cemented carbide tools. The performance of polycrystalline cubic boron nitride tools was also reviewed for machining of hard steels. Turning was applied to alumina ceramics using a polycrystalline diamond tool. An analysis of the surface indicated that although the surface contained a few residual microcracks, the surface roughness was within an acceptable range for most applications. In one paper, a new laser-assisted, hot-machining process was proposed for turning and milling of ceramics. In this experimental process, the laser beam is used to heat and soften the material just ahead of the cutting zone to reduce the cutting forces.

2.7 Laser and Electrical Discharge Machining

The application of pulsed lasers in machining of advanced materials was reviewed in this section. The influence of heat-affected layers and residual stress on fracture strength of finished test samples was evaluated. It was shown that the fracture strength of laser-processed silicon nitride ceramics was lower by 10 to 20 percent compared with ground samples. The process of material removal in laser machining of silicon nitride was shown to be dissociation and oxidation of silicon nitride. The finished surfaces were found to contain porosity, an oxidized layer, and a heat-affected zone which reduced the surface quality and strength. It was reported that although laser processing of ceramics cannot be used alone to finish advanced ceramics, it can be used as a complementary process to conventional diamond grinding, especially in high-speed cutting of complicated shapes and geometries. Electrical discharge machining as applied to ceramics and polycrystalline diamond was reviewed. It was shown that several ceramics such as titanium diboride, boron carbide, and several composites containing nitrides, carbides, and borides can be cut by electrical discharge machining. Machined surfaces were examined to assess the material removal mechanisms and surface quality.

3. Future Conference

Based on the comments made by attendees, this conference was successful in achieving its goal, which was to strengthen communication and technology transfer among researchers and engineers involved in machining of advanced materials. Many participants suggested that the conference be held on a regular basis. Following discussions with the Conference Advisory Committee it was tentatively decided to hold the Second International

Conference on Machining of Advanced Materials in Germany in 1996. If this conference is successful, the next conference will be held in Japan. Then, plans will be made to rotate the conference every 2 years between the United States, Germany, and Japan.

4. For More Information

Copies of the Conference Proceedings are available through the National Technical Information Service (NTIS), Springfield, VA 22161. The following information should be used when ordering this item from NTIS: Machining of Advanced Materials, NIST/SP 847, PB93-217578/AS. Please indicate if you are ordering a hard copy (A23/$61.00) or a microfiche (A04/$19.50).

To obtain more information about the next conference, or to be placed on the mailing list, write to Said Jahanmir, National Institute of Standards and Technology, Building 223/Room A329, Gaithersburg, MD 20899-00001.

Volume 99, Number 1, January–February 1994
Journal of Research of the National Institute of Standards and Technology

Conference Report

WORKSHOP ON STANDARDIZATION NEEDS IN BIOTECHNOLOGY Gaithersburg, MD April 26–27, 1993

Report prepared by

Kenneth D. Cole and
Lura J. Powell

Biotechnology Division,
National Institute of Standards and Technology,
Gaithersburg, MD 20899-0001

and

G. Larry Eitel

Chair, Committee E-48 on Biotechnology,
American Society for Testing and Materials,
Wolder Engineers & Constructors,
Golden, CO 80401

1. Introduction

The National Institute of Standards and Technology, an agency of the U.S. Department of Commerce, Technology Administration in cooperation with the American Society for Testing and Materials (ASTM) Committee E-48 on Biotechnology held a workshop to determine the necessary standards to aid the rapidly growing biotechnology industry. As shown in Fig. 1, the number of U.S. biotechnology companies grew rapidly from about 100 in 1970 to over 1300 in 1992. The availability of standard methods for the industry fell behind this development curve. Most major biotechnology firms prepared their own procedures for testing in a fragmented approach to using standard procedures. This has handicapped some industry users and complicated the regulatory efforts to validate and qualify new drugs and products that use recombinant organisms in their manufacturing processes.

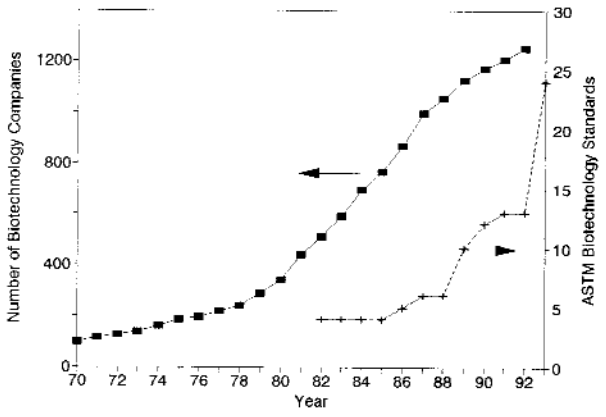

Fig. 1. Growth of U.S. biotechnology companies compared to the number of ASTM standards.

The ASTM Committee E-48 on Biotechnology was chartered in 1985 to develop test methods, specifications, classifications, practices, guides and terminology standards for the developing biotechnology industry. Where processes use living organisms, the E-48 scope of activity extends from identification and preservation of biological

materials, unit processes and their control, enviromental issues, and biomass conversion to validation of biological manufacturing processes.

ASTM Committee E-48 is a dynamic group of more than 100 volunteer scientists, engineers, manufacturers, researchers, government representatives and members of the private sector who develop voluntary consensus-based standards to promote appropriate technological development. The seven technical subcommittees of Committee E-48 and their topics are:

- Materials for Biotechnology: purity and contamination in biological drug products, characterization of proteins, quality control of culture media, synthetic DNA, and preservation methods for biological materials.
- Characterization and Identification of Biological Systems: test methods for plasmids, cell cultures, viruses, bacteria, fungi, and tissues.
- Unit Processes and Their Control: test methods and practices for aseptic sampling, membrane separation, bioleaching, biosensing, and manufacturing equipment performance.
- Environmental Issues: procedures to decontaminate biological process fluids and equipment, containment, safety equipment to avoid biomaterial losses.
- Biomass Conversion: test methods for wood materials, practices for evaluating fuel alcohol plant design and performance, practices for anaerobic/aerobic digesters.
- Biotechnology Equipment Qualification and Process Validation: test methods and practices for validating manufacturing processes and equipment, current good manufacturing practice guidelines for biological processes.
- Terminology: establishing standard terminology for biotechnology.

Over 30 standards have been developed and over 100 more are targeted for development during the next few years by qualified and experienced personnel in this field.

The Workshop on Standardization Needs in Biotechnology was designed to: (1) update industry participants on NIST and ASTM activities that will impact our industry and facilitate regulatory compliance, (2) identify and prioritize needs for consensus, voluntary standards and programs to develop technology, (3) organize resources to develop these voluntary standards, and (4) serve as a forum for industry, universities and government to discuss standards of mutual interest.

The workshop was opened by remarks by Larry Eitel, Chair of ASTM E-48 and Lura Powell, first Vice-Chair of ASTM E-48. The President of ASTM, James A. Thomas gave an overview of the ASTM consensus standardization process. Overviews of the NIST Biotechnology Program, the Standard Reference Materials Program and the Advanced Technology Program were presented. A panel discussion made up of representatives of government agencies discussed federal agency standard issues.

The workshop was then organized into seven workgroups that included: validation and current good manufacturing practices, the environment, characterization and preservation of living cells, safety and transport of biomaterials, bioprocess separations, agricultural/biomass, and microbiological diagnostics. Each workgroup considered the following aspects: a review of current standards, a review of areas where standards might be considered, identification of those areas where standards are needed, prioritization of the standards needs and identification of resources for developing and reviewing standards. The findings of the individual workgroups are presented in this report.

2. Validation and Current Good Manufacturing Practices

The validation and current good manufacturing practices workgroup was chaired by Victor Batista, Regional Validation Project Manager for Raytheon Engineers and Constructors. The reference documents (monographs, points-to-consider, guidelines, etc.) already written by professional organizations on validation were identified as a major issue. It was agreed that there is a need to organize and compile this information into a uniform source. The group came to a consensus that the standards should be documents that will be of practical use and have regulatory and scientific depth. Consensus definitions were developed for the three components of a qualification study. The first component is the installation qualification program that will evaluate the documentation (or references) against the system as installed. The second component is the operational qualification program that will provide testing of the system against design specifications and process requirements. The final component is the performance qualification that will provide a scientific study to demonstrate that a process or

product will consistently meet the predetermined specifications.

The workgroup decided that standards should contain the following components. An overview is necessary to indicate the purpose of the validation study as well as the data generated and how the information will be used. Installation requirements should contain a clear definition of the minimum criteria of the protocol format and sample forms. Operational and performance qualification documents should have a clear definition of the minimum criteria of the protocol format, sample forms and the objective and methodology for the applicable testing, inspection procedures and analytical tests. General acceptance criteria that contain the minimum requirements for defining predetermined specifications for the study in question should be part of the standard. Revalidation requirements are required for the type of equipment, system or process to be qualified. A points-to-consider section should anticipate possible variables affecting the qualification study. Sample forms for installation, operational and performance qualification requirements should also be included. Standard documents should contain references used in their development.

The members of the workgroup decided that specific standards need to be developed in the following areas.

A. Protocol preparation guidelines for installation, operational and performance qualifications need to be developed.
B. Summary report guidelines are needed.
C. Master project plan guidelines need to be developed.
D. Validation requirements used in the development of purchase or construction specifications are needed.
E. Qualification standards are needed for bottled gases, filtered air, potable water, deionized water, water for injection, chilled water, plant steam, clean steam, drainage, kill systems (decontamination), containment systems, classified air systems, heat vacuum air conditioning systems enviromental chambers, environmental monitoring systems, clean in place systems, steam in place systems, automated systems, process vessels, dry heat ovens, sterile filters, autoclaves, ultrafilters, bioreactors, microfiltration processes, incubators, programmable logic systems and chromatography equipment.
F. Software functional description guidelines requirements need to be developed.
G. Hardware specification guidelines requirements are needed.
H. Requirements are needed for software development and qualification.
I. Automated system guidelines are needed.
J. Cleaning validation requirement guidelines are needed.
K. Standards are needed for process qualifications.

3. Environment

John Burckle, Senior Research Engineer for the Risk Reduction Engineering Laboratory, Toxic Control Branch of the Enviromental Protection Agency (EPA) chaired the workgroup on industrial biosafety/enviromental aspects of large-scale use of genetically modified organisms and the release of such organisms into the environment. This workgroup concentrated on recently conducted research identified to support the EPA efforts in regulating manufacturing using genetically modified organisms and deliberate enviromental release of these organisms. This research helps to define the areas of standards and provide sufficient data so that standards can be considered. The chair and members identified the following areas as having equally high priority because of their impact on regulatory decision making and because they involve the release of genetically modified organisms to the environment.

A. Standards are needed for the methodology of assessing worker exposure to microorganisms in large-scale fermentation facilities. Recent investigations have shown that bioaerosol sampling technology to measure viable and nonviable organisms is inadequate. Basic issues such as which parameters to measure and the most appropriate methods need to be resolved.
B. Standards to determine the performance of kill tanks in large-scale facilities need to be resolved because of difficulties in sampling such facilities.
C. Guidelines are needed for the detection of genetically engineered microorganisms during field trials. There is a wide variety of test methods that can be used to detect genetically modified organisms. These methods need to be standardized to help facilitate

enforcement of current legislation and the development of test guidelines by federal agencies, such as the EPA.

D. There is an urgent need to standardize microcosm design and testing protocols for studying the survival and competition of genetically-modified organisms. This will allow the reliable testing of the survival of genetically-modified organisms and their effect on endogenous organisms before they are released into the environment.

E. Methods need to be developed to determine the extent of bioremediation by microorganisms. These methods should address preparation, sampling, sample transport, sample preservation, soil moisture, analysis and statistical design including control groups.

4. Characterization and Preservation of Living Cells and Viruses

Larry Bockstahler, Senior Research Biophysicist for the Molecular Biology Branch of the Food and Drug Administration chaired the workgroup on characterization and preservation of living cells and viruses. This workgroup was concerned with standards to characterize the large number of cells and viruses to ensure identity and detect genetic changes during propagation. Voluntary standards in the areas of characterization and preservation assist industrial and other biotechnological laboratories in sustaining high quality control of their products. This workshop reviewed the current standards, protocols and guidance documents for the characterization and preservation of cells and viruses and identified the following specific areas for standards needs in characterization.

A. Guides are needed for the cell line identification of mammalian cells based on results of a number of diagnostic tests. This area was given the highest priority. A general guide for polymerase chain reaction for the verification of inserted genes in transgenic animals is also needed.

B. In the area of viruses, a specific guide for bacteriophage ΦX-174 along with a draft standard for a new barrier leak testing method should be developed. General guidelines are needed for detecting enveloped RNA, nonenveloped RNA, enveloped DNA, and nonenveloped DNA virus categories. Guidelines for adventitious virus testing and co-cultivation are necessary to help meet Food and Drug Administration requirements and points-to-consider documents. General guidelines for viruses used in gene therapy such as retroviruses and adenoviruses should be developed.

C. In the area of bacteria, general standards are needed for "wild-type" industrial isolates used in genetic engineering, including the 10 most commonly used "wild-type" strains and for genetically-engineered bacteria used by the biotechnology industry. In addition, guidelines are needed for sterility testing of finished products of the biotechnology industry.

D. For plasmids, guidelines for data interpretation for restriction enzyme mapping of the DNA and determination of copy number to help meet FDA requirements were recommended.

E. General guidelines are needed for the identification of fungi used as expression systems in biotechnology.

F. A data base is needed for keeping track of the existing standards and to establish better communication between ASTM committee E48 and federal government agencies.

Preservation of living cells and viruses is key to the consistency and quality of biotechnology products and processes. The following specific needs were determined for the preservation section.

A. In the area of cell banking, standards are needed to assist users in validating the characterization and preservation processes to satisfy FDA requirements for cell banking. This area was given the highest priority in the preservation section.

B. Equipment for low-temperature storage of mammalian cells and inventory control and data management systems such as barcoding and ampule tracking need to be standardized.

C. Standards are needed for the proper packing and transport of frozen cells depending on if the use is immediate use or long term storage.

D. The banking of tissues from human and other sources requires standards.

E. Standards are necessary for safety issues with liquid nitrogen such as oxygen monitoring and ventilation systems.

F. Standards for raw material specifications for cryoprotectants and standardized certificates of analysis from vendors are needed.
G. The handling of specific hazardous materials during low temperature storage requires standards.

5. Safety and Transport of Biomaterials

Frank Simione, Associate Director for Operations at the American Type Culture Collection, chaired the workgroup on safety and transport of biological materials. Safety of biological materials includes their use, transport and disposal. Biological materials can pose safety considerations from their biological, chemical and radiological properties. Transport of biological materials are covered under existing guidelines and regulations but there is a need to improve and clarify the existing documents. The session chair and members identified these areas where standards are needed:

A. A safety action plan that considers specific safety issues for a particular product or process should be developed. This area was given the highest priority by the workgroup.
B. A general guide for transport standards that covers current regulations and procedures for packaging and shipping of biological materials should be developed. Specific standards would include standards for package performance testing, a guide for determining the level of hazard of an infectious substance and a guide for responding to infectious substances in an accident or during a spill.
C. Standard practices for handling hazardous waste are needed that include on site treatment of infectious waste, handling and segregation of chemical and radioactive waste should be developed. Guides are also needed for the treatment and reduction of chemical waste.

6. Bioprocess Separations

Gail Sofer, Director of International Validation Development at Pharmacia chaired the workgroup on bioprocess separations. The workgroup agreed that while standards are available from a number of organizations, it is not clear what standards are available and if there is an overlap of existing standards. The group identified the need by industry to consolidate and cross-reference existing standards into a data base. Better communications need to be established among the organizations currently developing standards. The workgroup discussed general guidelines that should determine when a standard is needed. These guidelines included a demonstrated need for a standard, quantitative standards must have a thorough statistical evaluation, standard analytical methods must exist and be validated and standards should not be misapplied or stretched.

General conclusions reached by members of the group were: (1) that the bioseparations area is not yet mature and standards should reflect this, (2) that each biotechnology process is unique and each process requires validation, and (3) that currently, there is not a high demand for standards, but as the industry matures, needs will increase and standards will have to be reviewed often.

The chair and members of the workgroup identified the following specific areas for standard needs.

A. Standards for materials classification, especially plastics, are needed. This area was given a high priority.
B. A database of existing and developing standards was also given high priority.
C. The existing ASTM standard on ultrafiltration membrane performance needs to be upgraded.
D. Guides for good development practices are needed.
E. Guides to fermentation process development are needed.
F. Filtration standards that include steam-in-place, pressure and cleaning standards and solution compatibility and leachates need to be developed.

7. Agriculture/Biomass Workgroup Session

James Walsh of the Enviromental and Technology Laboratory, Georgia Technology Research Institute chaired the agriculture/biomass workgroup. Agricultural and biomass processes generate large volumes of material that must be treated, recycled or disposed of. There is a great amount of interest in the use of agricultural and biomass materials as a renewable source of energy. Standards are necessary to determine the technical and economic performance of energy producing and conversion systems and to characterize feedstock and byproduct materials. Guidance is needed for the design and operation of these processes.

The chair and members of the workgroup have identified the following specific areas for standards needs.

A. Development of proposed standards for evaluation of biomass gasifiers should be completed and the terminology document should include definitions developed by the National Renewable Energy Laboratory (NREL).
B. A document on standard properties of biomass that could be used for process development to full scale systems should be developed. The document should include a comparison of data from several sources and a standard basis for evaluation of proposals by the Department of Energy.
C. Standard testing methods for analysis of cellulose, hemi-cellulose and lignin based on data from NREL should be developed.
D. Methods for the analysis of "bio-crude" or oils produced from biomass conversion processes need to be developed.
E. Methods for the measurement of lactic and poly-lactic acid produced from biomass are needed.
F. A guide is needed for the methods of analysis of simple sugars and saccharification processes products.
G. A study should be done to determine the precision and accuracy of data from laboratories using existing standards. This study will determine if modifications are needed to these standards.
H. Standards are needed for the characterization of the enzymes used in biomass conversion processes.

8. Microbiological Diagnostics

Robert James, Director of Quality Assurance and Regulatory Affairs at Becton-Dickson Microbiology Systems was chair of the workshop on microbiological diagnostics. This workgroup reviewed the following general areas where standards might be considered: (1) reference standards including the need by diagnostic manufactures and users and their development and source, (2) specification standards including the minimum standard for assurance, and achieving the minimum standard, (3) calibration standards for manual and automated delivery systems, (4) stability studies including standardized testing protocols for product stability, standardized testing protocols for establishing storage temperature ranges, and storage and usage temperature standard, (5) standardized training programs on use of microbiological diagnostics. Specific attention was paid to the National Committee for Clinical Laboratory Standards (NCCLS), the FDA guidelines for making premarket submissions, and available international standards such as ISO. In addition, the Center for Disease Control and the National Institutes of Health activities relative to microbial standards were reviewed. The chair and members of the workgroup identified the following specific areas where standards are needed.

A. A guideline for the handling and maintenance of microbial reference strains by the user is needed. The guideline should include the proper receipt, propagation and storage of strains. In addition, an internal quality control program should include biochemical analysis, antigenic properties, toxin production, virulence factors, and susceptibility characteristics (authenticity). The guide should address replacement of strains to include shelf-life recommendations based on storage conditions and low passage suggestions to minimize mutagenic issues.
B. A manufacturer's guideline for stability of diagnostic kits and reagents is needed. The guideline should include a definition of types of studies (e.g., accelerated studies and its relation to real time studies), use of real time versus accelerated studies, statistically valid study design (that includes number of lots, sample size,time frames, normal and adverse conditions, and cyclic temperature studies), shipping tests to include the use of temperature monitoring devices, labeling for shelf-life and shipping conditions, and packaging considerations.
C. A guideline for utilizing thermal cyclers is needed. The guideline should include manufacturing specifications, test methods for manufacturer validation, identification of critical parameters, (e.g., time, temperature, volume), and suggested quality control for the end user. Points to consider for a guideline on thermal cyclers should include allowable tolerances (depending on the design of individual assays), a comparison of thermal blocks, thermal plates and hot air ovens, and a comparison with state of the art equipment.

). Conclusions and Future Directions

The workshop identified many standards and guidelines that would benefit the biotechnology industry. In the area of validation alone, there are over 100 potential standard practices and protocols that need to be developed for biotechnology activities to assist the industry to meet FDA and other agencies regulations. A common need that was expressed in many of the workshops was for a database that would consolidate and cross reference the large number of standards. Another recurrent theme seen in the workshops was the need for better communications between governmental agencies designing standards. This workshop served as a basis for establishing better communication between government, academia, and industry representatives involved in biotechnology standards.

The most effective standards can only be prepared by the best qualified persons on the topic from industry, academia and government. E-48 is seeking these volunteers to assist preparation of new standards in biotechnology to assist in this most important activity. Through close linkage between E-48 activities and the industry needs, we can provide the needed standards for the rapid expansion of activity in the biotechnology field. Interested individuals and company representatives are urged to contact Leigh Anne Sellstedt, ASTM Committee E-48 at 1916 Race Street, Philadelphia, PA 19103-1187 or phone (215) 299-5526.